

Important Notice

This copy may be used only for the purposes of research and private study, and any use of the copy for a purpose other than research or private study may require the authorization of the copyright owner of the work in question. Responsibility regarding questions of copyright that may arise in the use of this copy is assumed by the recipient.

UNIVERSITY OF CALGARY

Microphone and geophone data analysis for noise characterization
and seismic signal enhancement

by

Alejandro David Alcudia León

A THESIS

SUBMITTED TO THE FACULTY OF GRADUATE STUDIES
IN PARTIAL FULFILMENT OF THE REQUIREMENTS FOR THE
DEGREE OF MASTER OF SCIENCE

DEPARTMENT OF GEOSCIENCE

CALGARY, ALBERTA

APRIL, 2009

© Alejandro David Alcudia León 2009

UNIVERSITY OF CALGARY

FACULTY OF GRADUATE STUDIES

The undersigned certify that they have read, and recommend to the Faculty of Graduate Studies for acceptance, a thesis entitled “Microphone and geophone data analysis for noise characterization and seismic signal enhancement” submitted by Alejandro D. Alcudia Leon in partial fulfilment of the requirements for the degree of Master of Science.

Supervisor, Dr. Robert R. Stewart, Department of Geoscience

Dr. Robert J. Ferguson, Department of Geoscience

*Dr. Alejandro Ramirez-Serrano, Department of Mechanical
& Manufacturing Engineering*

Date

ABSTRACT

Source-generated noise, such as air waves and ground roll, is a major challenge in land seismic acquisition. Since much of the surface noise in geophone records arises from a direct impact of air pressure on the geophone case or by conversion of air pressure into ground motion or vice versa, it might be possible to measure air pressure and use it as reference for surface noise attenuation. Microphone data is recorded during land seismic data acquisition to provide air pressure measurements proximal to the geophones. A combination method is developed in the time-frequency domain with the aid of the Gabor transform to suppress the air noise on the geophones. This method is based on the construction of a “mask” function from the microphone Gabor spectrum by setting a threshold on its Gabor coefficients. Then, multiplying the geophone Gabor spectrum with the “mask” function achieves a deterministic cancellation of the associated air-noise component in the geophone. This methodology is applied to two different 3C-2D seismic surveys conducted in Western Canada in 2000 and 2008. In these surveys, the strongest noise measured with microphone prototypes (designed, manufactured and tested by the CREWES Project), is the air blast (or air wave). The results show consistent air wave measurements (both in amplitude and waveform) from trace to trace in the microphone data. The air wave on geophone shot gathers is successfully attenuated by using multiple “mask” functions derived from the microphone data on a trace-by-trace basis. In a separate experiment, a comparison between a single microphone prototype and a calibrated microphone and two professional audio recording microphones, suggests that all microphones under test respond quite similar at frequencies where the source-generated air wave is strongest (>100 Hz). In contrast, all microphones respond very differently to low frequencies, where other noises such as surface waves are dominant (<30 Hz).

ACKNOWLEDGEMENTS

I extend my gratitude to Dr. Robert R. Stewart, my thesis supervisor, for giving me the opportunity to work in this interesting and exciting project. I thank Mr. Henry Bland and Mr. Malcolm Bertram who designed and tested our microphone prototypes. I also extend a special acknowledgement to Dr. Gary Margrave for his Gabor transform codes and other useful signal processing routines included in the CREWES MATLAB Toolbox. Finally, I thank the CREWES Project sponsors and staff for their continuing support.

DEDICATION

To my beloved wife, Mama, Papa, Hugo, Mario, my niece Cassandra and my nephew Emiliano.

TABLE OF CONTENTS

APPROVAL PAGE	ii
ABSTRACT.....	iii
ACKNOWLEDGEMENTS.....	iv
DEDICATION.....	v
TABLE OF CONTENTS.....	vi
LIST OF TABLES.....	ix
LIST OF FIGURES	x
LIST OF ABBREVIATIONS.....	xvii
Chapter One: INTRODUCTION.....	1
1.1. Noise overview.....	1
1.2. Seismo-acoustic sensor in seismic exploration.....	4
1.3. Sound pressure and microphone overview	6
1.4. Seismo-acoustic arrays in other fields of research.....	7
1.5. Thesis objectives	9
1.6. Methodology	9
1.7. Resources	11
Chapter One: SOURCE-GENERATED AIRBORNE NOISE AND ITS INTERACTION WITH THE GROUND	12
2.1. Introduction.....	12
2.2. Source modelling	12
2.2.1. Vibroseis: Circular piston vibrating in an infinite rigid baffle	12
2.2.2. Dynamite.....	17
2.3. Air blast propagation.....	21
2.4. Acoustic-to-seismic transfer function	21
Chapter Two: GROUND VIBRATION AND AIR PRESSURE MONITORING OF SEISMIC SOURCES: IMPLICATIONS FOR SEISMIC WORK AND THE ENVIRONMENT	23
3.1. Introduction.....	23
3.2. Instrumentation and PPV/PAP measurements	25
3.3. Vibration event report	27
3.4. Regulations.....	29
3.5. A case study: Nanton, Alberta	29

3.5.1.	Shock-induced airwave from a buried dynamite explosion.....	30
3.5.2.	Vibroseis	32
Chapter Three: FIELD COMPARISON OF 3-C GEOPHONES AND MICROPHONES TO HIGH-PRECISION BLASTING SENSORS		41
4.1.	Introduction	41
4.2.	Transducer sensitivity	43
4.3.	Instrumentation	44
4.3.1.	3-C geophones	44
4.3.2.	Microphones	45
4.3.3.	Calibrated sensors	47
4.4.	Data acquisition.....	48
4.5.	Vibroseis data.....	53
4.5.1.	3-C geophones	53
4.5.2.	Microphones	59
4.6.	Sledgehammer data	62
4.6.1.	3-C geophones	62
4.6.2.	Microphones	65
4.7.	Particle motion analysis	67
Chapter Four: AIR PRESSURE MEASUREMENTS DURING SEISMIC DATA ACQUISITION.....		70
5.1.	3C - 2D survey at Pikes Peak heavy oilfield, Saskatchewan, Canada	70
5.1.1.	Acquisition.....	71
5.1.2.	Data pre-processing and analysis.....	73
5.2.	3C - 2D high-resolution near-surface survey at the Rothney Astrophysical Observatory, Alberta, Canada.....	82
5.2.1.	Acquisition.....	84
5.2.2.	Data pre-processing and analysis.....	85
5.2.3.	Coherence function	88
5.2.4.	Air-ground transfer function.....	90
Chapter Five: AIR WAVE ATTENUATION IN SEISMIC SIGNALS USING AIR-PRESSURE MEASUREMENTS		96
6.1.	Time-frequency analysis	97
6.2.	Nonstationary filters in the Gabor domain.....	99
6.3.	Method of air wave attenuation in the Gabor domain.....	100

6.4. Field data examples: Pikes Peak and Priddis 3C-2D surveys.....	104
Chapter Six: CONCLUSIONS	113
Chapter Seven: FUTURE WORK.....	115
REFERENCES	116
APPENDIX A: MATCH FILTER DESIGNED VIA WIENER FILTER THEORY	120
APPENDIX B: MATCH FILTER DESIGNED VIA LEAST-SQUARES ADAPTIVE FILTER.....	121
APPENDIX C: THE AIR-GROUND INTERFACE.....	123
C.1. Ground-coupled air wave.....	125
C.2. Air-coupled ground roll.....	127

LIST OF TABLES

Table 2.1. Parameters for the prediction of PPV and PAP from a buried explosion.....	20
Table 3.1. Stand-off distances applied by the CAGC.....	24
Table 4.1. Summary of geophone specifications (Instantel, 2001; Hons, 2008).....	44
Table 4.2. Summary of microphone specifications (from owners' manual)	47
Table 4.3. GEODE channel assignment	51
Table 4.4. Blastmate data from Vibroseis shots.	56
Table 4.5. PPV scaling factors for multicomponent seismic data relative to Blastmate data for Vibroseis shots.....	56
Table 4.6. Blastmate data from hammer shots.....	65
Table 4.7. PPV scaling factors for multicomponent seismic data relative to Blastmate data for hammer shots.....	65
Table 5.1. Pikes Peak survey acquisition parameters	73
Table 5.2. Priddis survey acquisition parameters	85
Table 5.3. Equation 5.3 coefficients obtained by curve fitting.....	94

LIST OF FIGURES

Figure 1.1. Typical scenario for shallow seismic data acquisition (Courtesy of Dr. Don Lawton). The upper panel is a shot record from the seismic reflection experiment shown in the lower panel. In addition to reflections from the target reflector (i.e., coal seam), the geophones also detect and measure refractions, surface waves, and air waves. The goal of seismic processing is to isolate the reflected energy from other unwanted energy across several shot records.	3
Figure 1.2. a) Two-channel (microphone and geophone) motion sensor and (b) single-channel, active noise suppressing geophone (from Stewart, 1998).	6
Figure 2.1. Basic vibrator model (left) (after Sheriff and Geldart, 1995) and circular piston vibrating in an infinite rigid baffle (right) (from Norton and Karczub, 2003).	13
Figure 2.2. Frequency-dependent sound radiation for the circular piston model. At high frequencies, the piston source becomes directional producing lobes or beams of radiated sound (from Norton and Karczub, 2003).	15
Figure 2.3. Sound wave generated with a non-linear sweep (8-150 Hz) at 100m offset. The radius of the piston is 1m and the acceleration of the baseplate (1-28 m/s ²) is varied linearly with time. Note the nodal point at about 570ms and 830ms.	16
Figure 2.4. Sound pressure level estimates for the range 10-1330m from the source. The speed of sound in air used in computations is 332 m/s and the density of air is 1.22 kg/m ³ . The 16s sweep was linear in 8-150 Hz and the acceleration of the baseplate constant (20 m/s ²).	17
Figure 2.5. Geometry used to derive explicit equations for PPV and PAP from a buried dynamite shot (after Gupta et al., 1988).	18
Figure 2.6. Prediction of PPV and PAP with offset distance from a buried explosion. The vertical line at 15 m indicates the boundary of the crater zone.	21
Figure 3.1. Peak particle velocity definition (From Instanetel, 2001).....	26
Figure 3.2. Vibration and air-overpressure monitoring of dynamite shot. The vibration monitor system was located 5 m distance from the explosion. The PPV occurred at 5.001 s in the vertical component. The PSPL also occurred at the same time. The PPV in the horizontal components occurred at slightly later times being smaller than the vertical PPV. Note that the vibrations at such small distance reach threshold levels.....	28
Figure 3.3. Vibration monitor setup (left) and shooter ready to fire a source point (right) (Photos by Dr. Robert Stewart).....	30

Figure 3.4. Vibration and air-overpressure monitoring of dynamite shot at 25 m offset (top). Cross-correlation of vertical ground velocity and air pressure at the surface (bottom).	31
Figure 3.5. PPV and POP monitoring of dynamite shots as a function of distance.	31
Figure 3.6. Vibration and air-overpressure monitoring of Vibroseis source. The vibration monitor system was located 5 m distance from the Vibroseis array. The PPV occurred early in the transverse component, followed by the PPV on the longitudinal, and finally on the vertical. The PSPL was 19 Pa at 0.266 s. Note that none of the components reach a critical vibration level with respect to USBM and OSRME standards.	33
Figure 3.7 Vibration and air-overpressure monitoring of Vibroseis. The vibration monitor was located 50 m distance from the Vibroseis array. PPV for the three components are very small. However, the PSPL was 30.5 Pa at 5.557s. Most interesting is the microphone waveform with dominant low-frequency content.	34
Figure 3.8. Histogram recorded at the Nanton water spring for a series of dynamite shots. The nearest shot to the monitor station was at about 1.6 km.....	36
Figure 3.9. Histogram of natural vibrations recorded at the Nanton water spring nine days before shooting.	37
Figure 3.10. a) Amplitude spectrum, b) Gabor transform in the time-frequency space, and c) time domain representation of the microphone record. Note that there exist high-order harmonics in the signal.	38
Figure 3.11. a) Amplitude spectrum, b) Gabor transform in the time-frequency space, and c) time domain representation of the geophone vertical component. Note there are two high-order frequency harmonics.	39
Figure 3.12. a) Amplitude spectrum, b) Gabor transform in the time-frequency space, and c) time domain representation of the geophone longitudinal component. Note there are two high-order frequency harmonics.	39
Figure 3.13. a) Amplitude spectrum, b) Gabor transform in the time-frequency space, and c) time domain representation of the geophone transverse component. Note there are two high-order frequency harmonics.	40
Figure 4.1. Location map of the test site located west of the University of Calgary Campus. The direction of the seismic line was northeast-southwest (from Google maps).....	42
Figure 4.2. Seven sensors were used in the test: a) OyoGeospace GS-3C geophone, b) Input/Output Spike 3C geophone, c) CREWES microphone prototype, d) APEX 435 condenser microphone, e) EMC8000 electret-condenser microphone, and f) Blastmate III unit with two calibrated sensors (3C geophone and microphone).....	43

Figure 4.3. CREWES microphone prototype and single-pin connector used to transmit the microphone output to the recording system.	45
Figure 4.4. a) Two studio microphones were connected to the analog inputs of a Digidesign MBox2 using conventional microphone XLR cables. b) The MBox2 analog outputs were connected to the Geode receiver cable through special cables consisting of jack connectors on one end and single-pin geophone connectors on the other.	47
Figure 4.5. a) CREWES staff preparing equipment. b) North view of test site. The receiver line was deployed along the vegetation boundary to allow road traffic.	49
Figure 4.6. Southwest view of the seismic line with the mini Vibe located at shot point one (left) and the seven-sensor test pad located at the northeast end (bottom right). The observer's computer was located about 3.5m north of the test station while the Blastmate monitor was located about 1 m east of the test station (top right) (Photos by Alejandro Alcudia).	49
Figure 4.7. Acquisition layout for shot and receiver lines.	50
Figure 4.8. a) Geophone cable connections were facilitated by using color codes for each component. Each Geode recorded a full data set of a particular geophone component. b) The mini EnviroVibe, owned by the University of Calgary, was used as one of two seismic sources.	51
Figure 4.9. Vibroseis data separated by component and sorted into receiver gathers. The top data set is a receiver gather recorded from the ION Spike geophone. The bottom data set is a receiver gather recorded from the OYO geophone at the test station. A 200-ms AGC was applied for display.	54
Figure 4.10. Amplitude spectra average of geophone data. A 2/5-250/255 Hz band-pass filter was applied to these data.	58
Figure 4.11. Amplitude spectra average of microphone data. A 5-260 Hz band-pass filter was applied to uncorrelated data. Note that all microphone responses (including the Blastmate microphone) have a response decrease at about 40 Hz.	59
Figure 4.12. Pressure data recorded from APEX435 (top), CREWES prototype (centre) and EMC 8000 (bottom) microphones for all Vibroseis shots at 2.5m interval. VP's 23 to 32 were spaced every 10 m. Data were cross-correlated with the pilot sweep. AGC of 250 ms was applied to data for display only. The average of amplitude spectra is also show at the bottom. Note that all microphone responses are quite similar at high-frequencies, where the air blast is dominant.	61
Figure 4.13. Hammer data separated by component and sorted in receiver gathers. The top data set is a receiver gather recorded from the ION Spike geophone. The bottom data set is a receiver gather recorded from the OYO geophone at the test station. A 200-ms AGC was applied for display.	63

Figure 4.14. Average amplitude spectra for each component of ground velocity for hammer shots.	64
Figure 4.15. Average amplitude spectra of microphone data. 11 hammer shots were used for these computations. A band-pass filter (0-2-250-255 Hz) was initially applied to the data (top left and top right). Note that the frequency response of the EMC 8000 microphone (in red) is very close to the Blastmate calibrated microphone (in black) for the entire frequency band. By applying a second band-pass filter to attenuate frequencies less than 15 Hz, the average spectra of the CREWES prototype (dashed blue) and the APEX 435 microphone (green) were partially corrected (bottom left and bottom right).....	66
Figure 4.16. Geometry of source-receiver position for polarization analysis.	67
Figure 4.17. Analysis of particle motion computed from the first breaks (one half-cycle) of particle velocity data (hammer). H1 is the radial (inline) component and H2 is the transverse (cross-line) component. Vertical components are mapped into the vertical axis. From left to right, hodograms correspond to shot points at 0, 2.5, 5.0 and 7.5 m nominal offsets.....	68
Figure 5.1. Location map of the Pikes Peak heavy oilfield, Saskatchewan.	71
Figure 5.2. Acquisition layout for the Pikes Peak multicomponent survey (from Hoffe et al., 2000).	72
Figure 5.3. Time-frequency decomposition of the Vibroseis sweep used in the Pikes Peak survey. The 16s sweep was linear from 8-25 Hz and nonlinear from 25-150 Hz.....	75
Figure 5.4. Uncorrelated microphone output recorded at nominal zero offset from the Vibroseis array and represented in the time-frequency domain.	75
Figure 5.5. Analysis of air-pressure amplitude as a function of distance for several microphones. Note how the high-frequency components of the air wave decay with distance while the low-frequency components remain strong. Also note that the lobes of radiated sound disappear with distance.....	76
Figure 5.6 Vibroseis-uncorrelated microphone output recorded at 40 m nominal offset from the Vibroseis array. The first nodal point (or lobe) occurred at about 5 s when the sweep frequency was about 110 Hz. The second nodal point occurred at about 9 s when the sweep frequency was close to 130 Hz.	77
Figure 5.7 Example of correlated microphone (left) and geophone data (right) from Pikes Peak. Note that the airwave in these shot records propagates at the speed of sound in the air (331 m/s).	79

Figure 5.8. First 1000 ms of uncorrelated microphone data. Raw data and time analysis window (not gained) are shown of the left. Windowed data with AGC is shown of the right.....	80
Figure 5.9 Amplitude spectrum of the first 1000 ms of uncorrelated microphone data over the analysis window shown in Figure 5.6 with no amplitude scaling. This wave train in the uncorrelated microphone data corresponds to the low-frequency component of the Vibroseis-generated sound wave with peak amplitude between 20-23 Hz.	81
Figure 5.10 Vibroseis correlated vertical geophone (left) and microphone data (right). A 10/12/25/30 Hz band-pass filter was applied to these data to investigate the low-frequency energy in the typical ground-roll frequency band. A 500-ms AGC has been applied.	81
Figure 5.11. F-k spectra of vertical component of ground velocity (right) and air pressure (left). A 10/12/25/30 Hz band-pass filter was applied to both shot gathers to investigate the low-frequency energy contained in these records. Note that the microphone information in the surface wave's bandwidth is the low-frequency component of the air wave.....	82
Figure 5.12. Location map of the test site at Priddis, Alberta.	83
Figure 5.13. CREWES students and staff provided a valuable help in the field. Each microphone was placed besides a geophone every 5 m (photos by Gabriela Suarez and Alejandro Alcudia).....	83
Figure 5.14. Acquisition layout at Priddis survey.	84
Figure 5.15. Time-frequency decomposition of the Vibroseis sweep used in the high-resolution near-surface survey at Priddis. The 10s sweep was linear from 10-250 Hz.....	86
Figure 5.16. Uncorrelated microphone output recorded a few metres from the EnviroVibe and represented in the time-frequency domain. The sweep was linear from 10-250 Hz.....	86
Figure 5.17. Common shot gather of microphone (left) and vertical component seismic data (right) with the Vibroseis source at 100m offset from station 101.	87
Figure 5.18. Common shot gather of microphone (left) and vertical component seismic data (right) with the Vibroseis source in split-spread shooting.	88
Figure 5.19. Coherence functions computed for two pairs of geophone and microphone signals.	90
Figure 5.20. Vertical component of the geophone for a shot point located at station 301 (far right). Trace spacing is 1m. A 200-ms AGC was applied to the raw data.....	91

Figure 5.21. Vertical component of the geophone for a shot point located at station 301 (far right). Trace spacing is 1m. A 120-250 Hz band-pass filter has been applied to the data.....	92
Figure 5.22. Same as Figure 5.20 with a 200-ms AGC for display purposes.....	93
Figure 5.23. LMO-corrected geophone data for regression analysis.....	94
Figure 5.24. Results of geophone data fit to the exponential amplitude decay models.....	95
Figure 6.1. Fourier and Gabor transforms of an uncorrelated Vibroseis signal (i.e., the air wave) recorded with a microphone. The upper left is the signal of interest represented in the time domain. Signal representations are achieved using the Fourier transform for the frequency domain representation (upper right) and the Gabor transform for the joint time-frequency domain representation (lower left)...	98
Figure 6.2. a) Geophone signal and b) microphone signal in the time domain. c) Geophone signal and d) microphone signal in the time-frequency domain (Gabor domain).	101
Figure 6.4. A single-trace example from the Priddis survey. a) Original trace, b) filtered trace, and c) difference between original and filtered trace.....	105
Figure 6.5. A single-trace example from the Pikes Peak survey. a) Original trace, b) filtered trace, and c) difference between original and filtered trace.	105
Figure 6.6. Shot gather from the Pikes Peak data set. A 50 ms window and 1 ms time-shift was used for this shot gather. Note that the air wave has been attenuated while preserving the frequency content of other seismic events.	107
Figure 6.8. Common shot gather from the high-resolution near-surface survey before and after applying our Gabor combination method. A 25 ms Gaussian window shifted at 1ms time increment was used for the Gabor transformations. The threshold for constructing the “mask” filter was set to $maxGC/8$	109
Figure 6.9. Same example as in Figure 6.8 showing the original shot record (left), its filtered version (centre) and the difference between raw and filtered data (right). Displays have been changed to variable density and amplitudes scaled relative to the peak amplitude on each shot record.	109
Figure 6.10. f-k spectra of shot gathers shown in Figure 6.8. Note that the air wave is spatially aliased in the original data and wraps around at about 100 Hz (left). The Gabor combination method attenuated the aliased air wave to a great extent. However, some residual air wave remains in the data.....	110
Figure 6.11. Another shot gather from the Priddis high-resolution survey with the same filter parameters as in the example for SHOT 1. The original data is shown on the left, its filtered version is shown in centre panel, and the difference between	

original and filtered data is shown on the right. The amplitudes have been scaled relative to the peak amplitude on each shot record.....	110
Figure 6.12. Same example as in Figure 6.11 showing the original shot record (left), its filtered version(centre) and the difference between raw and filtered data (right). Displays have been changed to variable density.	111
Figure 6.13. f-k spectra of shot gathers shown in Figure 6.11. Note that the air wave is spatially aliased in the original data and wraps around at about 100 Hz (left). The Gabor combination method attenuated the aliased air wave to a great extent. However, some residual air wave remains in the data.....	111
Figure 6.14. An example of air wave attenuation in a split-spread shot gather from Priddis. Data have been scaled relative to peak amplitude in the entire shot gather. Data before filter (left), data after filter (centre) and difference between original and filtered data (right).....	112
Figure A.1. A Wiener filter produces good noise estimates in the geophone signal by matching the input microphone signal (top).....	120
Figure B.1. A two-pass adaptive filter for air wave attenuation. The reference input to the filter, $x(n)$, is a microphone signal. Note that noise estimations, $y(n)$, are good but noise attenuation is achieved only after the second pass. However, this procedure is not as robust as the Gabor method.	121
Figure B.2 Example of power-line noise cancellation by using the microphone signal as noise reference in an adaptive filter.....	122
Figure C.1. Propagation mechanism of the acoustic-induced waves in the ground (after Mooney and Kaasa, 1962).	124
Figure C.2. P-wave transmission coefficients at the air-ground interface for a) an incident P-wave and b) an incident S-wave from the ground. Solid lines represent the magnitude and dashed lines represent the phase of the transmission coefficients. For the P-wave case, the phase is zero for all incidence angles. For the S-wave, there is a change in phase from zero for angles beyond the critical. ..	127
Figure C.3. Simple model of the resonant coupling that occurs when the S-wave associated with the ground roll is equal to the speed of sound in the air. The upper curve corresponds to the particle displacement in the vertical component. The lower curve corresponds to particle displacement in the horizontal component.....	128

LIST OF ABBREVIATIONS

AEC	-	Automatic envelope correction
AGC	-	Automatic gain correction
CAGC	-	Canadian Association of Geophysical Contractors
f-k	-	Frequency-wavenumber
IAGC	-	International Association of Geophysical Contractors
LMO	-	Linear moveout
MaxGC	-	Maximum Gabor coefficient in the microphone Gabor spectrum
OBC	-	Ocean Bottom Cable
OSMRE	-	Office of Surface Mining Reclamation and Enforcement
PAP	-	Peak air pressure
POP	-	Peak overpressure
PPV	-	Peak particle velocity
RMS	-	Root Mean Square
SPL	-	Sound pressure level
UBSM	-	United States Bureau of Mines

CHAPTER ONE: INTRODUCTION

1.1. Noise overview

The success of the seismic method in providing a high-resolution image of the earth's subsurface largely depends upon the quality of the seismic data (Pritchett, 1990). Survey design, instrumentation, terrain complexity and human activity in the survey area play major roles in achieving good data quality (Pritchett, 1990). However, a crucial step in creating high-resolution images is that related to mitigating seismic and ambient noise while preserving signal (Pritchett, 1990). Sheriff and Geldart (1995) use the term *signal* to refer to any event on the seismic record from which one wishes to obtain information, everything else is *noise*. Russell et al. (1990) define noise as “*anything on the seismic data that does not fit our conceptual model of the data, that is, as clean seismic reflections*”.

According to Sheriff and Geldart (1995), seismic noise may be separated into two major categories based on its coherency across several traces. *Incoherent noise*, also known as *random noise*, is different from trace to trace and cannot be followed within a few traces in a seismic record. Random noise is usually generated from winds, instruments, wildlife, and human activity in the survey area. On the other hand, *coherent noise* can be tracked as a consistent event in a seismic record (Sheriff and Geldart, 1995). Some examples of coherent noise are surface waves, refracted waves, air waves and multiples.

Exploration geophysicists have encountered source-generated noise problems for almost any seismic source used at the surface: most sources not only generate vibrations in the form of body waves but also excite surface waves and produce strong air waves (Pritchett, 1990; Kalinski, 2007). Because surface waves and air waves can be tracked and

followed for more than a few traces, source-generated noise can be classified as coherent noise (Sheriff and Geldart, 1995).

Figure 1.1 depicts a typical scenario for shallow seismic data acquisition with a single seismic source at the surface. The lower panel of this figure shows the variety of raypaths for the different wave modes propagating from the source to the receiver. An example of a shot record is shown in the upper panel of Figure 1.1. Note that unwanted surface waves and air waves are dominant over a large portion of the entire shot record.

While there are many ways to filter out source-generated noise, it still can be a problem. For example, the air waves in shallow surveys may occupy a comparatively large window on the scale of a shot record as in Figure 1.1. These air waves can obscure primary reflections at the near offsets and may lie in the same frequency band of reflected energy. For this reason, a simple band-pass filter does little to attenuate the air noise while preserving the signal. Similarly, conventional f-k filtering cannot be applied easily and must be used cautiously due to spatial aliasing of the air waves (Steeple and Miller, 1998). Spatial aliasing means insufficient sampling along the space axis (Claerbout, 1985). To avoid spatial aliasing, Claerbout (1985) suggests that surface seismic data should be sampled at more than two points per wavelength (λ). Since wavelength is inversely proportional to frequency (f), higher frequency components have shorter wavelengths and are more likely to be spatially aliased (Pritchett, 1990).

The air waves are broadband and usually exhibit frequencies above 200 Hz (Steeple and Miller, 1998). If $f > 200$ Hz, then $\lambda < 1.715$ m for a speed of sound in the air of 343 m/s. Therefore, these acoustic waves are likely to be spatially aliased unless the geophone

interval is substantially less than 1 m (Steeple and Miller, 1998). Of course, there is a practical trade-off between the expense of a survey (which increases with decreasing geophone interval) and our desire to avoid spatial aliasing (Lines and Newrick, 2004).

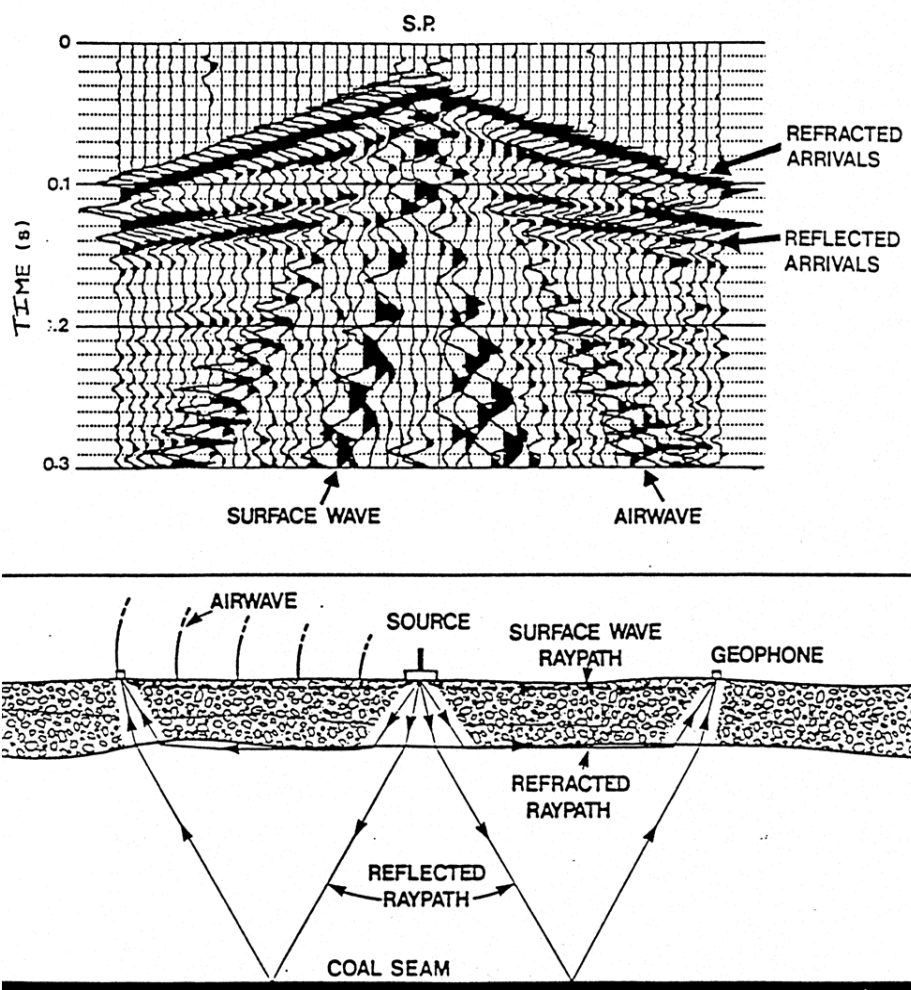


Figure 1.1. Typical scenario for shallow seismic data acquisition (Courtesy of Dr. Don Lawton). The upper panel is a shot record from the seismic reflection experiment shown in the lower panel. In addition to reflections from the target reflector (i.e., coal seam), the geophones also detect and measure refractions, surface waves, and air waves. The goal of seismic processing is to isolate the reflected energy from other unwanted energy across several shot records.

1.2. Seismo-acoustic sensor in seismic exploration

Seismic exploration geophones are designed to measure the particle velocity component of ground motion. Unfortunately, the seismic energy arriving at the surface of the ground, detected by several geophones, is a complex collection of wave modes sharing the same frequency band. Separating and extracting desired reflected energy from other wave modes and surface noise (i.e., air waves, surfaces waves and ambient noise) is not always an easy task in seismic processing.

Most of the existing algorithms for coherent noise attenuation are based on the transformation of the data into a different domain that exploits the characteristic that most distinguishes noise from signal (Larner et al., 1983). Some distinguishing characteristics in seismic data analysis are frequency, dip, apparent velocity and wavenumber (Larner et al., 1983). Some practical examples include coherent noise attenuation in the frequency - wavenumber (f-k) domain, radial trace (RT) domain (Henley, 2003) and Radon domain (Russell et al., 1990).

A different approach for noise attenuation utilises noise models as reference in adaptive subtraction schemes. These noise models are usually constructed from the actual seismic data or by modeling. The most common application of adaptive subtraction is found in surface-related multiple elimination (e.g., Verschuur et al., 1992).

In another application, Karsli and Bayrak (2008) introduce a method that uses Wiener filters to estimate ground-roll from a reference noise signal and then subtract the ground-roll from the seismic data. Such a reference noise signal is generated from a simple sweep signal whose frequency content varies similarly to that of ground-roll.

As it was previously mentioned, most of the reference signals used for noise estimation and attenuation are extracted from the actual seismic data or generated by modeling, but what about having an independent noise reference from a different sensor in the field to provide a measure of the surface noise? Since much surface noise within geophone records arises from a direct impact of air pressure on the geophone case or by conversion of air pressure into ground motion or vice versa, it might be possible to measure air pressure and use it as reference for surface noise attenuation.

Stewart (1998) proposes a noise-reducing multi-sensor for seismic land operations. It basically consists of a dual-sensor (two-element) instrument having a microphone within the geophone case or in the proximity to the geophone to give air pressure measurements. If sufficient correlation between seismic and air pressure records exists, then a combination of these data may be used to attenuate and reduce air-related noise in the geophone.

This approach is similar to four-component (4-C) ocean-bottom-cable (OBC) seismic recording in the marine environment, where a single hydrophone and a 3-C geophone are combined (summation of hydrophone + vertical geophone signal) for the suppression of receiver-side multiples (Hoffe et al., 2000).

Figure 1.2 shows two design possibilities according to Stewart (1998): a) we can record air pressure and ground velocity within the geophone case on two separate channels and do processing, or b) we can make a single-channel active-noise suppressing geophone. The latter approach is based on the well-known concept of the active noise reducing headphone technology (). From this point of view, the geophone output is cross-correlated against a

reference microphone in real-time. Then, the air-correlated noise values from the geophone are filtered before transmission to the recording system.

To evaluate Stewart's proposal, the Consortium for Research in Elastic Wave Exploration Seismology (CREWES) at the University of Calgary undertook a couple of experiments with a modified version of case a). The analysis of simultaneous air pressure and ground velocity recordings during these experiments, and the evaluation of a method to combine these data for air-noise attenuation constitute the framework of this thesis.

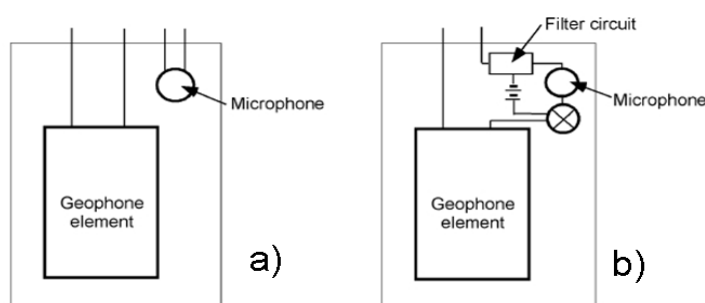


Figure 1.2. a) Two-channel (microphone and geophone) motion sensor and (b) single-channel, active noise suppressing geophone (from Stewart, 1998).

1.3. Sound pressure and microphone overview

Sound is generated by any vibrating structure or mechanism (Carley, 2004). Sound pressure is described most commonly in Pascal units (Pa) and Sound Pressure Level (SPL) in decibels. The SPL is an expression of a given sound pressure in Pa referenced to 20 uPa, which is considered to be the quietest sound some humans may hear (Carley, 2004). A positive pressure pulse corresponds to the compression phase of a sound wave and a negative pulse corresponds to a rarefaction. These two phases of a sound wave are deviations from the local atmospheric pressure (1 atm = 100 kPa), that is, the effective sound pressure is the root mean square (RMS) difference between the peak pressure and the local atmospheric pressure. A sound pressure wave can be a composite of many

frequencies, of course, but a distinction must be introduced when the dominant frequencies are within the humans' audible band or outside. A human being can hear pressure variations (or sounds) in the frequency range from 20 Hz up to 20 kHz. Any given sound with dominant frequencies below the threshold of human hearing is called infrasound. These low-frequency pressure variations are particularly important in earthquake seismology and volcano studies for air vibration monitoring. In exploration seismology, we are concerned about sound propagation in the frequency band of the seismic source and its associated reflections. The bandwidth depends on the source type and the target depth. Both sound and infrasound are often generated.

A microphone is a transducer that converts sound pressure into an electrical signal. The basic microphone design consists of a thin membrane which vibrates in response to an incident sound pressure (Norton and Karczub, 2003). The vibration of the membrane in a microphone is the analog to the velocity of the coil with respect to the case in a geophone. In both cases, the output voltage is proportional to the motion of the sensing element from rest position relative to a reference point.

1.4. Seismo-acoustic arrays in other fields of research

Past experiments in global seismology (e.g., Hill et al., 1976; Kappus and Vernon, 1991; Beauquin et al., 1996; Sharp and Yule, 1998; Le Pichon et al., 2001; Edwards et al., 2007; Lin and Langston, 2007) and acoustics (e.g., Albert and Orcutt, 1990; Albert, 1993; Harrop and Attenborough, 1998; Xiang and Sabatier, 2000) have shown and proved the advantage of using collocated microphones (or microbarometers) and 3-C geophones for sensing related air pressure and particle velocity at the earth's surface, where the interaction of an acoustic wave with the ground produces well-defined wave propagation effects. This

type of instrumentation has been used extensively in global seismology, for example, to study the effects of atmospheric pressure changes on seismic station records. Beauduin et al. (1996) used barometers to record atmospheric pressure variations and then improve the quality of recorded long-period seismic signals by combining pressure and seismic data.

More recently, Lin and Langston (2007) have studied the thunder-induced ground motions using a seismo-acoustic array consisting of low-frequency geophones and infrasound microphones. Edwards et al. (2007) analyse the excitation and propagation of hypersonic shockwaves in the ground from an artificial “meteor” (i.e., the re-entry of NASA’s Stardust sample return capsule) and give results of the acoustic-to-seismic coupling using a collocated infrasound-seismic array.

Acoustics research uses the vertical seismic transfer function (m/s/Pa), also called the acoustic-to-seismic transfer function, to detect land mines or other buried objects (Xiang and Sabatier, 2000). Others have used such a transfer function to study the outdoor sound propagation and its interaction with the ground as it travels horizontally (Albert, 1993).

Another major application is found in blast explosion monitoring, where both the air and ground vibration levels are measured using a high-precision microphone and a triaxial geophone connected to a portable recorder. It is noteworthy that previously mentioned applications in acoustics, earthquake and global seismology could be adapted to exploration seismology to better understand the air-noise coupling into the ground and consequently into the geophones.

1.5. Thesis objectives

In this thesis, the dual-sensor concept proposed by Stewart (1998) for noise attenuation in seismic land operations is studied. A number of microphone prototypes were built by the CREWES Project in 2000 and deployed in the field during two different 3C-2D seismic surveys in western Canada. Air pressure and multicomponent seismic measurements were recorded on separate channels for further processing. A detailed analysis of such unique data sets and a new air-noise filtering technique are presented. The proposed filtering technique for air noise attenuation in geophone records combines pressure and particle velocity in the time-frequency domain, with the aid of the Gabor transform implementation of Margrave et al. (2005). Other methods designed in the time domain are suggested and included in Appendices A and B. As complementary work, the microphone prototypes are compared to a couple of studio microphones and a calibrated blasting microphone. A similar comparison is undertaken with 3-C geophones used for seismic acquisition and a calibrated 3-C geophone used for blasting monitoring.

1.6. Methodology

This thesis starts with an overview of source-generated noise focusing on airborne noise, its propagation, attenuation and interaction with the ground (Chapter 2). Modelling of the airborne-noise sources is essential to draw a broad picture of the physics involved and obtain estimates of expected amplitudes. The concept of acoustic-to-seismic transfer function (air-coupling) is also introduced. This transfer function can be used to quantitatively describe the transfer of vibrational energy from the air to the ground in the form of seismic waves.

Monitoring data of ground vibrations and air pressure generated by seismic sources during a seismic survey are presented in Chapter 3. Several dynamite and Vibroseis shot points were monitored as a function of distance at Nanton, Alberta by an engineering contractor and reported to Compton Petroleum Corporation. Some data from this acquisition is used here to show the amplitude decay of ground and air vibrations with distance. The most accepted regulations of peak particle velocity (PPV) and peak air pressure (PAP) permissible levels in Canada and overseas are also presented.

Instrument calibration is a very important step for any kind of data acquisition program. Ultimately, accurate measurements depend upon instruments fidelity and field response. In Chapter 4, a 3-C geophone (typically used for seismic exploration) is compared to a high-precision calibrated 3-C geophone (mostly employed for blast monitoring). The CREWES microphone prototypes and two additional large-diaphragm microphones are also compared to a calibrated microphone.

This thesis continues with the introduction and analysis of two data sets recorded during two different seismic surveys (Chapter 5). Surface air pressure measurements were recorded from several microphones collocated with 3-C geophones along the seismic acquisition profiles, allowing for direct measurement of air pressure and seismic particle velocity at the same position over the air-ground interface.

Finally, a novel technique for seismic signal enhancement is presented, which assists in air blast attenuation. The proposed filter exploits the benefits of time-frequency decomposition of a signal by means of the Gabor Transform. The theory of time-frequency analysis with a particular emphasis on the Gabor transform and how to design

nonstationary filters in this domain is reviewed. The latter constitutes the main contribution of this thesis.

1.7. Resources

Several resources were available within the CREWES project and the Department of Geoscience at the University of Calgary. Most data used in this thesis were acquired and provided by the CREWES Project. The first microphone data set was acquired at the Pikes Peak heavy oilfield by Veritas DGC (now CGGVeritas) on behalf of the CREWES Project. The second microphone data set recorded at the Rothney Astrophysical Observatory was fully acquired by CREWES staff and students. Calibration data recorded near the University of Calgary campus were also acquired by CREWES staff. Ground vibration and air overpressure data were acquired by WorleyParsons Komex and provided by Compton Petroleum Corporation. Most of the data analysis was undertaken in MATLAB™ 7.1., a product of MathWorks™. The CREWES MATLAB toolbox was extremely useful for our purposes and objectives in this thesis. For instance, the Gabor transform code was written by Dr. Gary Margrave and it is available within the CREWES toolbox. Air pressure and seismic data were previewed and pre-processed with VISTA™ 7.0., a product of and generously donated by GEDCO™. Seismic source monitoring data were analyzed with Blastware™ 8.0, a product of Instantel™. This thesis was written and assembled in Microsoft Office Word™.

CHAPTER ONE: SOURCE-GENERATED AIRBORNE NOISE AND ITS INTERACTION WITH THE GROUND

2.1. Introduction

Noise produced during seismic data acquisition is a direct consequence of imperfect seismic sources. For deep-target exploration surveys (i.e., hydrocarbon exploration), Vibroseis trucks and dynamite charges are the most common and preferred sources of seismic energy. For engineering and environmental surveys, a sledgehammer blow on a metal plate generates enough energy to acquire shallow reflection and refraction data. A common problem with most seismic sources is that related to the generation of strong sound waves in the air, often referred to as air blast or air wave. In this chapter, a model for the Vibroseis-generated air wave, which is based on previous work by Sallas and Brook (1989), is presented. PPV and PAP predictions from buried dynamite explosions are also presented. These predictions are computed from explicit equations derived by Gupta et al., (1988).

2.2. Source modelling

2.2.1. Vibroseis: Circular piston vibrating in an infinite rigid baffle

The airborne noise generated by a Vibroseis truck can be regarded as a problem of sound fields around solid bodies. This phenomenon can be studied using the theory of vibrating bodies (Carley, 2004). Previous experimental studies of the air wave produced by the vibrator (Brook et al., 1989; Sallas and Brook, 1989) suggest that the surface of the vibrator's baseplate acts like a loudspeaker array and is the primary generator of the air wave. According to Sallas and Brook (1989), the air wave source can be modelled as a circular piston source vibrating in an infinite rigid baffle (i.e., the basic model of a

loudspeaker). Figure 2.1 shows a diagram of the basic vibrator model (left panel) and illustrates the circular piston vibrating in an infinite rigid baffle (right panel). The circular piston model ignores the contribution of the vibrator's reaction mass to the air wave propagating horizontally. The reaction mass oscillates up and down causing compression of the air above its upper face and rarefaction of the air below its lower face. Sallas and Brook (1989) state that the reaction mass on a P-wave vibrator behaves like a dipole source with its two elements in antiphase, and therefore it can be considered a less efficient radiator of horizontal acoustic noise than the baseplate. The model of the air wave source also ignores any sound produced by the Vibroseis truck exhaust system.

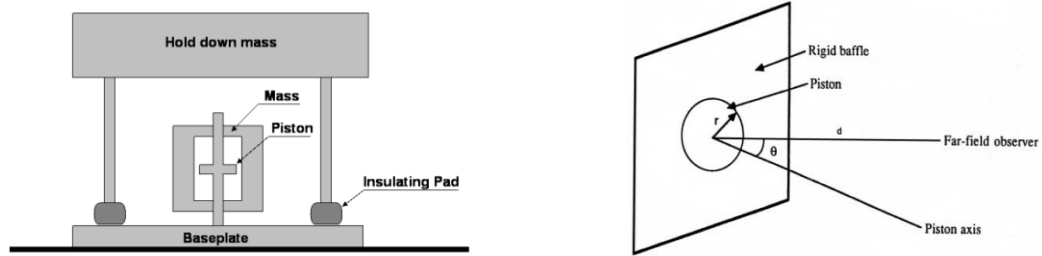


Figure 2.1. Basic vibrator model (left) (after Sheriff and Geldart, 1995) and circular piston vibrating in an infinite rigid baffle (right) (from Norton and Karczub, 2003).

The model of sound pressure radiation from the Vibroseis system is given by

$$p(\omega, t, r) = \frac{\rho_0 \cdot a \cdot r^2}{d} \frac{J_1\{x\}}{x} e^{\left(-i\omega\left(t - \frac{d}{c}\right)\right)}, \quad (2.1)$$

where p is the sound pressure generated by the piston of radius r (m), oscillating at frequency ω (r/s or revolutions/second) at an acceleration of a (m/s^2), measured at an angle θ from the piston axis and a distance d (m) from the source. The speed of sound in air is c (m/s), ρ_0 is density of air, J_1 is a Bessel function of the first kind of order 1, $x = kr \sin(\theta)$, and k is the angular wavenumber (Sallas and Brook, 1989).

From Equation (2.1), the directivity of sound pressure is given by the term

$$D(\theta) = \frac{2J_1\{x\}}{x} = \frac{2J_1\{kr\sin(\theta)\}}{kr\sin(\theta)}, \quad (2.2)$$

while the phase information is given by the complex exponential

$$e^{\left(-iw\left(t-\frac{d}{c}\right)\right)}. \quad (2.3)$$

According to Carley (2004), “when a body is large compared to the wavelength of the sound it generates, interference between sounds from different parts of the body give rise to a complicated sound pattern, especially in the region near the body. When the body is small on a wavelength scale (or vibrates at low frequencies), the phase difference between different parts of the source is not enough to give rise to much interference and the body radiates like a point source. The ‘size’ of a body at a given frequency is called its compactness and is characterized by the parameter kr where r is the characteristic dimension”. In other words, the compactness kr drives the sound radiation pattern from the piston and is frequency dependent through the wavenumber ($k=w/c$).

Figure 2.2 depicts the behaviour of the piston for different magnitudes of compactness (note that kr is equal to kz in the figure). At low frequencies ($kr \ll 1$), the piston radiates like a point source and the sound intensity distribution is approximately constant, whereas at high frequencies there are several nodal points and corresponding lobes of radiated sound (Norton and Karczub, 2003). The physical consequence of the sound radiation at high frequencies is that the source becomes directional (Norton and Karczub, 2003).

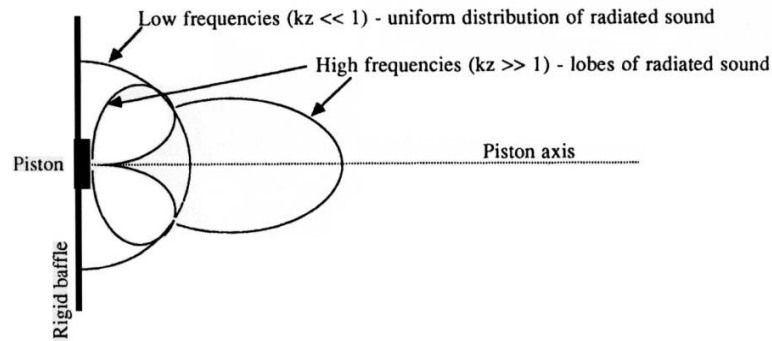


Figure 2.2. Frequency-dependent sound radiation for the circular piston model. At high frequencies, the piston source becomes directional producing lobes or beams of radiated sound (from Norton and Karczub, 2003).

In order for the radiation to be highly directional, the source must be large compared to the wavelength (Norton and Karczub, 2003). For a 10-250 Hz Vibroseis sweep, wavelengths oscillate between 33.3m at 10 Hz and 1.33m at 250 Hz for a sound wave propagating at 333 m/s. This suggests that the sound radiated by the Vibroseis system may become directional as the frequency gets higher. If the radius of the circular piston r for a single Vibroseis truck is set to 1 m (i.e, the radius of the baseplate) and the frequency is 100 Hz, the parameter kr is 1.88 ($kr > 1$). However, at 250 Hz, the parameter kr is 4.71 ($kr \gg 1$) and the sound field radiated by the Vibroseis may become directional. This directionality produces lobes or beams of radiated sound as explained above. Figure 2.3 shows a simulation of a nonlinear sweep (8-150 Hz) recorded at 100 m from the source. The maximum and minimum pressure are +0.08 and -0.08 Pa. The effect of the parameter kr can be observed in the simulated sound wave with some nodal points at about 570ms and 830 ms (i.e., the sweep frequencies increase with increasing time). In Chapter 5, some uncorrelated microphone traces recorded near the Vibroseis source suggests the existence of sound beams as a function of time.

The model was also used to compute estimates of sound pressure levels at various distances from the source. Figure 2.4 shows sound pressure level estimates corresponding to distances in the range 10-1330m from the source. Note that the sound pressure level decays as the inverse of distance in agreement with observations by Brook et al., (1989).

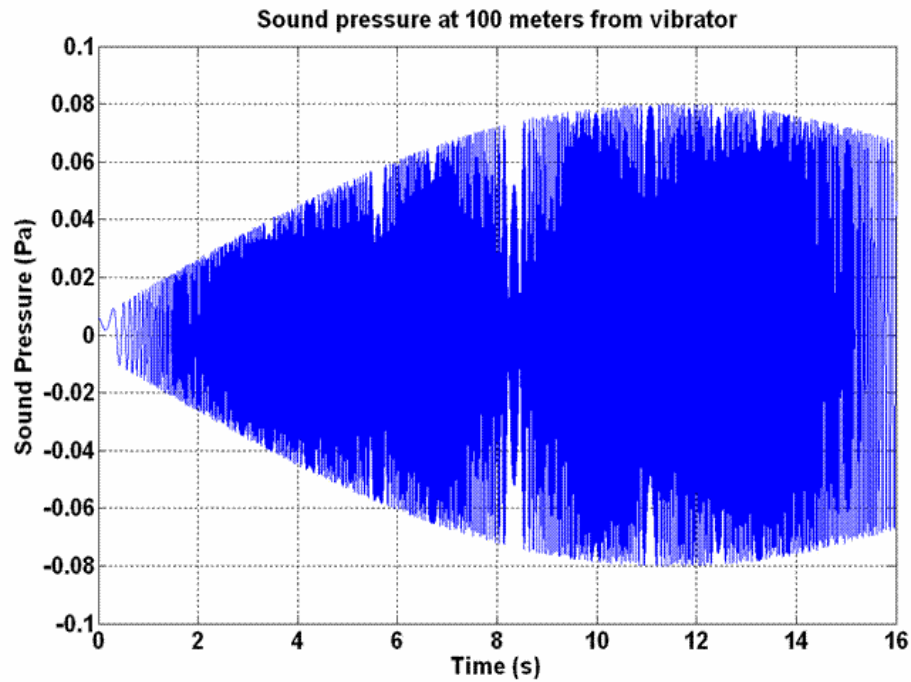


Figure 2.3. Sound wave generated with a non-linear sweep (8-150 Hz) at 100m offset. The radius of the piston is 1m and the acceleration of the baseplate ($1-28 \text{ m/s}^2$) is varied linearly with time. Note the nodal point at about 570ms and 830ms.

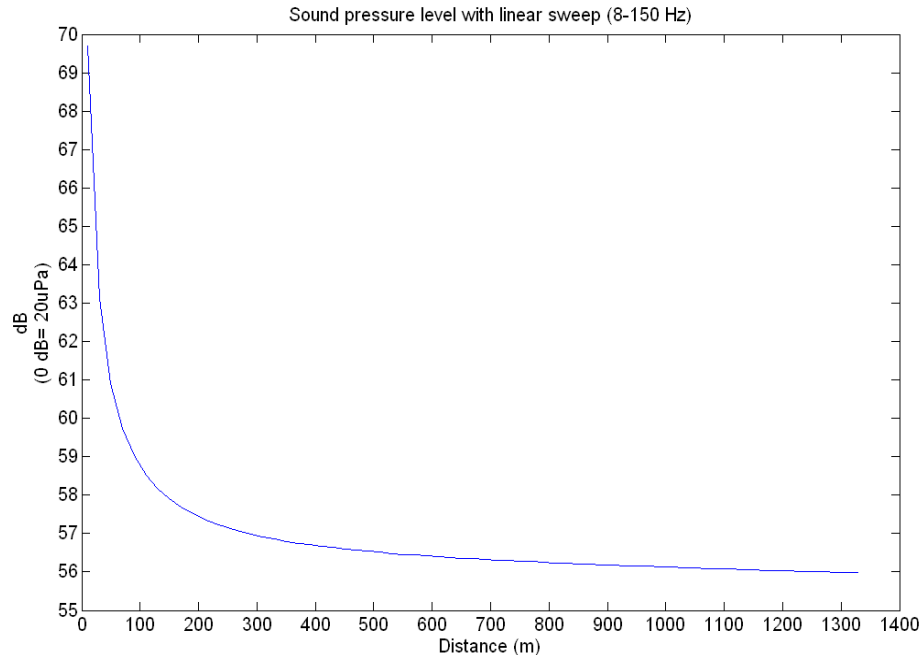


Figure 2.4. Sound pressure level estimates for the range 10-1330m from the source. The speed of sound in air used in computations is 332 m/s and the density of air is 1.22 kg/m³. The 16s sweep was linear in 8-150 Hz and the acceleration of the baseplate constant (20 m/s²).

2.2.2. Dynamite

Gupta et al. (1988), in a study of ground and air vibration predictions generated by buried explosions, suggests that approximately 20 to 30% of the dynamite energy is utilised in fragmenting the rock or other host materials. Part of the energy is not only transmitted through the earth in the form of seismic waves (i.e., used for seismic exploration) or vibrations, but also dissipated in the air, producing noise. Gupta et al. (1988) explain that the vertical vibration of the earth's surface produces an equivalent particle velocity in the air, which results in air vibration of the same frequency as the seismic waves. In other words, the ground surface acts as a piston moving the air above the point of detonation, producing a distinct air blast pulse. This is often referred to as ground-shock-induced air blast. However, the air vibrations produced by ground motion resulting from dynamite blast are small compared to air vibrations generated by mud, rocks and venting gases in a shot

hole (Pritchett, 1990). According to Pritchett (1990), noise from mud and rocks ejected from the shot holes should also be classified as source-generated noise because increasing the charge will likely also increase the noise.

Gupta et al. (1988) derive explicit equations for the prediction of PPV and PAP generated from a buried explosion (see Figure 2.5 for geometry of the problem). These equations incorporate physical parameters including (i) P-wave velocity, (ii) S-wave velocity, (iii) density of the rock, (iv) characteristic impedance of the air, (v) detonation pressure of explosive, (vi) depth of hole, (vii) radius of hole, and (viii) distance of the measuring geophone.

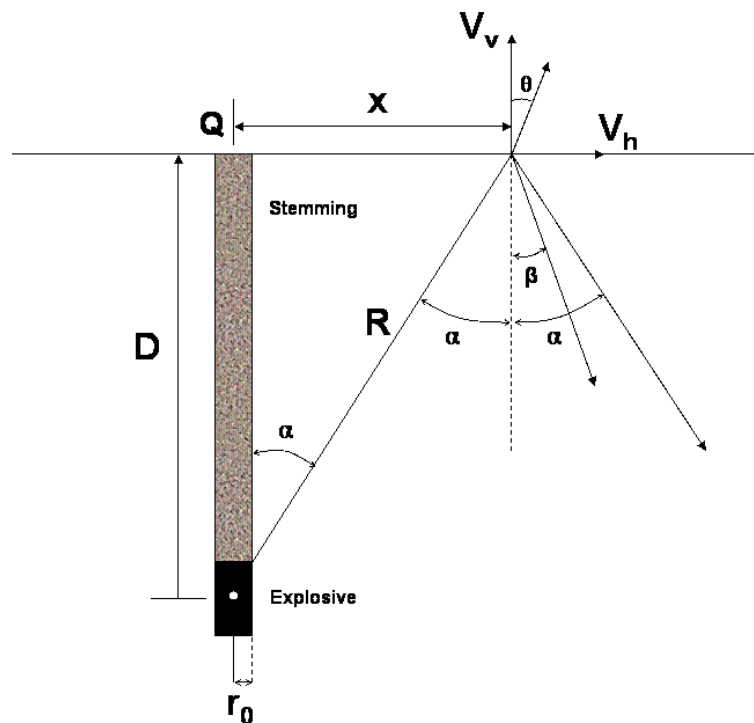


Figure 2.5. Geometry used to derive explicit equations for PPV and PAP from a buried dynamite shot (after Gupta et al., 1988).

The prediction equations of Gupta et al. (1988) are derived for direct values of PPV and PAP at any point outside the crater zone ($x > D$), within the crater zone ($x < D$), and at the boundary of the crater zone ($x = D$). From Figure 2.5, the crater zone is defined by the horizontal distance x and vertical distance D from ground zero Q . In this chapter, the equations of Gupta et al. (1988) are used to estimate direct values of PPV and PAP at any point outside the crater zone. A valid reason for computing PPV and PAP outside the crater zone only is that most measurements are usually undertaken within a safety distance.

The peak particle velocity at any point outside the crater zone at a distance x from ground zero is given by

$$PPV = \frac{4\pi D_p D r_0^3 A^2 l}{\rho V_p x^2 \left[\frac{4D\sqrt{A^2 - 1}}{(A^2 - 2)} + (A^2 - 2) \right]}, \quad (2.4)$$

where V_p is the P-wave velocity in the rock, $A = V_p/V_s$ and V_s is the S-wave velocity in the rock; ρ is the density of the rock; r_0 and D are the radius and depth of the hole, respectively; D_p is the denotation pressure of the explosive and l is the length of the column charge (Gupta et al, 1988).

The vertical PPV of the earth's surface will produce an equivalent particle velocity in the air which results in a peak pressure in the air, PAP, given by

$$PAP = \rho \cdot c \cdot PPV = K \cdot PPV, \quad (2.5)$$

where $K = \rho c$ is the air impedance. Under normal temperature and atmosphere conditions K has the value $622.7973 \text{ kg/m}^2\text{s}$ (Gupta et. al, 1988).

Predictions of PPV and PAP with offset distance from buried dynamite are computed using Equations 2.4 and 2.5 and the parameters listed in Table 2.1. The rock properties in Table 2.1 are characteristic of sandstones. The specifications for the type of explosive in Table 2.1 are taken from Gupta et al. (1988). Figure 2.6 shows PPV and PAP curves as a function of distance from a buried explosion. The vertical line at 15 m indicates the boundary of the crater zone ($x=D$). The range of offsets is from 15.1-225 m ($x>D$). Therefore, the maximum and minimum values in the curves occur at 15.1 m and 225 m, respectively.

Table 2.1. Parameters for the prediction of PPV and PAP from a buried explosion.

PARAMETER	VALUE
D	15m
r_0	50mm
l	1m
V_p	3000 m/s
V_s	1875 m/s
ρ	2700 kg/m ³
D_p	4.443 x 10 ⁸ kg/m ²
V_p/V_s	1.574
K	622.7973 kg/m ² s

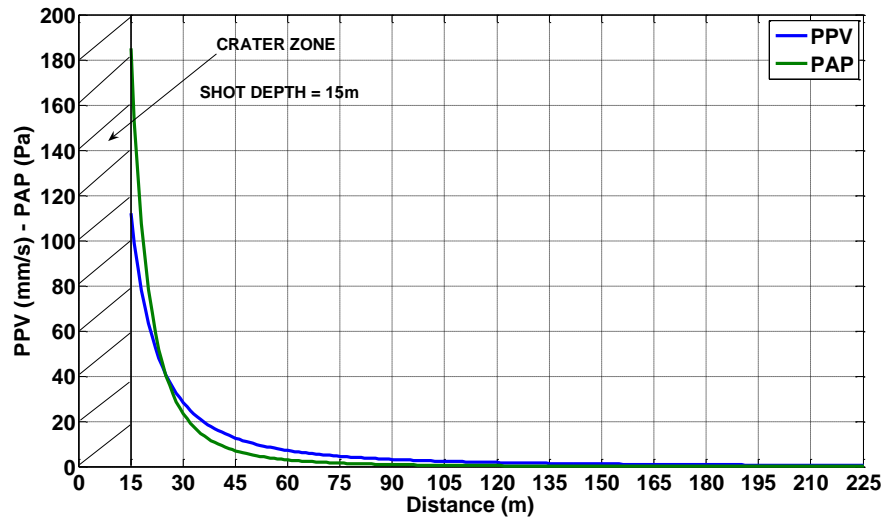


Figure 2.6. Prediction of PPV and PAP with offset distance from a buried explosion. The vertical line at 15 m indicates the boundary of the crater zone.

2.3. Air blast propagation

The pressure P received at a height h_r , above an impedance boundary from a continuously emitting point source at height h_s , and a distance r_1 away is given by

$$\frac{P}{P_0} = \frac{1}{k_1 r_1} e^{-ik_1 r_1} + \frac{1}{k_1 r_2} Q e^{-ik_1 r_2}, \quad (2.6)$$

where P_0 is a reference pressure level near the source, k_1 is the wavenumber in the air, and r_1 and r_2 are the path lengths of the direct and reflected waves, respectively (Albert and Orcutt, 1990). The first term gives the pressure from the direct wave: the second gives the contribution from the boundary

2.4. Acoustic-to-seismic transfer function

In the last 20 years, researchers from the environmental, acoustical and engineering communities have contributed to the development of the seismic-to-acoustic coupling ratio

theory as a quick and cost-effective, non-invasive method for investigating the bulk properties and layering of near-surface soils using acoustic sources (Harrop and Attenborough, 1998).

There is an ambiguity in using the terms seismic-to-acoustic and acoustic-to-seismic. The former refers to the coupling ratio itself, that is, the ratio of induced particle velocity to incident acoustic pressure at the surface; the later refers to the mechanism of energy transfer (coupling) that occurs when a travelling sound wave in the air couples to the ground. The seismic-to-acoustic ratio is given by

$$H = \frac{\text{Particle velocity } \left(\frac{m}{s}\right)}{\text{Incident pressure (Pa)}} = \text{Units of } \left(\frac{m}{s \cdot Pa}\right), \quad (2.7)$$

which basically depends on the physical properties and characteristics of the soil such as porosity, density, thickness of the surface layer, etc. In other words, the acoustic-seismic impedance has a dramatic effect on the level of ground vibration induced by a given sound pressure (Sabatier et al., 1986).

CHAPTER TWO: GROUND VIBRATION AND AIR PRESSURE MONITORING OF SEISMIC SOURCES: IMPLICATIONS FOR SEISMIC WORK AND THE ENVIRONMENT

3.1. Introduction

Seismic operations are undertaken to satisfy exploration goals while respecting the environment. However, actual monitoring of ground vibration and air overpressure generated by seismic sources during land data acquisition is not a standard procedure. The standard methodology followed by most of the seismic contractors in Canada and worldwide is to apply safe offsets between the seismic sources and facilities or other infrastructure. This requires using standard charts whose values are collected empirically and rely on best practices around the world. Such charts are published by the International Association of Geophysical Contractors (IAGC), and in Canada, the Canadian Association of Geophysical Contractors (CAGC) plays the analog role (see Table 3.1). However, as suggested by Rappin et al. (2007), *“the use of available standard reference charts is not optimal as it will define cautiously large safety distances, usually too conservative. In addition, their use does not ensure that arguments or lawsuits can be avoided in case of damage.”*

Rappin et al. (2007) proposed a monitoring methodology based on a calibration stage followed by real-time monitoring of ground vibrations during seismic operations. The early stage produces calibrated reference curves of the ground response to the seismic energy sent into the ground (i.e., either dynamite or Vibroseis), quantitatively expressed in terms of the PPV. According to Rappin et al. (2007), these calibrated curves can be used to refine the safety distances to specific objects. Because PPV limit values are now known for

sensitive areas, they can be used during seismic acquisition for real-time monitoring by means of 3-C geophones placed near the objects.

Table 3.1. Stand-off distances applied by the CAGC.

Canada Oil and Gas Geophysical Operations Regulations (SOR/96-117)			
Facility	Stand-off distance		
	2 > kg dynamite	2 < kg dynamite < 4	Vibroseis
Dam	64 m	90 m	100 m
Oil or gas well	32 m	45 m	15 m
Pipeline	32 m	45 m	15 m
Structure with concrete base	64 m	90 m	50 m
Residence	64 m	90 m	50 m
Area of public congregation	64 m	90 m	50 m
Water well	64 m	90 m	100 m

The industrial and cultural impact of vibration monitoring approaches during seismic operations could be significant. On the one hand, seismic data quality can be improved as a function of reducing gaps in the fold. In addition, the calibrated curves of ground response could be presented as reference material in case of contention between the seismic contractor and complainant (Rappin et al., 2007). In other cases, measurement of PPV versus distance is legally accepted to prove that seismic operations are not causing damage to nearby objects (WorleyParson Komex, personal communication, 2007). On the other hand, it might not be cost-prohibitive since only a few extra channels and a small additional crew or specialized contractor would be required. Vibration monitoring of seismic sources can be used to achieve an optimal trade-off between seismic data quality, safe operations, and environmental protection.

The aim of this chapter is to describe the measurements and typical instrumentation involved in vibration monitoring. A case study is also presented of vibration monitoring during a seismic exploration program at Nanton, Alberta, in which dynamite and Vibroseis sources were monitored in the proximity of the valuable water springs in the Nanton area.

3.2. Instrumentation and PPV/PAP measurements

A vibration monitoring program requires measurements of particle velocities in three directions because several features are responsible for the variation of these at a given distance. For instance, the geological and soil conditions, the type of seismic source, the type of waves, and the wavefield spreading geometry, affect the magnitude and direction of propagation of induced ground vibrations. Therefore, the strongest ground vibrations can occur in any of the three directions (i.e., vertical, longitudinal, and transverse). In the case of air vibrations, these are transmitted through the air; hence, weather conditions replace geology as a principal variable (Sharp and Yule, 1998).

Typical instrumentation for vibration monitoring consists of a triaxial geophone, a microphone and the recording system, referred to as vibration monitor. This configuration is typical for peak particle velocity and air-overpressure measurements. However, other type of sensors could be used such as accelerometers or hydrophones, depending on the physical variable to be measured and the site environment (e.g., land, water, swamp, etc.). The sampling frequencies are larger than those used in seismic data acquisition, therefore sampling frequencies in the range 1 kHz - 16 kHz are not uncommon.

The PPV is the most accepted and used indicator of vibration levels. Most regulations and standards prescribe vibrations thresholds in terms of the PPV. For each recorded

waveform, the maximum particle velocity over the total recorded time is regarded as the peak particle velocity (see Figure 3.1). This type of particle velocity must not be confused with the velocity with which the wave propagates through the medium (i.e., information of interest in seismic exploration).

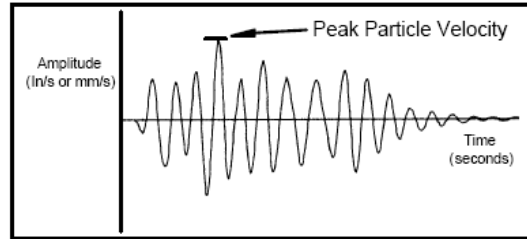


Figure 3.1. Peak particle velocity definition (From Instanetel, 2001).

The peak vector sum (PVS) is often preferred over the PPV because it reflects the effect of the other two components. Both have units of mm/s with slightly different magnitudes. In most blasting, the PVS occurs at about the same time as the PPV of one of the components, but the addition of the other two components increases its magnitude. In other words, the peak vector sum represents the resultant particle velocity magnitude. Recall from linear algebra that the magnitude of the resultant vector is always greater than the magnitude of any single component. The PVS is computed by squaring and summing the samples of each component at a time t , and then taking the square root of the sum. The maximum of these sums, over the appropriate time window, is the peak vector sum and does not necessarily occur at the PPV of an individual waveform.

Air vibration is measured with a microphone whose output units are pressure (Pascals). Peak Sound Pressure Level (PSPL) is the analogous to PPV and determines the maximum overpressure. It is often referred to as air-overpressure because microphones measure pressure changes with respect to the atmospheric pressure level. This pressure amounts to

roughly 100,000 Pa (1 atmosphere; 14.6954 psi). Then, sound pressure is defined as the difference between the actual instantaneous pressure due to sound and the atmospheric pressure (Carley, 2004). Therefore, sound pressure has a much smaller value than the one corresponding to the atmospheric pressure.

The zero-crossing frequency (ZC frequency) is an approximation of the frequency of the peak particle velocity. It is computed by taking the inverse of the period between two consecutive zero crossings at the peak. It is an approximate measurement because the peak in a waveform may be the result of a band of frequency components.

3.3. Vibration event report

Figure 3.2 shows an example of a vibration event report from a dynamite shot, which includes an informative section with the date and time of the acquisition, site location, file name, etc. The actual measurements are organized by sensor type. For the microphone, the peak sound pressure level (PSPL) in Pascal (Pa), the zero-crossing frequency in Hertz, the type of scale (linear or weighted), and sensor-check status are included. For the triaxial geophone, each component is checked and recorded independently. PPV (mm/s), ZC frequency (Hz), peak time (s), peak acceleration (g), peak displacement (mm) and peak vector sum (mm/s) are calculated for each channel. The waveforms are also plotted along with the sensor-check curves. Finally, recorded PPV values are plotted within a compliance reference chart. This reference is based on available vibration regulations, which are different from country to country. The report in Figure 3.2 uses U.S.A. USBM/OSMRE but other options can be chosen as reference.



Event Report

Date/Time Manual at 22:21:22 July 20, 2007
 Range Geo :254 mm/s
 Record Time 10.0 sec at 1024 sps

Serial Number 1287 V 5.52 BlastMate II/677
 Battery Level 6.4 Volts
 Calibration June 15, 2007 by Instantel Inc.
 File Name C287BRPK.RM0

Notes

Location: blast site
 Client: compton petroleum corporation
 User Name: Worley Parsons komex
 Converted: July 20, 2007 16:27:39 (V8.12)

Extended Notes

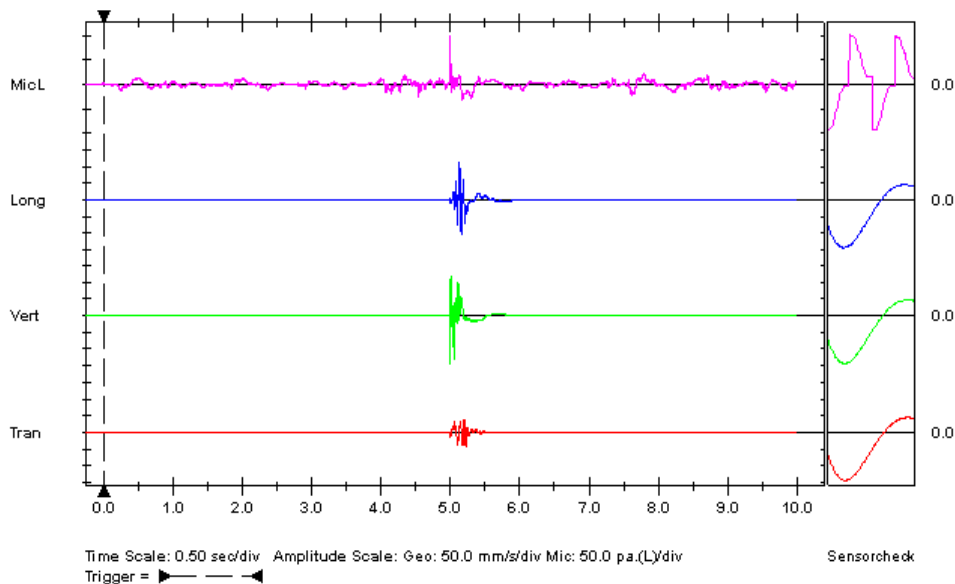
sandbagged and pointed at road ambient measurement

Post Event Notes

Microphone Linear Weighting
 PSPL 98.5 pa.(L) at 5.001 sec
 ZC Freq 12 Hz
 Channel Test Passed (Freq = 20.0 Hz Amp = 219 mv)

	Tran	Vert	Long	
PPV	40.1	145	113	mm/s
ZC Freq	19	43	14	Hz
Time (Rel. to Trig)	5.225	5.001	5.133	sec
Peak Acceleration	1.43	13.7	4.35	g
Peak Displacement	0.464	1.87	1.20	mm
Sensorcheck	Passed	Passed	Passed	
Frequency	7.8	8.0	8.2	Hz
Overswing Ratio	3.5	3.4	3.3	

Peak Vector Sum 145 mm/s at 5.001 sec



Printed: November 6, 2007 (V 8.12 - 8.12)

Format Copyrighted 2006-2007 Instantel, a division of VeriChip Corporation

Figure 3.2. Vibration and air-overpressure monitoring of dynamite shot. The vibration monitor system was located 5 m distance from the explosion. The PPV occurred at 5.001 s in the vertical component. The PSPL also occurred at the same time. The PPV in the horizontal components occurred at slightly later times being smaller than the vertical PPV. Note that the vibrations at such small distance reach threshold levels.

3.4. Regulations

The United States Bureau of Mines (UBSM) RI 8507 standard states that for frequencies between 3 and 10 Hz, the PPV should be kept below a threshold level of 13 mm/s to reduce the potential of damage. The threshold level increases with increasing frequency to 51 mm/s at 40 Hz and remains constant at 51 mm/s for frequencies above 40 Hz (Kalinski, 2007).

3.5. A case study: Nanton, Alberta

A vibration monitoring of a seismic exploration program was conducted in the area around Nanton, Alberta. The survey area was in the proximity (but more than 1km) to water springs which are economically important for the Nanton community. There was a concern about potential damage to the water springs from seismic activities (Stewart, personal communication, 2007). The aim of the project was to monitor vibrations near the springs as generated by Vibroseis and dynamite sources.

The methodology consisted of two monitoring points. One monitor system was placed at the Nanton water spring to continuously record ambient vibrations and the PPV for each of the shot points. The second vibration monitor was placed at a specific shot point from where all shots within a single seismic line were monitored. The methodology was repeated for all seismic lines in the survey.

The Vibroseis array consisted of four buggy-mounted Mertz model 8 vibrators. There were six sweeps (8-125 Hz) of 18s length each. Dynamite shots consisted of 2 kg of buried explosives in holes 15 m deep. The vibration monitor system was a Blastmate II equipped with a single 3-C geophone and a microphone. Both sensors had band-pass responses from

2Hz to 250Hz. All channels were recorded at a sampling rate of 1024 samples per second (1.024 kHz). A 10 s waveform was recorded for a variety of distances between the fixed points and fired shot points. Figure 3.3 shows the monitoring area and vibration monitor setup.



Figure 3.3. Vibration monitor setup (left) and shooter ready to fire a source point (right) (Photos by Dr. Robert Stewart).

3.5.1. *Shock-induced airwave from a buried dynamite explosion*

Figure 3.4 shows the vertical component of ground velocity and the air pressure recorded at 25 m offset from a dynamite test shot (located approximately 2.2 km from the Nanton water spring). The recorded peak particle velocity was 90.4 mm/s in the vertical component with dominant frequency of 19.2 Hz. The peak air pressure was 30.5 Pa (123 dB) with dominant frequency of about 2.44 Hz. The cross-correlation of the signals suggests that there is strong negative correlation and that the air-pressure signal is shifted with respect to the particle velocity signal. From the upper plot of Figure 3.4, there exists a difference in phase.

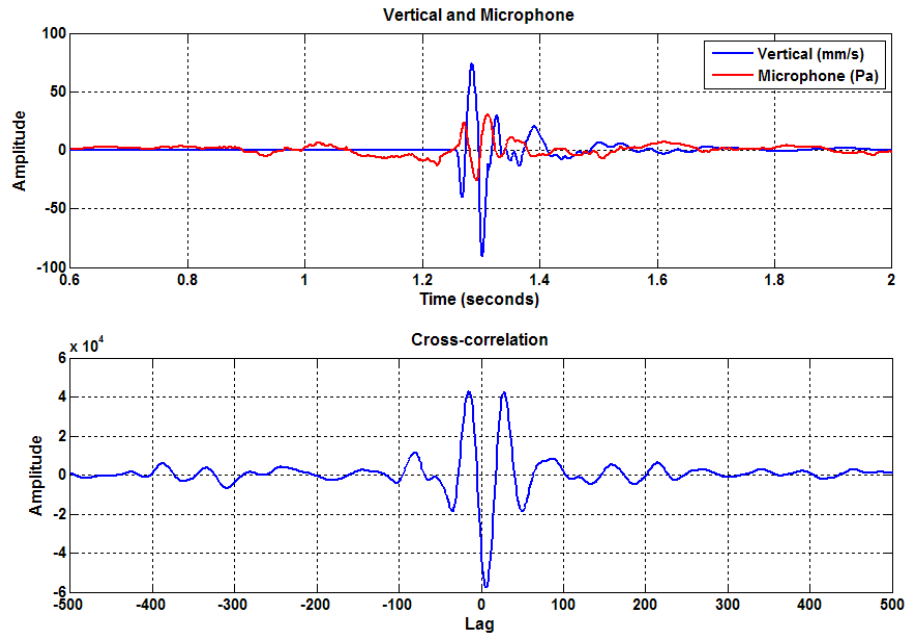


Figure 3.4. Vibration and air-overpressure monitoring of dynamite shot at 25 m offset (top). Cross-correlation of vertical ground velocity and air pressure at the surface (bottom).

Figure 3.5 shows peak particle velocity and peak overpressure measurements as a function of distance from a series of buried dynamite shots within a seismic line. Note that the PPV and POP values decreased with offset distance, in agreement with the theory of PPV and POP studied in Chapter 2.

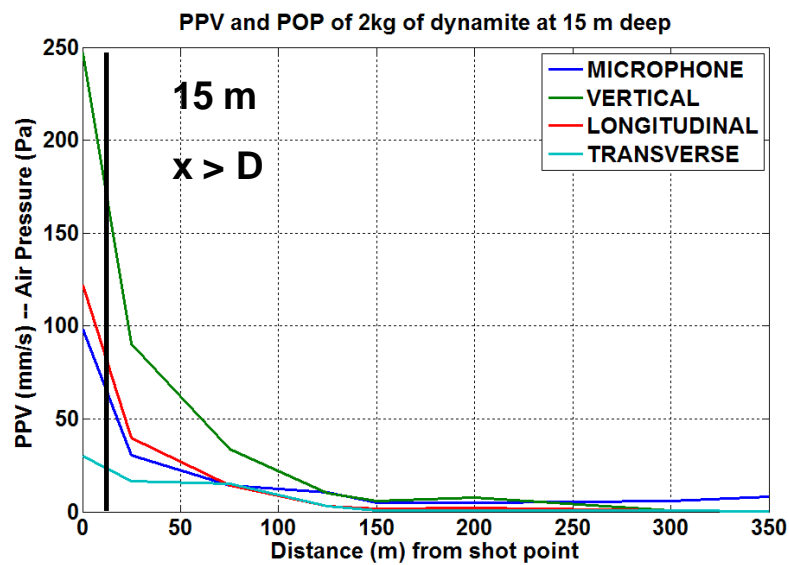


Figure 3.5. PPV and POP monitoring of dynamite shots as a function of distance.

3.5.2. *Vibroseis*

Figure 3.6 is an event report for the Vibroseis shot point monitored at a distance of 5 m. The Vibroseis array moved in the south direction along a seismic line running north to south. The responses of the triaxial geophone and the microphone are quite different from those recorded for the dynamite case. Such responses were expected given the different nature and mechanism of energy transmission of the sources. An important feature in this event report is the magnitude of the PPV in the transverse component, which is greater than the PPV recorded in the vertical and longitudinal components. This is also observed with the monitor placed at 50 m from the Vibroseis trucks. Kalinski (2007) suggested that the use of distance as the only criterion for selecting monitoring points is an oversimplification of the PPV field associated with Vibroseis arrays. In fact, during the Nanton monitoring program there was a suspected zone of constructive interference (see Figure 3.7). A vibration monitor placed on a gravel road at a distance of 50 m from the Vibroseis array recorded a PSPL of 30.5 Pa (123.66 dB) with 2.5Hz dominant frequency, which is larger than the PSPL recorded at 5m offset along the same road (i.e., 19 Pa or 119 dB with 2.88 Hz dominant frequency). However, the microphone at 5 m offset may have been shielded by the truck. On the other hand, there may be some sort of constructive interference occurring near the vibration monitor placed at 50 m. Certainly, events of this magnitude may cause some disturbance to nearby humans, even though the dominant frequencies are in the infrasound band when Vibroseis trucks operate in urban environments. Coupling phenomena at the air-earth interface provide a possible explanation for constructive interference. Air-coupled surface waves and ground-coupled air waves may cause PPV or PSPL amplification as a result of resonance coupling at the air-earth interface.



Event Report

Date/Time Manual at 20:01:20 July 21, 2007
 Range Geo :254 mm/s
 Record Time 10.0 sec at 1024 sps

Serial Number 1287 V 5.52 BlastMate II/677
 Battery Level 6.4 Volts
 Calibration June 15, 2007 by InstanTel Inc.
 File Name C287BRR8.Y80

Notes
 Location: recording station 1
 Client: compton petroleum corporation
 User Name: Worley Parsons komex
 Converted: July 21, 2007 16:10:44 (\8.12)

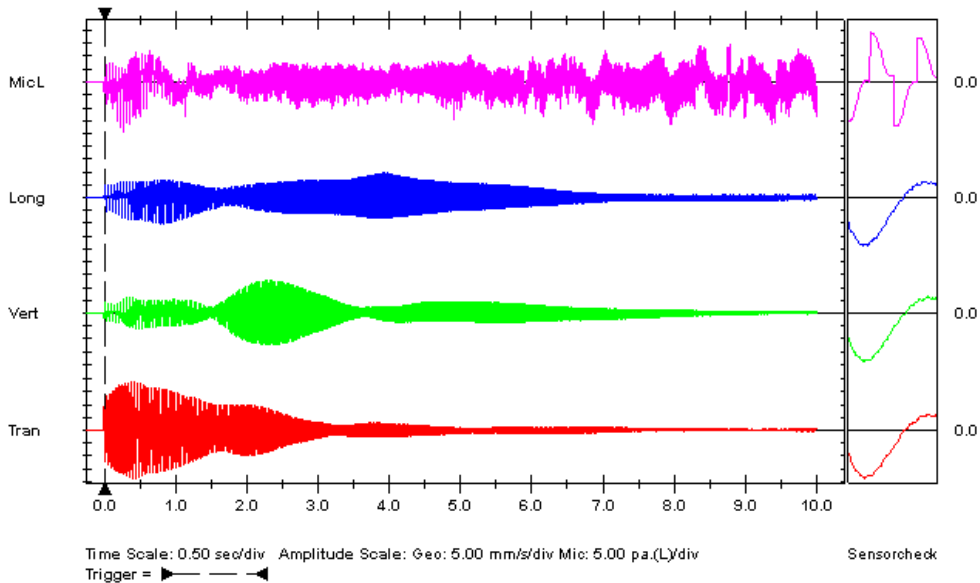
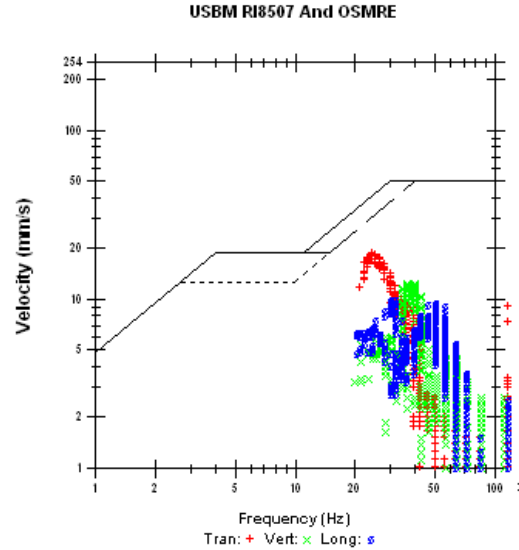
Extended Notes
 sandbagged and pointed at road

Post Event Notes

Microphone Linear Weighting
 PSPL 19.0 pa.(L) at 0.266 sec
 ZC Freq 64 Hz
 Channel Test Passed (Freq = 20.0 Hz Amp = 218 mv)

	Tran	Vert	Long	
PPV	18.8	12.7	10.0	mm/s
ZC Freq	24	37	30	Hz
Time (Rel. to Trig)	0.385	2.269	0.801	sec
Peak Acceleration	0.451	0.345	0.345	g
Peak Displacement	0.129	0.0556	0.0515	mm
Sensorcheck	Passed	Passed	Passed	
Frequency	8.0	7.8	8.2	Hz
Overswing Ratio	3.3	3.1	3.1	

Peak Vector Sum 19.3 mm/s at 0.446 sec



Printed: November 6, 2007 (\8.12 - 8.12) Format Copyrighted 2006-2007 InstanTel, a division of VeriChip Corporation

Figure 3.6. Vibration and air-overpressure monitoring of Vibroseis source. The vibration monitor system was located 5 m distance from the Vibroseis array. The PPV occurred early in the transverse component, followed by the PPV on the longitudinal, and finally on the vertical. The PSPL was 19 Pa at 0.266 s. Note that none of the components reach a critical vibration level with respect to USBM and OSRME standards.



Event Report

Date/Time Manual at 20:04:31 July 21, 2007
 Range Geo :254 mm/s
 Record Time 10.0 sec at 1024 sps

Serial Number 1287 V 5.52 BlastMate II/677
 Battery Level 6.4 Volts
 Calibration June 15, 2007 by Instantel Inc.
 File Name C287BRR9.3JO

Notes

Location: recording station 1
 Client: compton petroleum corporation
 User Name: Worley Parsons komex
 Converted: July 21, 2007 16:10:44 (V8.12)

Extended Notes

sandbagged and pointed at road

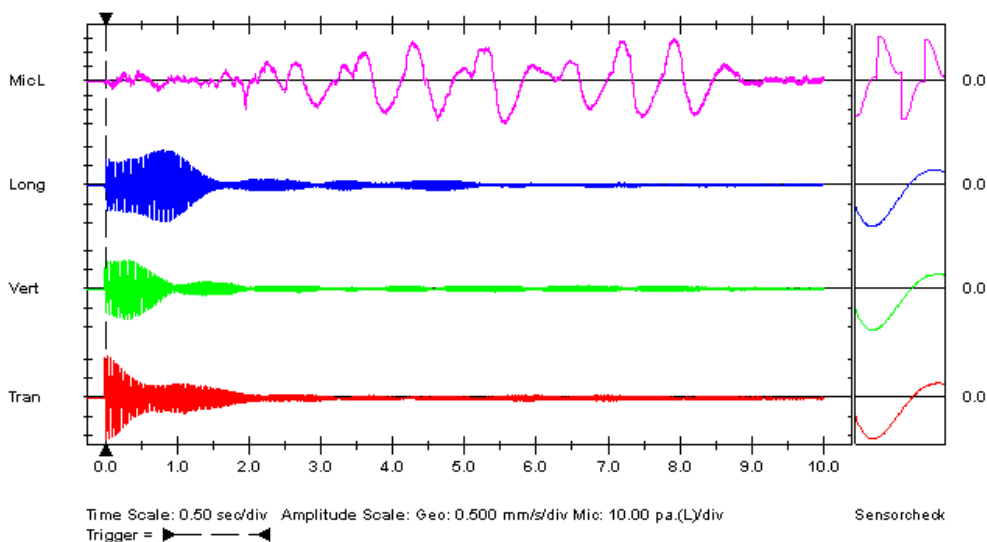
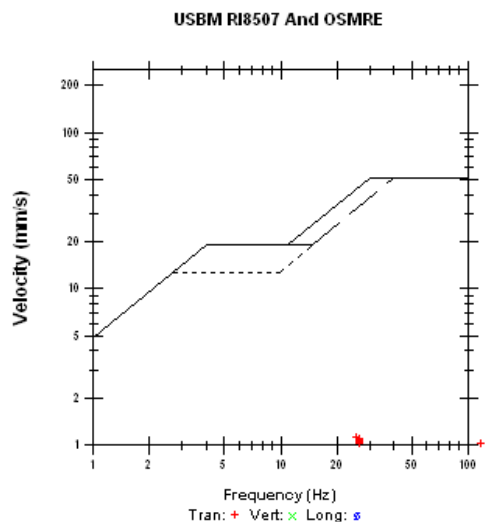
Post Event Notes

Microphone Linear Weighting
 PSPL 30.5 pa.(L) at 5.557 sec
 ZC Freq N/A
 Channel Test Passed (Freq = 20.0 Hz Amp = 220 mv)

	Tran	Vert	Long	
PPV	1.13	0.778	0.953	mm/s
ZC Freq	24	28	30	Hz
Time (Rel. to Trig)	0.018	0.278	0.798	sec
Peak Acceleration	0.0199	0.0166	0.0199	g
Peak Displacement	0.00719	0.00459	0.00493	mm
Sensorcheck	Passed	Passed	Passed	
Frequency	8.0	8.1	8.3	Hz
Overswing Ratio	3.5	3.4	3.2	

Peak Vector Sum 1.32 mm/s at 0.017 sec

N/A: Not Applicable



Printed: November 7, 2007 (V 8.12 - 8.12)

Format Copyrighted 2006-2007 Instantel, a division of VeriChip Corporation

Figure 3.7 Vibration and air-overpressure monitoring of Vibroseis. The vibration monitor was located 50 m distance from the Vibroseis array. PPV for the three components are very small. However, the PSPL was 30.5 Pa at 5.557s. Most interesting is the microphone waveform with dominant low-frequency content.

Figure 3.8 is an event report of a histogram recorded over 12.75 min at the water spring while shooting, with the closest dynamite shot at about 1.6 km. A histogram is computed by recording a number of time intervals. For each interval, the monitor calculates the maximum positive and negative peaks, the frequency of the largest peak, and one peak vector sum. For each channel, the maximum peak, its frequency, and the largest peak vector sum from all intervals are calculated over the entire event. Figure 3.9 shows a histogram of natural vibrations recorded at the water spring few days before seismic activities started. Peak particle velocities in the vertical and longitudinal components are equal in both histograms despite they were recorded in different days. The PPV in the transverse component is slightly larger (i.e., 0.0794 mm/s) for the histogram of natural vibrations than the PPV for the histogram of shots (i.e., 0.0635 mm/s). This implies that ground vibrations induced by shooting are less than the natural activity. Moreover, peak sound pressure levels did increase a little while shooting, but this was largely attributable to other ambient vibrations such as those generated by road traffic, heavy vehicles, construction machinery, etc. Therefore, the 1.6 km limit stand-off distance creates vibrations that are below natural background levels as measured at the water spring.



Event Report

Histogram Start Time 23:33:17 July 29, 2007 Serial Number 1287 V 5.52 BlastMate II/677
 Histogram Finish Time 23:46:00 July 29, 2007 Battery Level 6.3 Volts
 Number of Intervals 153 at 5 seconds Calibration June 15, 2007 by Instantel Inc.
 Range Geo :7.92 mm/s File Name C287BS6C.3H0
 Sample Rate 1024sps

Notes

Location: nanton sping2
 Client: compton petroleum corporation
 User Name: Worley Parsons komex
 Converted: July 30, 2007 10:07:41 (V8.12)

Extended Notes

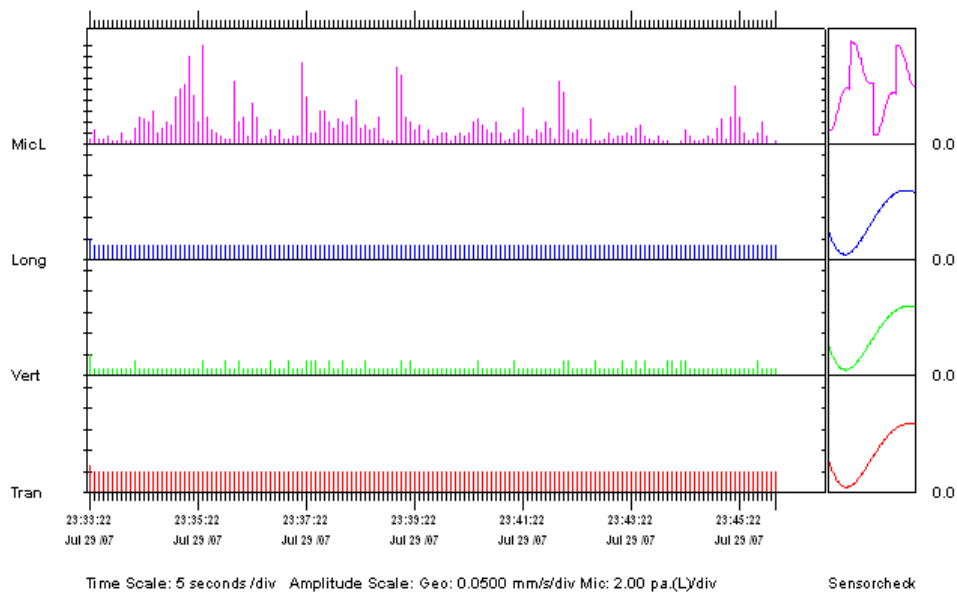
sandbagged and pointed at line

Post Event Notes

Microphone Linear Weighting
 PSPL 18.0 pa.(L) on July 29, 2007 at 23:35:27
 ZC Freq 4.0 Hz
 Channel Test Passed (Freq = 20.0 Hz Amp = 216 mv)

	Tran	Vert	Long	
PPV	0.0635	0.0476	0.0476	mm/s
ZC Freq	15	>100	>100	Hz
Date	Jul 29 /07	Jul 29 /07	Jul 29 /07	
Time	23:33:22	23:33:22	23:33:22	
Sensorcheck	Passed	Passed	Passed	
Frequency	7.8	8.0	8.3	Hz
Overswing Ratio	3.4	3.4	3.2	

Peak Vector Sum 0.0794 mm/s on July 29, 2007 at 23:33:22



Printed: November 6, 2007 (V8.12 - 8.12) Format Copyrighted 2006-2007 Instantel, a division of VeriChip Corporation

Figure 3.8. Histogram recorded at the Nanton water spring for a series of dynamite shots. The nearest shot to the monitor station was at about 1.6 km.



Event Report

Histogram Start Time 22:18:21 July 20, 2007 Serial Number 1291 V 5.52 BlastMate II/677
 Histogram Finish Time 22:42:19 July 20, 2007 Battery Level 6.5 Volts
 Number of Intervals 288 at 5 seconds Calibration July 10, 2007 by Instanter Inc.
 Range Geo :7.92 mm/s File Name C291BRPK.MLD
 Sample Rate 1024sps

Notes

Location: Water Spring
 Client: Compton Petroleum Corporation
 User Name: Worley Parsons Komex
 Converted: July 20, 2007 20:52:21 (V8.12)

Extended Notes
 station1 - test blast 1

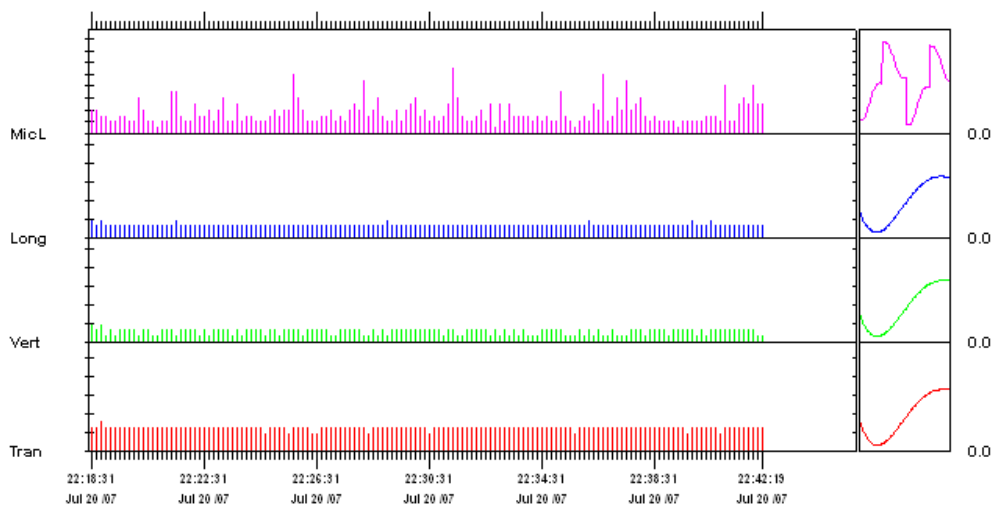
Post Event Notes

Microphone Linear Weighting
 PSPL 5.50 pa(L) on July 20, 2007 at 22:31:16
 ZC Freq N/A
 Channel Test Passed (Freq = 20.0 Hz Amp = 229 mv)

	Tran	Vert	Long	
PPV	0.0794	0.0476	0.0476	mm/s
ZC Freq	N/A	>100	N/A	Hz
Date	Jul 20 /07	Jul 20 /07	Jul 20 /07	
Time	22:18:51	22:18:26	22:18:26	
Sensorcheck	Passed	Passed	Passed	
Frequency	8.0	8.0	8.1	Hz
Overswing Ratio	3.8	3.6	3.7	

Peak Vector Sum 0.0953 mm/s on July 20, 2007 at 22:18:51

N/A: Not Applicable



Time Scale: 10 seconds /div Amplitude Scale: Geo: 0.0500 mm/s/div Mic: 1.000 pa.(L)/div

Sensorcheck

Printed: November 15, 2007 (V8.12 - 8.12)

Format Copyrighted 2006-2007 Instanter, a division of VeriChip Corporation

Figure 3.9. Histogram of natural vibrations recorded at the Nanton water spring nine days before shooting.

Time-frequency representations of the three ground motion components and the air vibration component induced by the Vibroseis source were computed using the Gabor transform, a particular case of the windowed, short-time Fourier transform (refer to Chapter 6 for further explanation). This analysis revealed the harmonic distortion of the signals produced by the Vibroseis source. The microphone output signal shows the fundamental frequency plus five high-order harmonics (see Figure 3.10). The ground motion signals show the fundamental frequency and only two high-order harmonics (see Figure 3.11, 3.12 and 3.13). For all cases, the high-order harmonics have low energy in comparison to the fundamental. However, the existence of harmonics in the recorded signals demonstrates that the transfer of energy from the vibrator to the earth is not perfect, and some of the energy is propagating as ground and air vibrations. Further analysis of the frequency harmonics may give additional information about the source-generated noise.

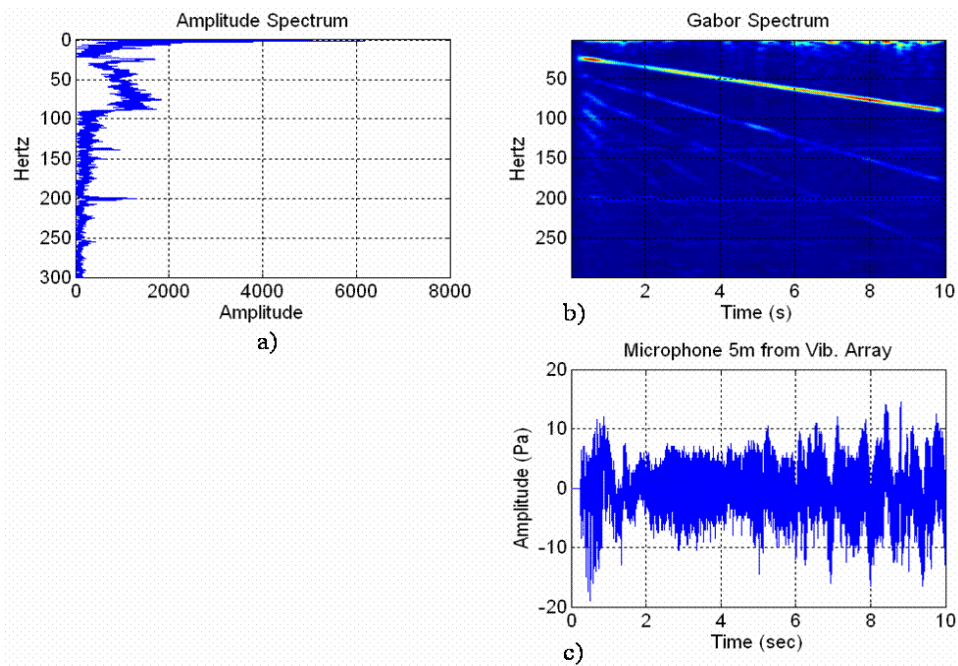


Figure 3.10. a) Amplitude spectrum, b) Gabor transform in the time-frequency space, and c) time domain representation of the microphone record. Note that there exist high-order harmonics in the signal.

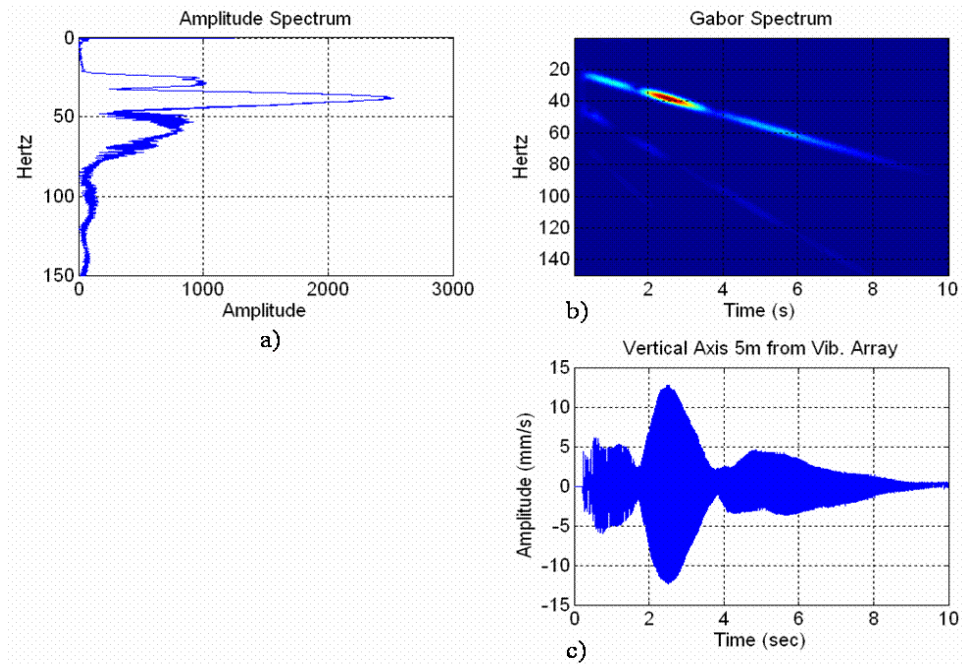


Figure 3.11. a) Amplitude spectrum, b) Gabor transform in the time-frequency space, and c) time domain representation of the geophone vertical component. Note there are two high-order frequency harmonics.

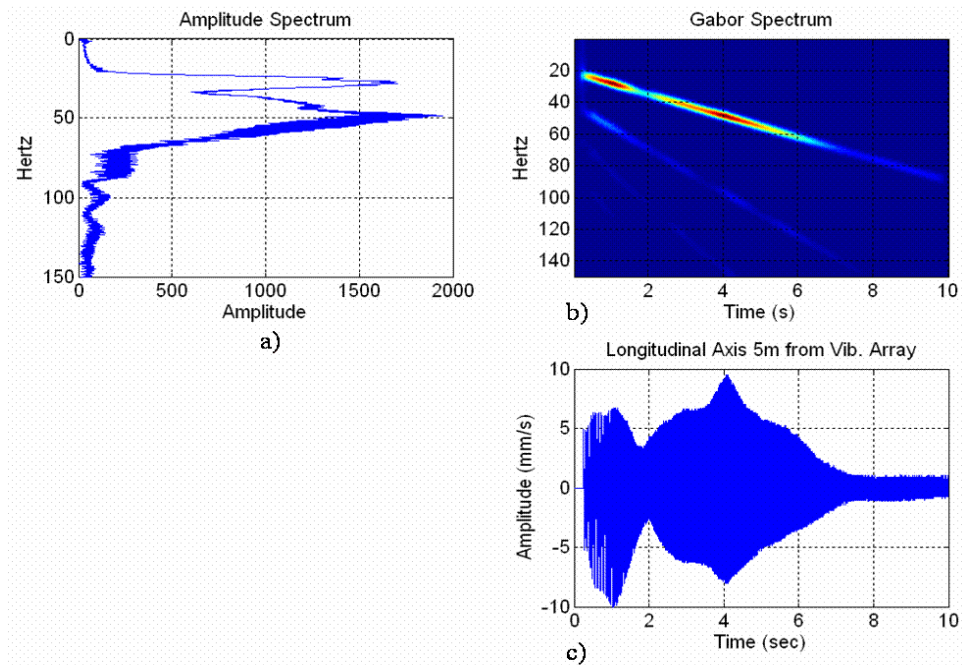


Figure 3.12. a) Amplitude spectrum, b) Gabor transform in the time-frequency space, and c) time domain representation of the geophone longitudinal component. Note there are two high-order frequency harmonics.

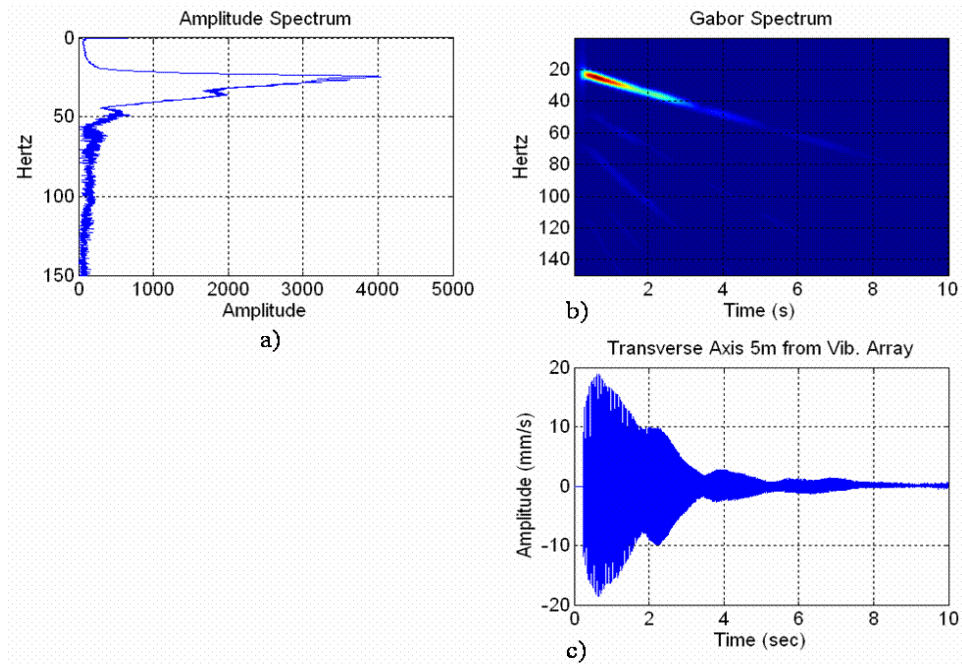


Figure 3.13. a) Amplitude spectrum, b) Gabor transform in the time-frequency space, and c) time domain representation of the geophone transverse component. Note there are two high-order frequency harmonics.

CHAPTER THREE: FIELD COMPARISON OF 3-C GEOPHONES AND MICROPHONES TO HIGH-PRECISION BLASTING SENSORS

4.1. Introduction

It is well known in seismic exploration that the geophone output is a voltage and not an actual magnitude of ground velocity (Hons, 2008). According to geophone modelling results by Hons (2008), the geophone output is not exactly ground velocity. Instead, it is a mix of amplitudes and phase rotations that is in a “geophone domain”. Although a geophone shows a fairly flat frequency response to ground velocity above the resonant frequency, it cannot be considered a “true velocity sensor” because low frequencies (below resonance) are recorded with smaller amplitudes relative to the amplitudes at high frequencies, and there are varying phase rotations up to 100 Hz or more (Hons, 2008).

Therefore, it is of interest to seismologists to compare different types and models of ground motion sensors to assess their benefits and drawbacks in terms of frequency response, phase distortion and operational limits. For instance, Hons (2008) recently analyzed and compared the system response of conventional geophones to the system response of MEMS accelerometers both in laboratory and field tests. Despite their limitations for reliable low-frequency recordings (i.e. <10 Hz), conventional coil geophones have been used as the standard sensors since the beginning of seismic exploration largely because they are self-powered, inexpensive and reliable (Hons, 2008). Although geophones with improved low-frequency response are commercially available, they are expensive, heavy and large, and consequently impractical for large-scale seismic acquisition (Stewart, personal communication, 2008). Nevertheless, Stewart et al., (1996) presents a case of a

broadband 3C-3D seismic experiment over the Blackfoot field in Southern Alberta that recorded reliable low-frequency seismic data using large 2 Hz geophones.

Most applications of geophones with improved low-frequency response are found in blasting monitoring and earthquake seismology. In this chapter, two conventional seismic exploration 3-C geophones (i.e., 10 Hz resonant frequency) are compared to a high-precision calibrated 3-C geophone (i.e., attached to a blast monitor system). The performance of these geophones is evaluated in terms of their peak particle velocity amplitudes. To achieve this goal, a very short seismic line was deployed west of the University of Calgary campus during the summer of 2008 (Figure 4.1) which included two different seismic sources, three different geophones and four different microphones (Figure 4.2).



Figure 4.1. Location map of the test site located west of the University of Calgary Campus. The direction of the seismic line was northeast-southwest (from Google maps).

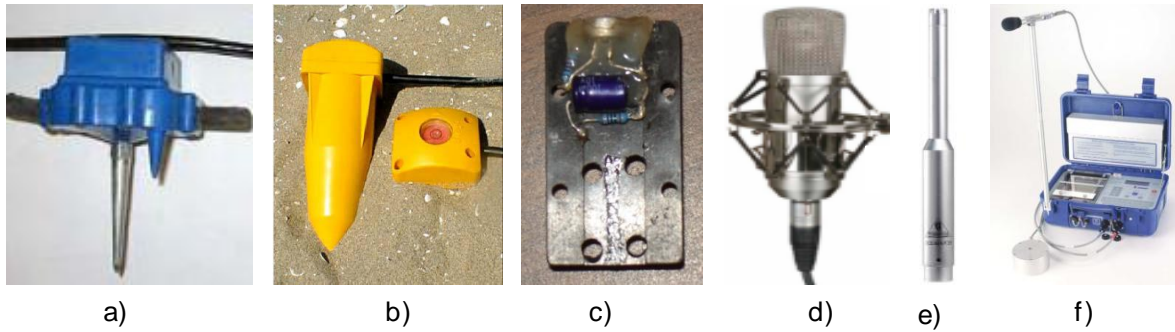


Figure 4.2. Seven sensors were used in the test: a) OyoGeospace GS-3C geophone, b) Input/Output Spike 3C geophone, c) CREWES microphone prototype, d) APEX 435 condenser microphone, e) EMC8000 electret-condenser microphone, and f) Blastmate III unit with two calibrated sensors (3C geophone and microphone).

4.2. Transducer sensitivity

A typical transducer converts physical signals into electrical signals. The magnitude of the transducer output, usually given in volts (V), is determined by the conversion mechanism and a sensitivity factor. For instance, the voltage output from a geophone is directly proportional to the velocity of the coil with respect to the case, scaled by a sensitivity factor given in units of V/m/s. The geophone's sensitivity depends upon the number of loops in the coil and the strength of the magnetic field of the permanent magnet.

Conversion from volts to physical units for a geophone is given by

$$u = \frac{V_{out}}{10^{\frac{gain}{20}} \times 1000 \times sensitivity}, \quad (4.1)$$

where u is particle velocity in m/s, V_{out} is the sensor output in millivolts (mV), $gain$ is the recording system gain given in dB, 1000 is a factor that converts from millivolts to volts and sensitivity is a factor given in V/m/s (Albert, 1993). Similarly, the equation to convert from volts to units of pressure in a microphone is given by

$$p = \frac{V_{out}}{10^{\frac{gain}{20}} \times 1000 \times sensitivity}, \quad (4.2)$$

where p is pressure in Pascal (Pa), V_{out} is the sensor output in mV, gain is the recording system gain given in dB, 1000 is a factor that converts to from millivolts to volts and sensitivity is a factor given in V/Pa (Albert, 1993).

4.3. Instrumentation

4.3.1. 3-C geophones

Two types of 3-C exploration geophones were used in this field study. Twenty-two ION Spike 3-C geophones with SM-24 elements manufactured by Input/Output Inc. and a single Oyo 3-C geophone with GS-20DM elements manufactured by OyoGeospace. The first type has a long case, housing three geophone elements at its bottom. The second type has a large metal spike and a smaller secondary spike to provide a better geophone planting and levelling. These geophones have similar manufacturer's specifications with the actual values listed in Table 4.1. The string of geophones was connected to the Geode Ultra-Light Exploration Seismograph, a product of Geometrics, INC.

Table 4.1. Summary of geophone specifications (Instanfel, 2001; Hons, 2008)

Sensor	Type	Natural frequency	Frequency response	Sensitivity	Damping
ION Spike 3-C	3-C	10 Hz	~10-240 Hz	20.5 V/m/s	0.69
OYO 3-C	3-C	10 Hz	~10-300 Hz	19.7 V/m/s	0.70
Calibrated 3-C geophone	3-C	Not specified	2-250 Hz	Not specified. Returns true amplitude	Not specified

4.3.2. Microphones

The CREWES project designed, manufactured and tested a microphone prototype suited for air pressure measurement recordings using conventional seismic acquisition systems. The main component of this prototype is a Panasonic WM-54 BT microphone (Figure 4.3), still available in the market. It is an electret condenser microphone with theoretical flat frequency response in the range of 20 Hz to 16 kHz (according to the Panasonic specifications sheet) and sensitivity of $-44 \text{ dB} \pm 3 \text{ dB}$ with a reference level of $0 \text{ dB} = 1 \text{ V/Pa}$ (i.e. $-44 \text{ dB} = 6 \text{ mV/Pa}$). In other words, if a sound pressure of 1 Pa impinges on this microphone, the output would be 6 mV. A PP3 9V battery is required to power a single microphone for a period of two to four hours. Two resistors and a capacitor complete the circuit that powers the microphone and amplifies its output. To transmit each microphone output to the seismic acquisition system on a single channel, a single-pin connector (Figure 4.3) was electrically welded to the load resistor connected in series to the condenser. We connected these prototypes to the ARAM Aries 24-bit System (ARAM Systems Ltd.) and the GEODE Exploration Seismograph (Geometrics Inc.) using conventional line cables and single-pin takeouts.



Figure 4.3. CREWES microphone prototype and single-pin connector used to transmit the microphone output to the recording system.

Two additional studio microphones were used. The APEX 435 is a wide-diaphragm condenser microphone with frequency response from 20-20 kHz and cardioid polar pattern (reception pattern). The EMC 8000 is an electret-condenser microphone with frequency response from 15-20 kHz and omnidirectional polar pattern. These microphones are commonly used for professional audio recording and need power from either a battery, a mixing board or a microphone pre-amplifier in the form of “phantom” power (+48 V DC). In this case, a USB-powered audio/MIDI production device, the Digidesign Mbox2, was procured and used for three main tasks: 1) to serve as the “phantom” power provider, 2) pre-amplification, and 3) redirection of its two available analog inputs to their analog outputs.

Microphone connections to the Geode Seismograph are accomplished by using conventional microphone XLR cables and special cables consisting of jack connectors on one end and single-pin geophone connectors on the other. The MBox2 analog inputs receive the analog microphone signals through the XLR cables and then they are internally routed to the analog outputs (Figure 4.4a). By plugging the jack connectors into the Mbox2 analog outputs, the microphones can be connected to any available channel in the Geode by simply plugging the single-pin connector into any takeout. The MBox2 has to be connected to a laptop through a USB port since the PC provides its power (Figure 4.4b). The MBox2 has pre-amplifier gain capabilities which can be applied to the analog inputs and routed to the available analog outputs. However, a disadvantage of the MBox2 is that the pre-amplifier gain control is knob-based and no legend is printed on the front panel. Microphone pre-amplifier gains were chosen so that the control knobs were fixed to the center position. The total gain applied to both microphones is a combination of the MBox2

gain and whatever gain is selected in the Geode Seismograph. Table 4.2 summarizes some relevant microphone specifications.

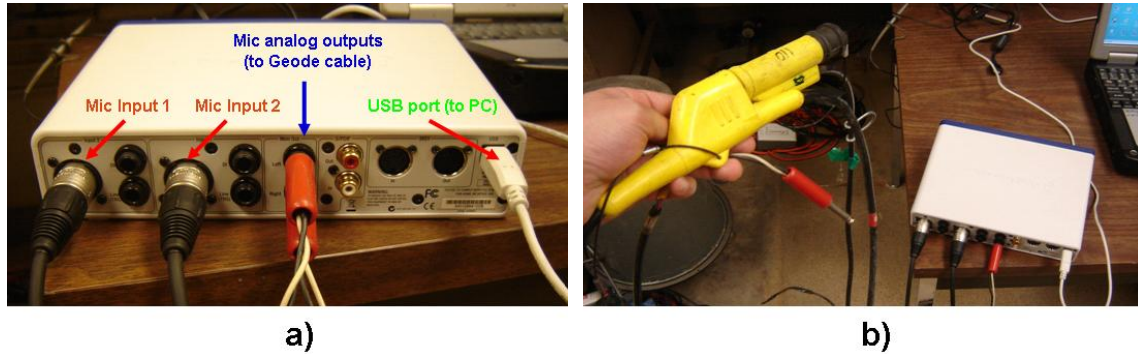


Figure 4.4. a) Two studio microphones were connected to the analog inputs of a Digidesign MBox2 using conventional microphone XLR cables. b) The MBox2 analog outputs were connected to the Geode receiver cable through special cables consisting of jack connectors on one end and single-pin geophone connectors on the other.

Table 4.2. Summary of microphone specifications (from owners' manual)

Sensor	Type	Frequency response	Sensitivity	Power source
Calibrated Microphone	Overpressure microphone	2-250 Hz	Not specified. Returns true amplitude	Blastmate II
CREWES Microphone	Electret- condenser	20 Hz-20 kHz	6 mV/Pa	9V battery
APEX 435 Microphone	Condenser	20 Hz-20 kHz	10 mV/Pa	Phantom (+48V)
EMC 8000 Microphone	Electret- condenser	15 Hz-20 kHz	1 mV/Pa	Phantom (+48V)

4.3.3. Calibrated sensors

Typical instrumentation for vibration monitoring consists of a calibrated 3-C geophone, a calibrated microphone and a portable recording system. Our monitor, the Blastmate III, includes one calibrated 3-C geophone and one calibrated microphone both with band-pass responses from 2-250 Hz. This configuration is typical for PPV and POP measurements. The Blastmate geophone resolution, or minimum recordable amplitude, is 0.0159 mm/s. Its maximum amplitude is limited up to 254 mm/s. The minimum and maximum values for the

calibrated microphone are 0.25 Pa and 500 Pa, respectively, which are equivalent to linear sound pressure levels (SPL) from 88 to 148 dB. The accuracy of the geophone is $\pm 5\%$ or 0.5 mm/s, whichever is larger between 4 and 125 Hz. Microphone accuracy is $\pm 10\%$ or ± 1 dB also between 4 and 125 Hz. Sampling frequencies of the Blastmate III are faster than those typically used in seismic data acquisition with options in the range of 1.024 kHz to 16 kHz.

4.4. Data acquisition

The receiver line was deployed along a roadside and extended 52.5 m in the northeast-southwest direction. The uppermost layer in the near surface was mainly comprised of clay. Soils that are high in clay are sticky when wet, compact easily and stay in rough lumps when dry. There was also some vegetation extending to the west side of the receiver line (Figure 4.5). A number of ION Spike 3-C geophones were planted along the receiver line at a 2.5 m receiver spacing. A small 1-cm deep by 6-cm wide hole was drilled for each ION spike using a gas-powered handheld auger. The seven-sensor test station was located at the northeast-end of the line (Figure 4.6). A schematic diagram of the acquisition layout is shown in Figure 4.7. The test station included an additional OyoGeospace 3-C geophone, an Instantel calibrated 3-C geophone, an Instantel calibrated microphone, an APEX 435 condenser microphone, an EMC 8000 electret condenser microphone and the CREWES microphone prototype. The calibrated sensors were attached to their own portable recorder (Blastmate III). All other sensors were connected to three Geode Ultra-Light Exploration Seismographs. The use of two different recorders imposed an inherent difference between the high-precision and conventional sensors, which was later minimized in data processing. Other logistics and recording issues are further explained below.



a)



b)

Figure 4.5. a) CREWES staff preparing equipment. b) North view of test site. The receiver line was deployed along the vegetation boundary to allow road traffic.

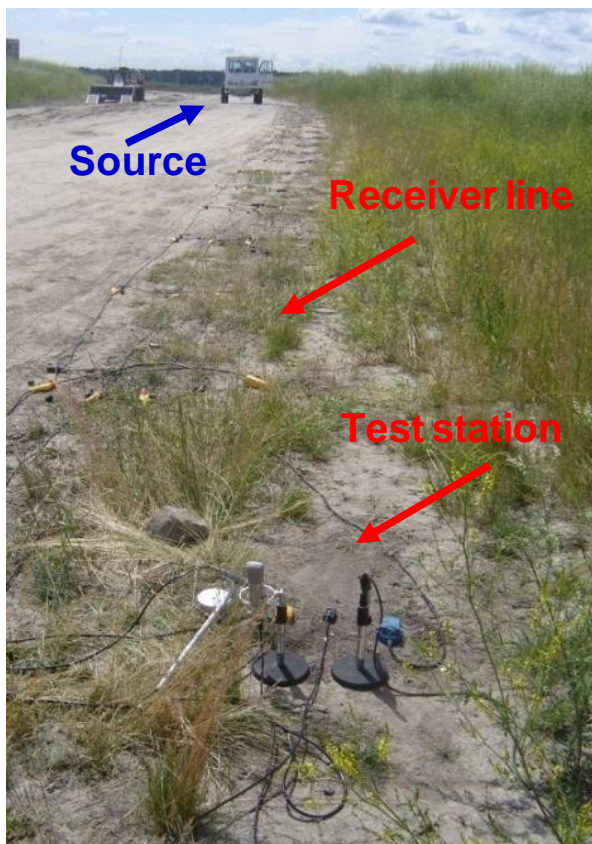


Figure 4.6. Southwest view of the seismic line with the mini Vibe located at shot point one (left) and the seven-sensor test pad located at the northeast end (bottom right). The observer's computer was located about 3.5m north of the test station while the Blastmate monitor was located about 1 m east of the test station (top right) (Photos by Alejandro Alcudia).

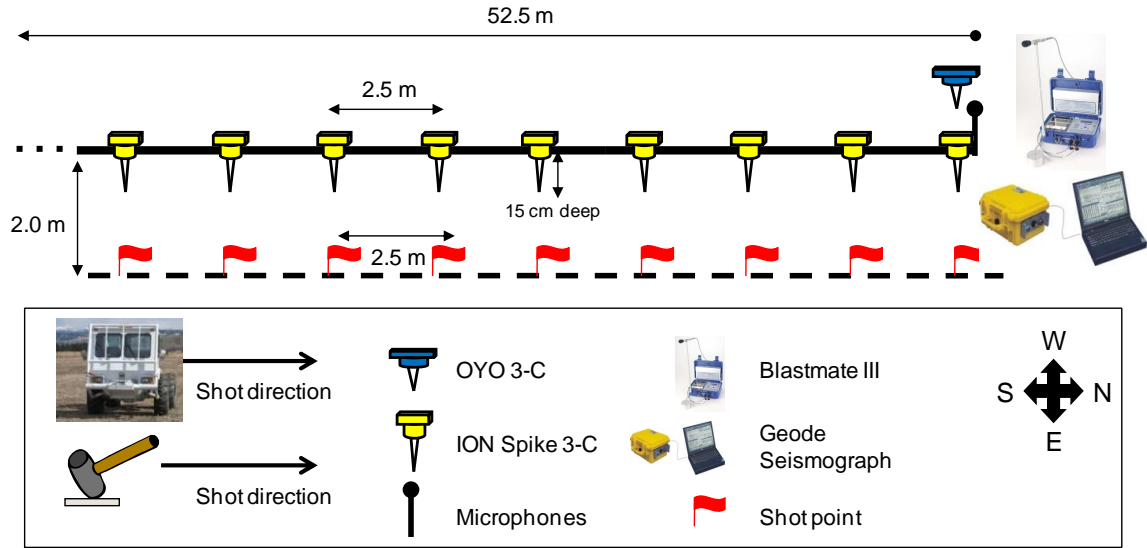


Figure 4.7. Acquisition layout for shot and receiver lines.

An IVI EnviroVibe (Figure 4.8 b) and a sledgehammer were used as seismic sources. Shot points were spaced every 2.5 m over a shot line parallel to the receiver line, nominally offset 2.0 m to the east. Each vibration point was centered and aligned to its corresponding receiver station. Following the vibe survey, the center of the vibrator's pad marks were used as the location for hammer shot points. The shooting direction for both sources was southwest-northeast with the first source point located at station 1, equivalent to a 52.5 m offset from the test station located at the northeast end. Each Geode was powered separately by a 12V battery and connected in series to a Panasonic Toughbook laptop through a special Ethernet cable. A total of 72 channels were available, 24 from each Geode, assigned as listed in Table 4.3. Color codes were used in the cables for connecting each geophone component and each microphone to a particular channel set (Figure 4.8 a). Station numbers, shot numbers and channel numbers for each Geode started at the southwest-end of the line. For example, channels 1, 25, 49, and shot 1 correspond to the geophone and source point at station 1, respectively; channels 2, 26, 50, and shot 2 correspond to the geophone and the source point at station 2, and so forth.



Figure 4.8. a) Geophone cable connections were facilitated by using color codes for each component. Each Geode recorded a full data set of a particular geophone component. b) The mini EnviroVibe, owned by the University of Calgary, was used as one of two seismic sources.

Table 4.3. GEODE channel assignment

Channel	Sensor component	Color code
1-20 and 22	Vertical / ION Spike 3-C	Red line
25-44 and 46	Radial / ION Spike 3-C	Green line
49-68 and 70	Transverse / ION Spike 3-C	Blue line
21	Vertical / OYO 3-C	Red line
45	Radial/ OYO 3-C	Green line
69	Transverse / OYO 3-C	Blue line
23	CREWES Microphone	Red line
47	APEX 435 Microphone	Green line
71	EMC 8000 Microphone	Blue line
24	Vibroseis sweep	Red line
48	OPEN	OPEN
72	OPEN	OPEN

The Vibroseis sweep was linear from 10-250 Hz over 10s with a 200 ms cosine taper. All sensors connected to the Geodes were sampled at 1ms. Listen time was set to 5 s due to a problem with time-zero. This problem could not be solved in the field and was attributable to either a trigger time delay in the cable connecting the VibePRO to the Geode trigger input, or to an unexpected time delay in the Geode response to the trigger signal. However, the sweep zero time was properly recorded at time-zero and cross-correlation of the pilot sweep with the raw data shows that the first breaks at the nearest offsets are very close to time-zero. Sledgehammer data was recorded without any problems over 1s at a sample rate of 1ms.

The Blastmate III is a self-triggered recorder. Recording starts only after an acoustic or seismic trigger level is reached. One can select a trigger source as either seismic, acoustic or both. To minimize the time difference between the Geode and Blastmate recordings, the seismic trigger was set to the minimum level available (i.e., 0.127 mm/s). Even this level imposed a limitation on far-offsets recordings for the seismic sources used in this field study. This was especially true for sledgehammer recordings as hammer-induced vibrations are very low for a source located even a few tens of metres away. In fact, a first conclusion can be stated: sledgehammer shots do not generate PPVs greater than 0.127 mm/s at offsets greater than 25 m for soils such as dry clay. Recording times were 1s for hammer shots and 11s for Vibroseis shots. A sample rate of 1024 samples per second was selected for Blastmate recordings because this rate was the closest to standard rates used in seismic exploration (1 ms, 2 ms or 4 ms). In addition to the far-offsets limitation, the standard Blastmate III has limited storage capacity (300 one-second events at 1024 samples per second) and relative long wait-time between shots. Such limitations made the acquisition operations highly dependent on the Blastmate timing and reduced the number of monitored shots to less than 35. Increasing the sample rate would have increased the accuracy of the waveform recordings but reduced the storage capacity. Future experiments involving Blastmate recordings would require careful planning with regard to number of shots versus waveform accuracy, unless an extended memory is available.

Aliasing occurs when a high-frequency signal appears as an erroneous low frequency because the waveform was sampled at too low of a sampling rate. An anti-aliasing filter solves this problem by removing the high-frequencies before they can appear at lower

frequencies. The BlastMate III standard sensors have anti-alias filters built into them to avoid this problem (InstanTel, 2001).

4.5. Vibroseis data

4.5.1. 3-C geophones

The natural domain for a direct sensor comparison is the receiver domain. Receiver gathers for each conventional geophone and each of its ground velocity components are shown in Figure 4.9. The data were cross-correlated with the vibrator sweep and windowed to 400 ms to assist in the identification of seismic events. A 250-ms AGC was applied before windowing the data for display purposes only. None of the amplitude analysis was performed using amplitude-corrected data. A valid reason for limiting our data in time was the presence of strong harmonic distortion after 500 ms, caused primarily by the non-linear coupling of the vibrator to the ground (which produces higher harmonics) and the proximity of the shot points to the geophones. In addition, we were not attempting to record deep reflections. Seismic data recorded with the Oyo 3C have stronger air blast contamination than seismic data recorded with the ION Spike. As expected, the ION Spike data were less affected by the propagating sound wave in the surface because the ION Spike was mostly buried and its geophone elements were located at the bottom of its case. On the other hand, the Oyo 3C case was exposed and prone to a direct impact of surface ambient noise. Ambient temperature during acquisition was about 20° C and the sky was partly cloudy. At these conditions, the speed of sound in air is close to 343 m/s. Note that the air blast looks stronger at the far offsets (first shots) because the first breaks at the near offsets are strong enough to overwhelm the acoustic wave arrivals. However, if a high-pass

filter is applied to these data, then the air blast becomes the predominant event across the receiver gather.

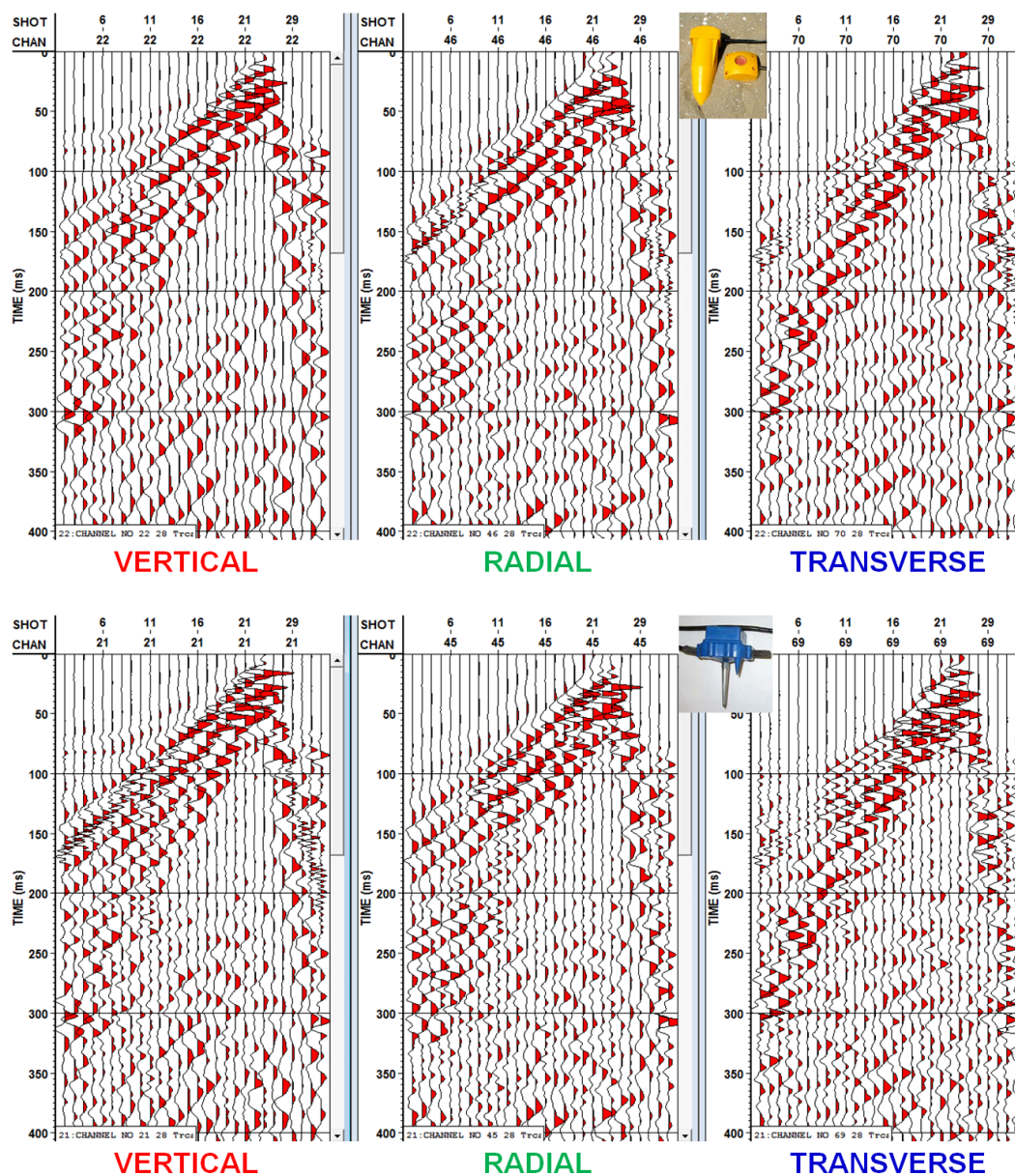


Figure 4.9. Vibroseis data separated by component and sorted into receiver gathers. The top data set is a receiver gather recorded from the ION Spike geophone. The bottom data set is a receiver gather recorded from the OYO geophone at the test station. A 200-ms AGC was applied for display.

A total of 22 Vibroseis shots were simultaneously recorded with the Blastmate and Geode Seismographs. Amplitude analysis was performed on uncorrelated traces only because we were unable to compute cross-correlations of the Blastmate data with the Vibroseis sweep correctly. Therefore, the “correlated” Blastmate data were not suitable for comparative analysis. Table 4.4 lists the Blastmate PPV, POP and peak displacement measurements per shot. Although they are closely related, peak displacement does not necessarily occur at the PPV of the event (Instanetel, 2001). Table 4.4 also includes the nominal offset and velocity component that triggered the Blastmate recording. Note that the Blastmate measurements show amplitude decay with increasing distance. For example, PPV values measured in the transverse direction decayed from 36.7 mm/s to 0.206 mm/s in a range of 52.5 m. Similarly, PPV in the vertical direction decayed from 10.8 mm/s to 0.222 mm/s and PPV in the radial direction from 18.2 mm/s to 0.302 mm/s. According to these measurements, a second conclusion can be stated: vibrations generated by the IVI EnviroVibe at offsets less than 52.5m are greater than 0.127 mm/s for soils such as dry clay.

Equation (4.1) was applied to each component of ground velocity as recorded from conventional geophones (i.e., each receiver gather) to determine the relative particle velocity amplitudes in physical units. Then, the PPV was found for each trace and compared to the Blastmate PPV measurements. A single difference factor was obtained per trace by dividing each Blastmate PPV measurement by the trace PPV. Table 4.5 contains factors of amplitude difference relative to the Blastmate geophone for Vibroseis shots.

Table 4.4. Blastmate data from Vibroseis shots.

Nominal Offset (m)	Trigger	Tran Peak (mm/s)	Vert Peak (mm/s)	Long Peak (mm/s)	Mic Peak (pa./dB)	Tran Disp. (mm)	Vert Disp. (mm)	Long Disp. (mm)
52.5	Long	0.206	0.222	0.302	1.00L	0.00088	0.00086	0.00128
50	Long	0.254	0.206	0.365	1.25L	0.00102	0.00099	0.0014
47.5	Long	0.286	0.222	0.286	1.25L	0.00103	0.0009	0.00102
45	Vert	0.317	0.19	0.413	1.00L	0.00093	0.00095	0.00121
42.5	Long	0.46	0.238	0.476	1.25L	0.00178	0.00094	0.0015
40	Long	0.651	0.27	0.397	1.75L	0.00274	0.00131	0.00168
37.5	Long	0.413	0.302	0.429	1.50L	0.00165	0.00115	0.00174
35	Vert	0.476	0.27	0.54	1.50L	0.00184	0.00115	0.00223
32.5	Long	0.571	0.381	0.556	1.25L	0.00243	0.00174	0.0021
30	Long	0.746	0.746	1	1.25L	0.00253	0.00285	0.00391
27.5	Long	0.762	0.778	1.32	1.75L	0.00228	0.00315	0.00522
25	Long	1	0.762	1.67	2.25L	0.00327	0.0029	0.00774
22.5	Tran	0.127	0.143	0.143	1.00L	0.00047	0.00104	0.00101
20	Vert	1.56	1.17	2.27	2.00L	0.00488	0.00385	0.00939
17.5	Vert	2.11	1.52	3.29	1.75L	0.00675	0.00671	0.0122
15	Long	1.17	1.68	2.87	3.00L	0.00407	0.00664	0.00957
12.5	Vert	2.37	2.38	4.05	4.00L	0.00588	0.00819	0.0123
10	Long	2.22	3.94	4.29	3.75L	0.00705	0.0127	0.0149
7.5	Long	2.41	4.24	4.46	6.50L	0.00819	0.0112	0.0182
5	Long	6.02	5.64	11.8	6.50L	0.0193	0.0147	0.0393
2.5	Tran	16.3	10.7	15.8	7.50L	0.0528	0.025	0.05
0	Tran	36.7	10.8	18.2	16.0L	0.103	0.0288	0.479

Table 4.5. PPV scaling factors for multicomponent seismic data relative to Blastmate data for Vibroseis shots.

Sensor component	Nearest shot	Farthest shot	Max. in receiver gather	Min. in receiver gather	Mean	Standard deviation
Vertical / ION Spike 3C	6.42	2.82	6.42	2.57	3.18	1.06
Radial / ION Spike 3C	10.61	2.85	10.61	2.57	3.63	2.27
Transverse / ION Spike 3C	19.87	3.05	19.87	2.74	4.18	3.81
Vertical / OYO 3C	5.78	2.84	6.15	2.28	2.98	0.99
Radial/ OYO 3C	10.32	2.95	10.32	2.43	3.57	2.16
Transverse / OYO 3C	18.43	2.53	18.43	2.17	3.63	3.56

These values represent a measure of the difference in amplitude between a conventional and a calibrated geophone, assuming that the PPV in both geophones occurs at the same event. The nearest-shot column in Table 4.5 contains amplitude difference factors for a shot point located 2.0 m nominal offset and 90-degree azimuth (in the cross-line direction). For this shot, the difference in amplitude of the transverse geophone relative to the Blastmate geophones was very large (19.87 for the ION spike and 18.43 for the Oyo 3C) because the vibration levels were so high (36.7 mm/s) that the conventional geophone amplitudes clipped. The other two components were also clipped as result of high vibration levels. As we will see later in the analysis of hammer data, for relative low PPV levels, these factors oscillate between 4 and 6. The ION spike PPV in the vertical direction was only 2.82 times smaller than the reference PPV for a 52.5 m source offset. Scaling factor mean values for each component were computed using PPV values from all monitored Vibroseis shots. Standard deviation values suggested that the dispersion of the factors from the mean is large because the amplitudes in the conventional geophones were clipped. Values between the ION spike and Oyo 3C differ a little due to their different sensitivities.

Average amplitude spectra were obtained for each uncorrelated receiver gather, including the Blastmate data. An average spectrum was obtained by averaging the 1D Fourier transform amplitude spectra computed for each trace in the receiver gather. Figure 4.10 shows average amplitude spectra for each component of particle velocity with the amplitude scale given in dB (referenced to the maximum amplitude on each spectrum). Note that the frequency responses of both conventional geophones are very similar to the frequency response of the calibrated geophone from about 15 Hz up to 80 Hz. As expected,

the frequency response of conventional geophones at frequencies below resonance (i.e., 10 Hz) was not optimal (-40 dB).

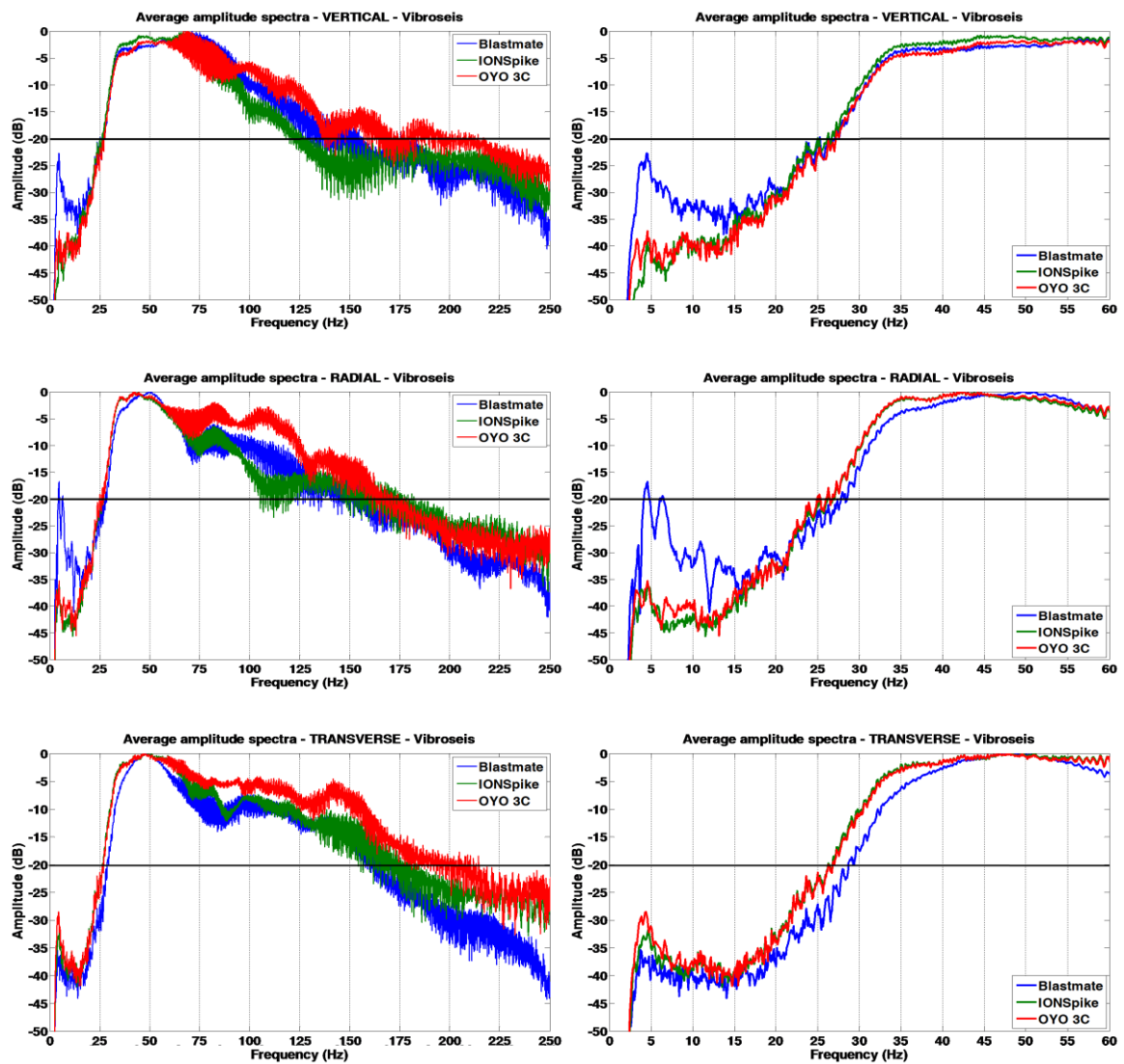


Figure 4.10. Amplitude spectra average of geophone data. A 2/5-250/255 Hz band-pass filter was applied to these data.

4.5.2. Microphones

Figure 4.11 shows average amplitude spectra for each uncorrelated microphone output. A 5-260 Hz band-pass filter was applied to the data before the computations to reduce any low-frequency bias. Recall that the frequency response for most microphones is fairly good from 20 Hz-20 kHz (i.e., humans' audible band), but we are interested in their performance at frequencies down to 10 Hz and how they compare to the Blastmate calibrated microphone. Microphone responses are very similar from about 40 Hz to 260 Hz (filter cut-off frequency), especially at high frequencies, which correspond to times when the sound coming from the vibrator's baseplate is very loud. Note that all microphone responses (including the Blastmate microphone) start decaying at about 40 Hz. This looks more like a frequency notch in the CREWES and APEX 432 microphones. Power-line noise at 60 Hz introduced a spike in all microphone responses.

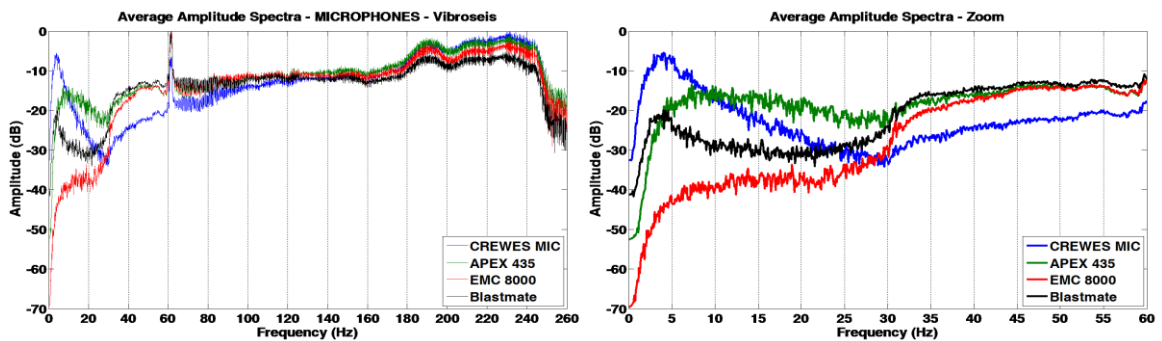


Figure 4.11. Amplitude spectra average of microphone data. A 5-260 Hz band-pass filter was applied to uncorrelated data. Note that all microphone responses (including the Blastmate microphone) have a response decrease at about 40 Hz.

The cross-correlation of a microphone signal with the pilot sweep results in a “pseudo-autocorrelation” of the microphone signal. In fact, the correlated microphone traces in either a shot or receiver gather are “pseudo-autocorrelations” with times of maximum amplitude given by the arrival times of the sound wave into the receivers. For instance, Figure 4.12 shows three receiver gathers for the uncalibrated microphones. Note that the highest amplitudes represent the amplitudes of maximum correlation due to the sound wave. Average amplitude spectra were also computed and plotted in Figure 4.12. The studio microphones have very similar responses across the entire frequency range except for frequencies less than 30 Hz. Unfortunately, this suggests that all microphones will respond very differently to the low frequencies where the ground roll is usually dominant. The poor and variable responses at low frequencies do not show any obvious coherent low-frequency events across the receiver gather.

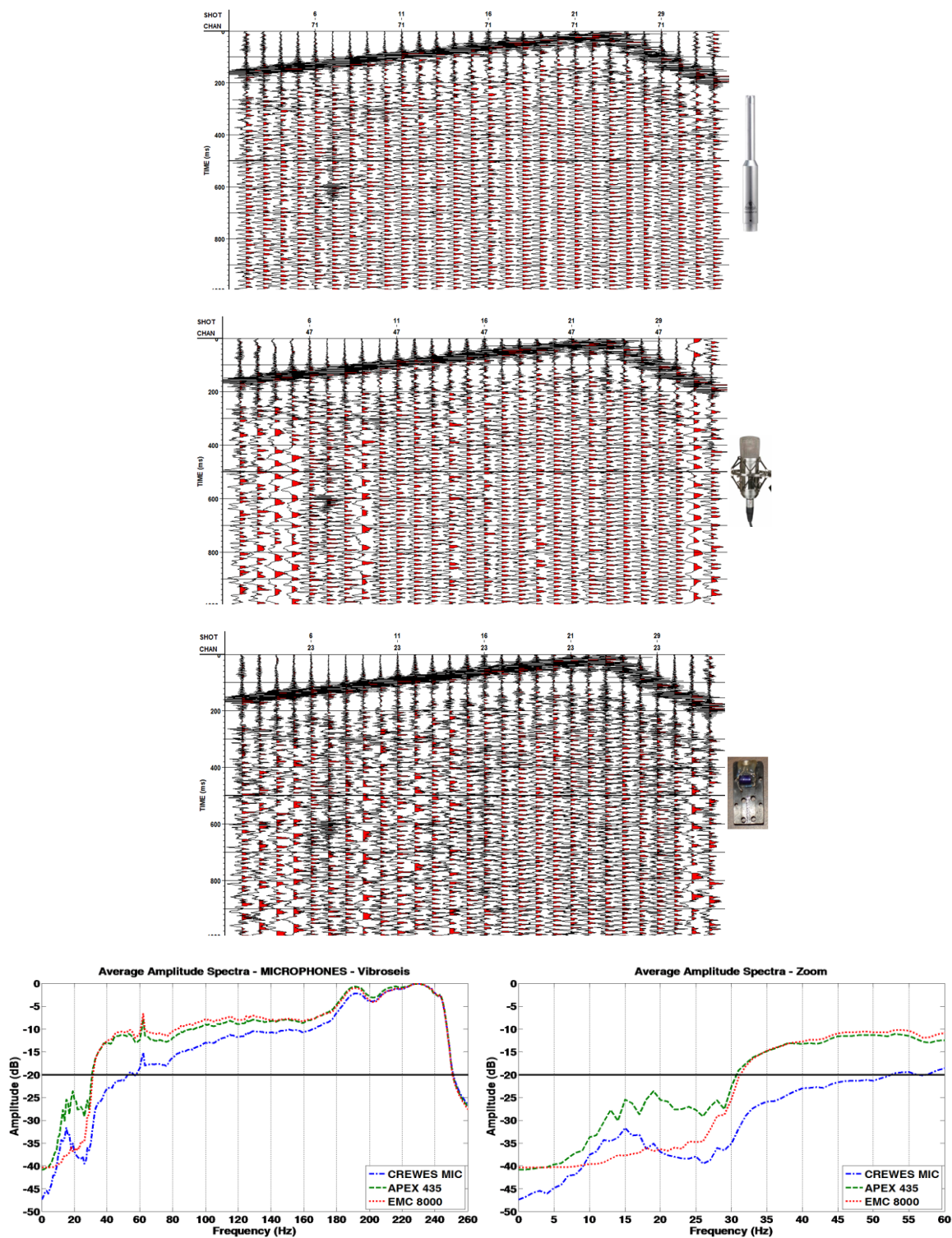


Figure 4.12. Pressure data recorded from APEX435 (top), CREWES prototype (centre) and EMC 8000 (bottom) microphones for all Vibroseis shots at 2.5m interval. VP's 23 to 32 were spaced every 10 m. Data were cross-correlated with the pilot sweep. AGC of 250 ms was applied to data for display only. The average of amplitude spectra is also show at the bottom. Note that all microphone responses are quite similar at high-frequencies, where the air blast is dominant.

4.6. Sledgehammer data

4.6.1. 3-C geophones

Similar to Vibroseis results, the OYO 3C geophone recorded noisier seismic data than the ION Spike when using the sledgehammer (see Figure 4.13). Only 11 out of 22 shots were simultaneously recorded with the Blastmate and the Geode Seismograph because particle velocity amplitudes of hammer shots beyond 25 m were very small. Such small amplitudes are well below the calibrated geophone resolution, which is the lowest measurable amplitude (i.e., 0.0159 mm/s). Table 4.6 lists the Blastmate PPV, POP and peak displacement measurements per hammer shot. Figure 4.14 shows the average amplitude spectra for each component of ground velocity for hammer shots. The average amplitude spectra of the conventional vertical components are very well matched to the Blastmate vertical geophone in the 12-90 Hz range (Figure 4.14, top). Average spectra for radial components (Figure 4.14, middle) are well matched from 10-80 Hz. Average spectra for transverse components (Figure 4.14, bottom) are well matched from 12-85 Hz. In general, the spectra for all components start to diverge from the Blastmate geophone at frequencies above 90 Hz. Note the strong low-frequency response of the calibrated geophone at frequencies down to 2 Hz. Factors of amplitude difference between conventional and calibrated geophone amplitudes were found following the same methodology used for Vibroseis data. Table 4.7 shows maximum, minimum and mean values of these factors for each receiver gather. Note that the longest offsets (25 m) correspond to trace 1 and the nearest offsets (2 m) correspond to trace 11 for all receiver gathers. According to these results, the particle velocity magnitude in the vertical direction as recorded by the ION Spike is 2.11 times smaller than the true magnitude as recorded by the Blastmate. The mean

value for the full receiver gather of vertical particle velocity is 2.97. In this case, standard deviation values suggested that the dispersion of the scaling factors from the mean in the entire receiver gather is small (0.62).

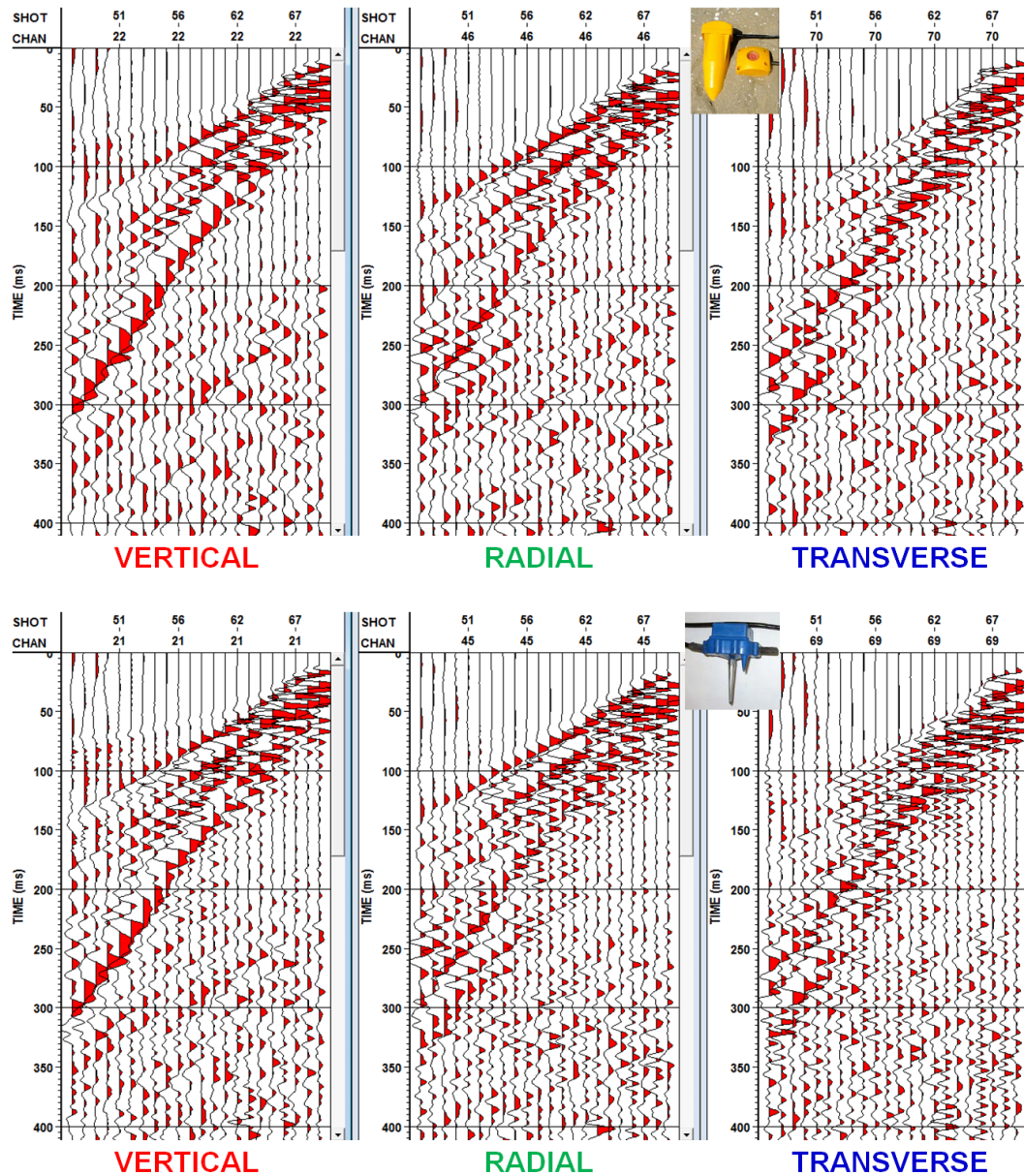


Figure 4.13. Hammer data separated by component and sorted in receiver gathers. The top data set is a receiver gather recorded from the ION Spike geophone. The bottom data set is a receiver gather recorded from the OYO geophone at the test station. A 200-ms AGC was applied for display.

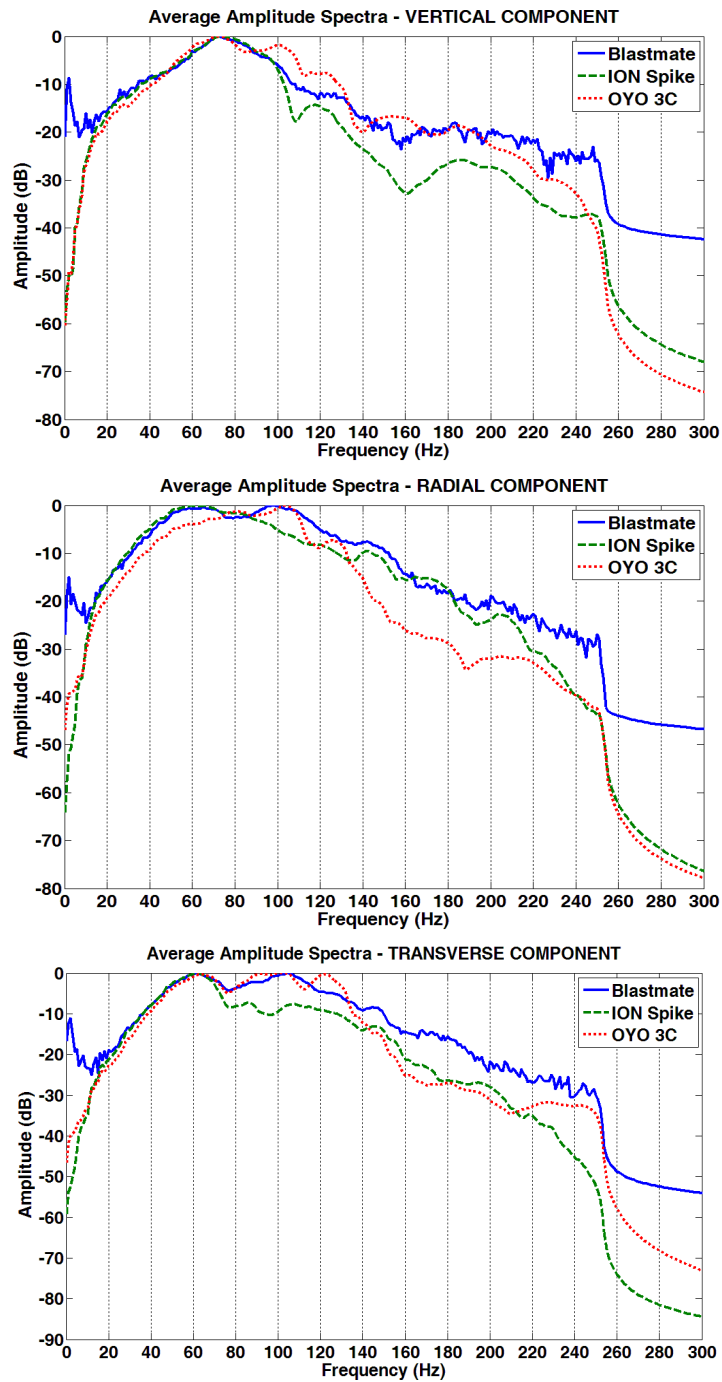


Figure 4.14. Average amplitude spectra for each component of ground velocity for hammer shots.

Table 4.6. Blastmate data from hammer shots.

Nominal Offset (m)	Trigger	Tran Peak (mm/s)	Vert Peak (mm/s)	Long Peak (mm/s)	Mic Peak (pa./dB)	Tran Disp. (mm)	Vert Disp. (mm)	Long Disp. (mm)
25	Long	0.0952	0.0635	0.127	0.500L	0.00022	0.00016	0.00034
22.5	Long	0.127	0.0794	0.127	0.500L	0.00031	0.00039	0.00039
20	Long	0.238	0.111	0.175	<0.500L	0.00052	0.0004	0.00051
17.5	Long	0.159	0.159	0.206	0.500L	0.00036	0.00053	0.00066
15	Long	0.27	0.206	0.302	<0.500L	0.00052	0.00079	0.00102
12.5	Long	0.238	0.238	0.381	0.500L	0.0005	0.00065	0.00106
10	Vert	0.524	0.492	0.746	0.500L	0.00076	0.00129	0.0017
7.5	Vert	0.365	0.841	0.667	0.750L	0.00079	0.00179	0.00148
5	Vert	1.51	1.43	2.95	1.00L	0.00274	0.00315	0.00554
2.5	Vert	2.81	1.59	4.41	2.00L	0.00608	0.00359	0.00962
0	Vert	7.38	2.27	4.24	2.50L	0.0126	0.00567	0.00651

Table 4.7. PPV scaling factors for multicomponent seismic data relative to Blastmate data for hammer shots.

Sensor component	Nearest shot	Farthest shot	Max. in receiver gather	Min. in receiver gather	Mean	Standard deviation
Vertical / ION Spike 3C	2.11	3.90	3.90	2.11	2.97	0.62
Radial / ION Spike 3C	3.89	2.84	3.89	2.43	3.05	0.51
Transverse / ION Spike 3C	6.04	3.01	6.04	2.87	3.62	0.95
Vertical / OYO 3C	2.05	2.27	2.56	1.42	1.98	0.37
Radial/ OYO 3C	2.95	2.68	3.43	1.51	2.45	0.54
Transverse / OYO 3-C	4.02	1.77	4.02	1.15	2.11	0.81

4.6.2. Microphones

A 2-250 Hz band-pass filter was initially applied to the data (top left and top right in Figure 4.15). Note that the frequency response of the EMC 8000 microphone is very close to the Blastmate calibrated microphone for the entire frequency band, as in the Vibroseis data. However, the average spectra of the CREWES prototype and the APEX 435 microphone are biased by very low frequencies (<15 Hz). By applying a second band-pass filter to attenuate frequencies less than 10 Hz, the average spectra are partially corrected (centre left and centre right in Figure 4.15). By applying a third filter to attenuate frequencies less than 15 Hz, the average spectra are corrected; therefore, they become

comparable to the Blastmate microphone response (bottom left and bottom right in Figure 4.15). This suggests that frequencies below 20 Hz are not reliable except for the Blastmate microphone and EMC 8000.

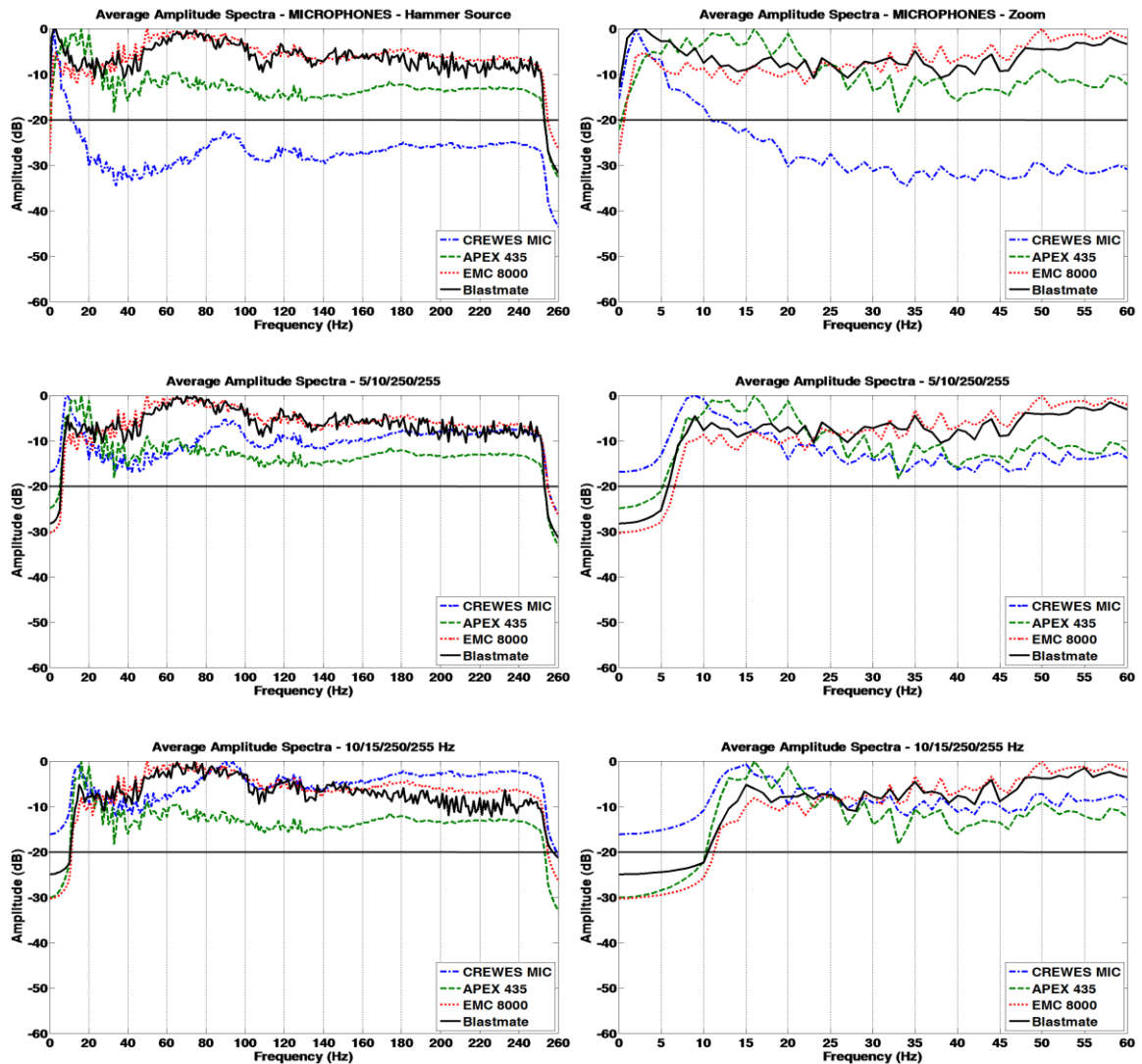


Figure 4.15. Average amplitude spectra of microphone data. 11 hammer shots were used for these computations. A band-pass filter (0-2-250-255 Hz) was initially applied to the data (top left and top right). Note that the frequency response of the EMC 8000 microphone (in red) is very close to the Blastmate calibrated microphone (in black) for the entire frequency band. By applying a second band-pass filter to attenuate frequencies less than 15 Hz, the average spectra of the CREWES prototype (dashed blue) and the APEX 435 microphone (green) were partially corrected (bottom left and bottom right).

4.7. Particle motion analysis

Particle motion analysis was also performed using hodograms. Hodograms are a useful technique for displaying particle motion of a vector wavefield and in elucidating wave types (Lawton and Bertram, 1990). Three components of ground motion and a time window are required to reconstruct the particle trajectory along the inline and cross-line planes. Hodogram analysis of the first breaks was performed for the ION spike, OYO 3C and Blastmate data using the CREWES Hodogram Explorer. The data were analyzed without any amplitude correction. A 2/5-250/255 Hz band-pass filter was applied to all data sets to minimize signal distortion at very low and very high frequencies. For a hammer source, particle motion trajectories at offsets less than 10 m were comparable to particle motions as recorded from the Blastmate geophone. Figure 4.16 depicts the geometry of the source-receiver azimuths for the near-offset shots. Note that the azimuth at nominal zero offset is 90° with respect to the inline direction (H1). With this source-receiver geometry, the angle of polarization in the transverse component (H2) of all geophones should decrease with increasing source offset. Figure 4.17 shows hodograms results for all the geophones at the test station (nominal zero offset).

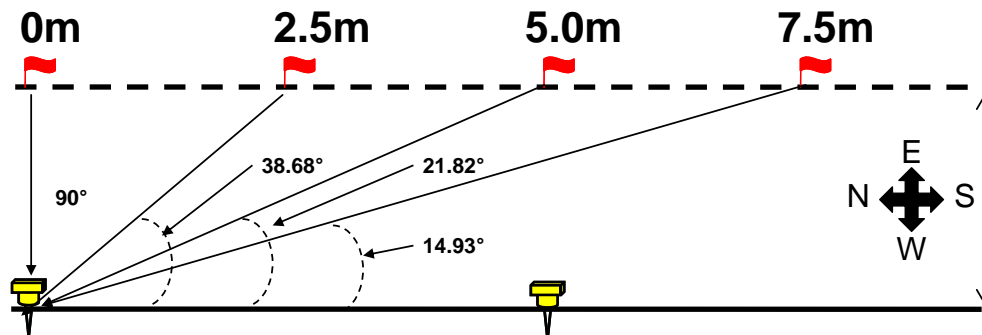


Figure 4.16. Geometry of source-receiver position for polarization analysis.

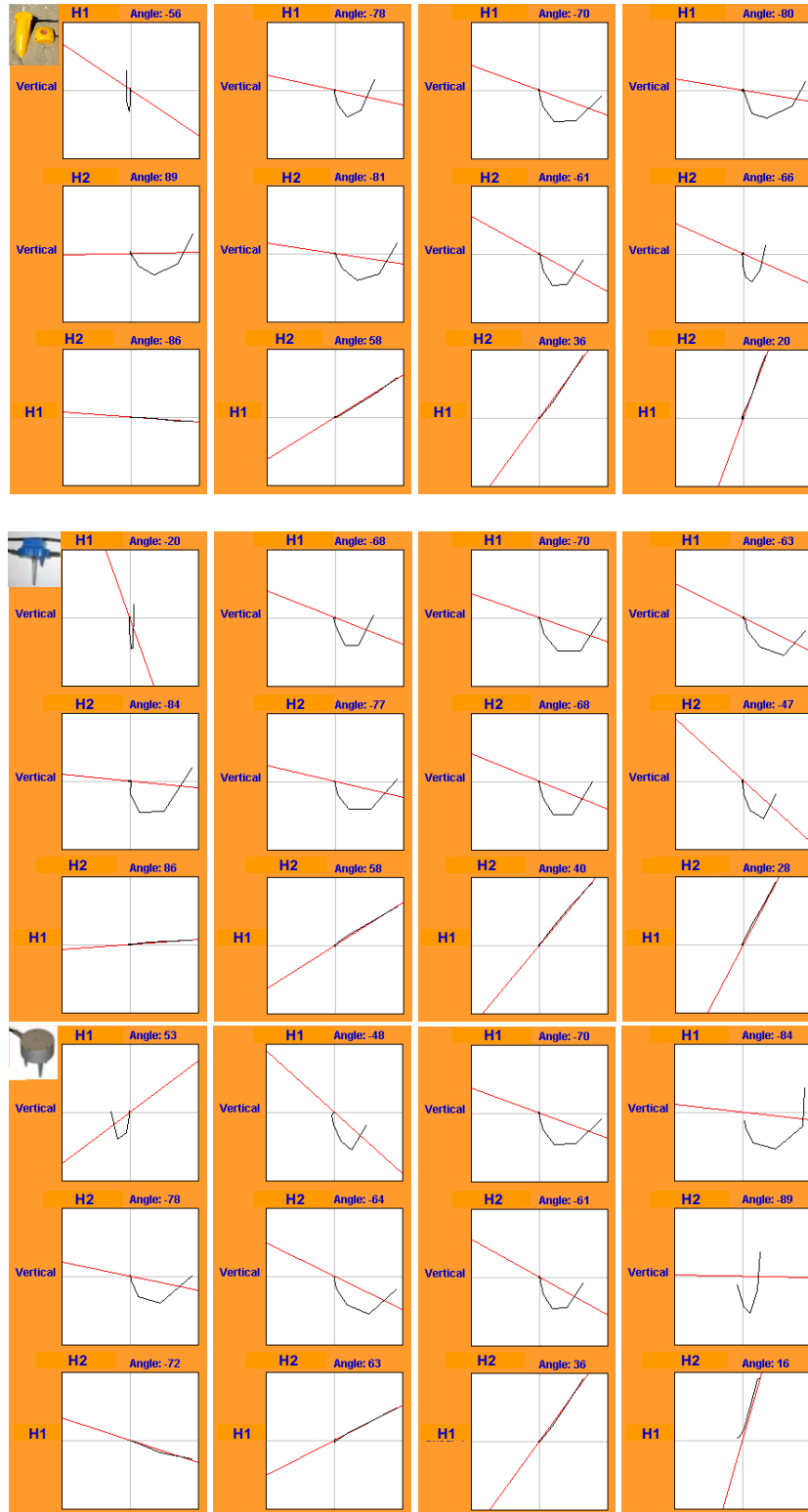


Figure 4.17. Analysis of particle motion computed from the first breaks (one half-cycle) of particle velocity data (hammer). H1 is the radial (inline) component and H2 is the transverse (cross-line) component. Vertical components are mapped into the vertical axis. From left to right, hodograms correspond to shot points at 0, 2.5, 5.0 and 7.5 m nominal offsets.

Note that the angles of polarization in the transverse direction (H1) decrease with increasing distance, and the motion in the inline (H1) direction becomes stronger. PPV values from Table 4.6 show that the PPV in the transverse component at zero nominal offset is 7.38 mm/s while the radial PPV is 4.24 mm/s. At 2.5 m, the transverse PPV is only 2.81 mm/s while the radial PPV increases a little from 4.24 to 4.41 mm/s. At 5 m, the PPV in the radial component is nearly twice the PPV in the transverse component. In all cases, the PPV in the vertical component is smaller than the PPV in the horizontal components.

CHAPTER FOUR: AIR PRESSURE MEASUREMENTS DURING SEISMIC DATA ACQUISITION

In this chapter, I describe two 3C-2D seismic surveys conducted in the Western Canada Sedimentary Basin (WCSB). Both surveys included air pressure measurements at some 3-C geophone locations in a regular interval along the seismic profile. Data from these surveys are used in Chapter 6 to evaluate a new method for air-noise attenuation in seismograms by combining air pressure and seismic measurements. Other authors have reported similar air pressure-seismic measurements with a few microphones positioned at two or three geophone locations but not during a seismic survey (e.g., Brook et al., 1989; Sallas and Brook, 1989; Albert, 1993).

5.1. 3C - 2D survey at Pikes Peak heavy oilfield, Saskatchewan, Canada

During March 2000, the CREWES project conducted a multicomponent 2D seismic survey at the Pikes Peak heavy oilfield located in Saskatchewan, Canada (Figure 5.1). The survey consisted of a 3.8 km seismic profile, Vibroseis sources and a combination of conventional vertical geophone arrays, microphone prototypes and single 3-C geophones. The Pikes Peak oilfield produces heavy oil from the sands of the Waseca Formation of the Lower Cretaceous Mannville Group, which lie at a depth of approximately 500 m (Hoffe et al., 2000). A particular problem with this survey was that related to high levels of noise in the seismic data from a diversity of sources. In an active oilfield, pumps, generators, traffic, production wells, injection wells, and flowing pipelines produce continuous ground vibrations. Noise from these sources and noise generated by the Vibroseis trucks resulted in very noisy seismic data. Therefore, this survey was a unique opportunity to evaluate the

potential of using air pressure recorded on microphones to attenuate some of the noise in geophone records.

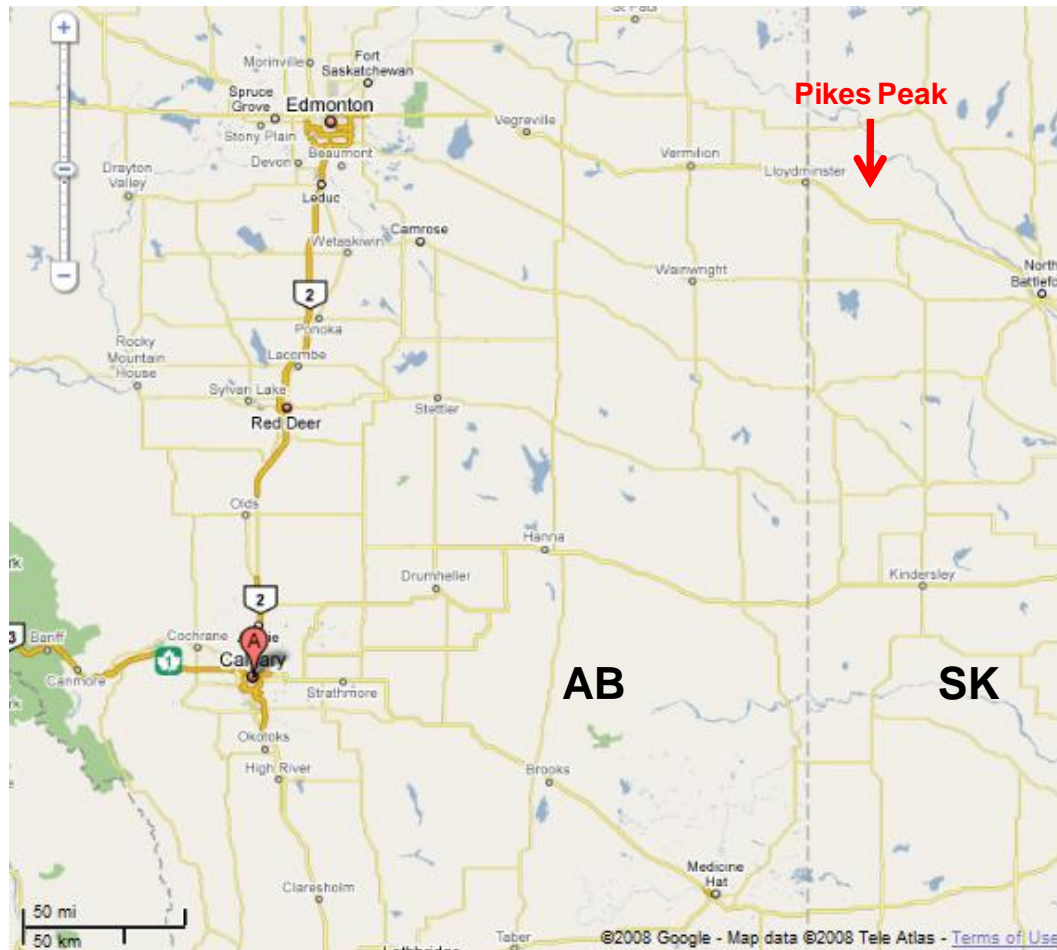


Figure 5.1. Location map of the Pikes Peak heavy oilfield, Saskatchewan.

5.1.1. Acquisition

The seismic line included 3-C geophones at 10 m spacing, vertical geophone arrays at 20 m group interval and microphones at 20 m spacing. The Litton LRS-1033 3-C geophones (10 Hz) were planted in holes of about 30 cm depth. The microphone prototypes were placed with the 3-C geophones every other augured hole. Vertical arrays consisting of 6 geophones were planted at surface level. This configuration resulted in half the number of traces in the microphone and vertical array shot gathers relative to the 3-C geophone shot

gathers. Two Vibroseis sources spaced over 10 m were used at 20 m spacing. The center of the Vibroseis array was aligned to the source station flag to ensure certain consistency on source-receiver offsets. The Vibroseis data were recorded using the ARAM Aries system (24 bits) in a split-spread configuration, with maximum offsets of ± 1330 m and a maximum of 1064 live channels per source point. To facilitate field logistics, the three components of the Litton geophones were recorded separately as three distinct receiver lines. The vertical arrays and microphones were assigned to a fourth receiver line (Figure 5.2). Only Vibroseis uncorrelated and non-summed data were recorded in the field. A summary of the recording parameters is included in Table 5.1.

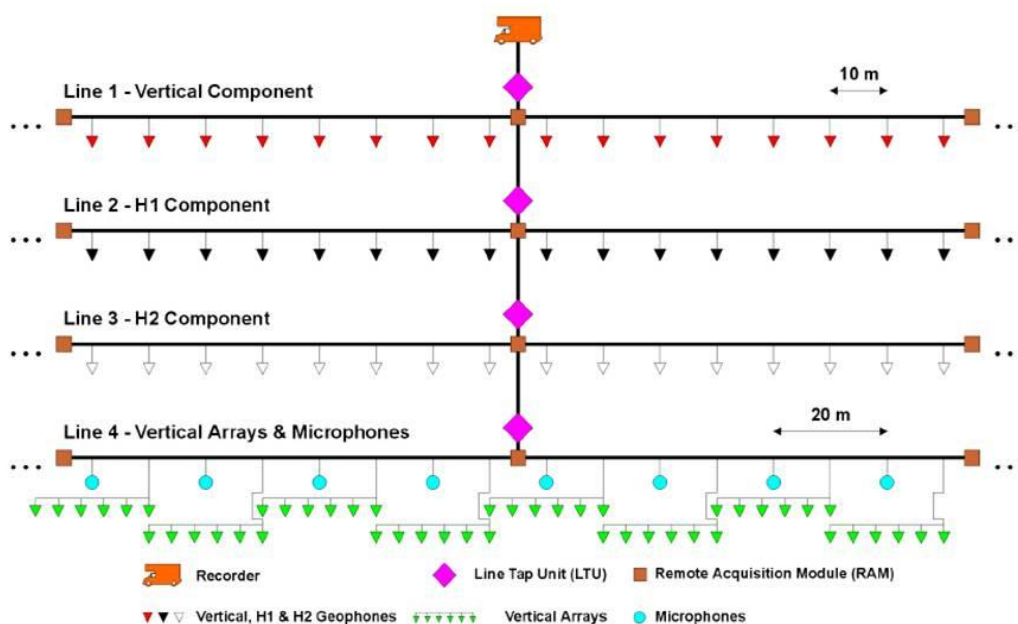


Figure 5.2. Acquisition layout for the Pikes Peak multicomponent survey (from Hoffe et al., 2000).

Table 5.1. Pikes Peak survey acquisition parameters

Contractor	Veritas DGC
Recording system	ARAM Aries 24 bits
Source	2 HEMI-44 vibrators 25,000 kg each
Sweeps	4 sweeps, 8-150 Hz, 2 segments, 16 seconds length 1) 0.325 s, 8 - 25 Hz 2) 15.625 s, 25 – 150 Hz
Listening	4 seconds
Sampling rate	2 ms
Total recording	20 seconds
Vibrator spatial area	10 m
Source interval	20 m
Preamp gain	36 dB
Low-cut filter	3 Hz
High-cut filter	164 HZ
Receiver interval 3-C	10 m
Receiver interval geophone	20 m
Receiver interval microphones	20 m

5.1.2. Data pre-processing and analysis

Data analysis required the decimation of the vertical component seismic data to match the spacing of microphone data. That was the case for the experiments discussed in this chapter, since they were also designed for other purposes. Although microphone data interpolation was a viable option, I decided to keep it as simple as possible and analyze “true” data on a trace-by-trace basis.

The analysis approach was to address uncorrelated microphone data first, both in time and frequency domains. A first observation was that the Vibroseis-generated air wave is fundamentally a sweep-like signal whose frequency content depends on the vibrator sweep parameters. This observation was made after transforming the uncorrelated output of the microphone and the Vibroseis sweep into the time-frequency domain. In this case, I used the Gabor transform to perform such time-frequency analysis. The Gabor spectrum in

Figure 5.3 corresponds to a two-segment Vibroseis sweep (linear from 8 Hz to 25 Hz and nonlinear from 25-250 Hz) used in the Pikes Peak experiment. In these time-frequency plots, the red color represents higher amplitudes whereas the blue color represents lower amplitudes. Figure 5.4 shows the Gabor spectrum of a raw microphone output recorded at nominal zero offset. Note that in the microphone Gabor spectrum the highest amplitudes occurred at the highest frequencies and latest times. This was particularly expected because the sound coming from the Vibroseis was louder at later times. If you stood a few metres from the Vibroseis truck, you would likely experience an increase in loudness as the sweep frequencies increase (for an up-sweep). Also note the presence of higher harmonics in the signal, which suggested the proximity of the seismic source to the microphone. Harmonics must be avoided in seismic data acquisition because they introduce strong correlation artifacts in correlated seismic records. I show some examples of this kind of artifacts in section 5.2. An analysis of the uncorrelated microphone traces as a function of distance from the source was also performed in the Gabor domain. It revealed that the air wave amplitude decayed with distance in agreement with the observations in Chapter 4 and observations by others (Brook et al., 1989; Sallas and Brook, 1989). Since the microphone prototypes do not represent the actual air pressure of a sound wave, this analysis was based on a qualitative observation of the waveforms as a function of distance in the time and Gabor domains (see Figure 5.5). Note that the near-offset microphone traces exhibit the beaming effects described in Chapter 2. This effect disappears with increasing distance from the source. Figure 5.6 shows another example of sound beaming as recorded by a microphone at 40 m offset.

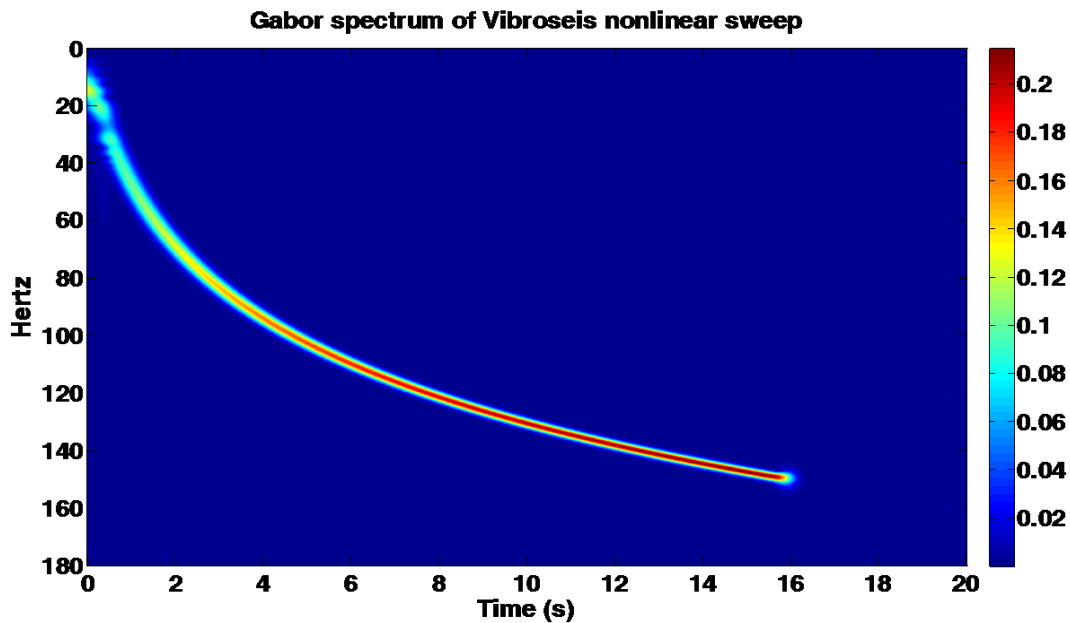


Figure 5.3. Time-frequency decomposition of the Vibroseis sweep used in the Pikes Peak survey. The 16s sweep was linear from 8-25 Hz and nonlinear from 25-150 Hz.

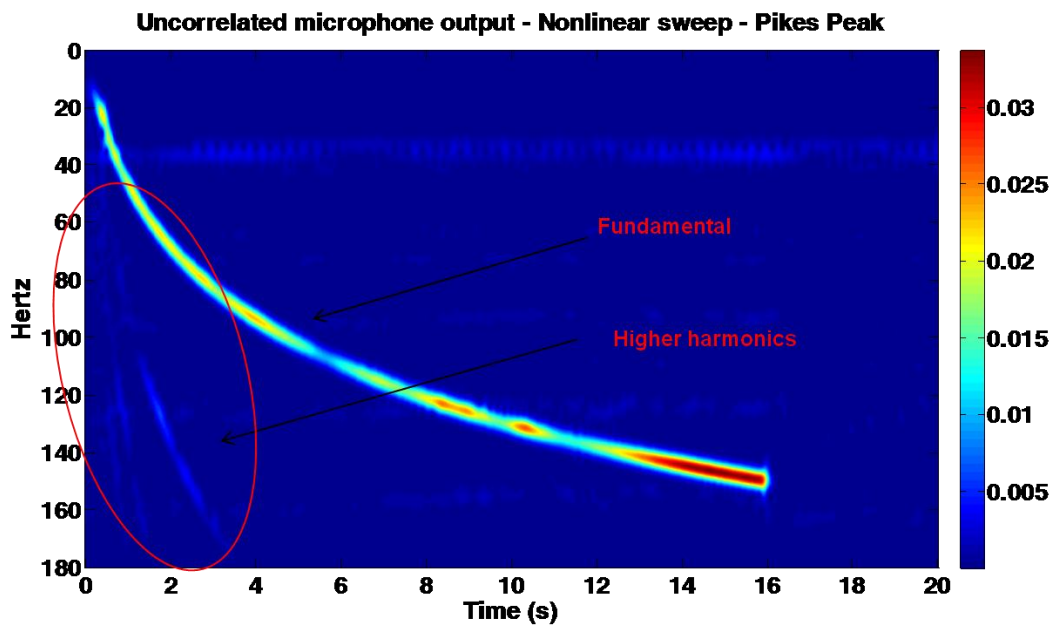


Figure 5.4. Uncorrelated microphone output recorded at nominal zero offset from the Vibroseis array and represented in the time-frequency domain.

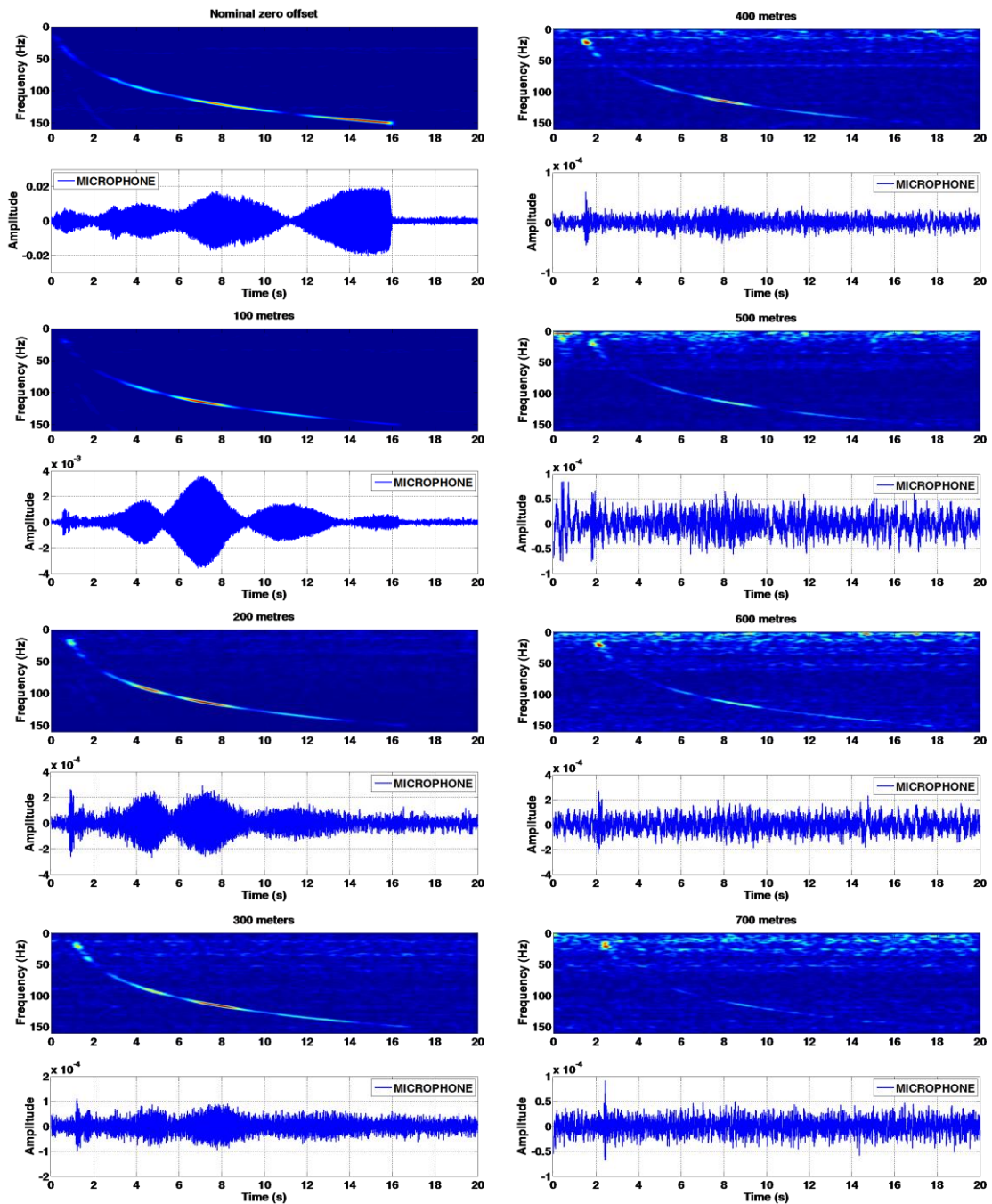


Figure 5.5. Analysis of air-pressure amplitude as a function of distance for several microphones. Note how the high-frequency components of the air wave decay with distance while the low-frequency components remain strong. Also note that the lobes of radiated sound disappear with distance.

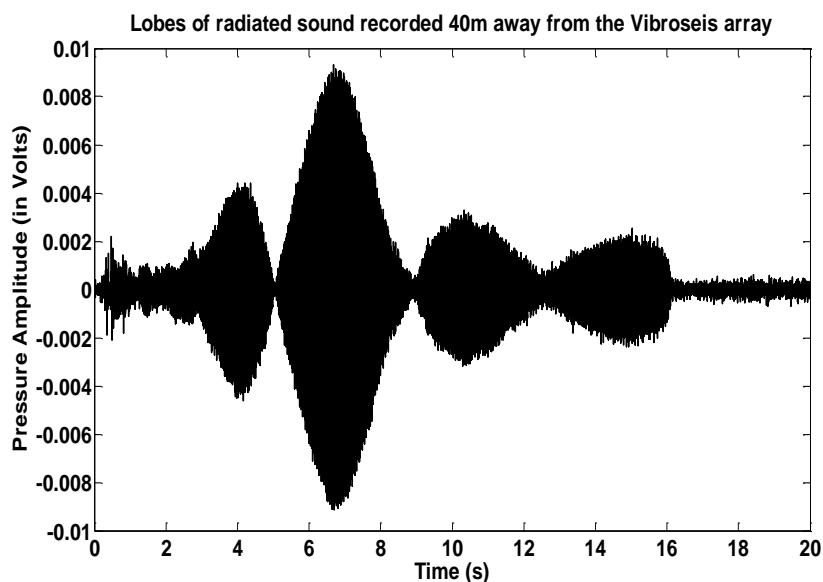


Figure 5.6 Vibroseis-uncorrelated microphone output recorded at 40 m nominal offset from the Vibroseis array. The first nodal point (or lobe) occurred at about 5 s when the sweep frequency was about 110 Hz. The second nodal point occurred at about 9 s when the sweep frequency was close to 130 Hz.

The second step in this analysis was to correlate the raw microphone and geophone data against the Vibroseis sweep as it is normally done for Vibroseis field data. Recall that the long-time duration of the sweep produces returning reflections from various depths that overlap one another in time. Cross-correlation is required to transform these long-duration signals into impulse-like signals. In theory, the cross-correlation of the recorded geophone signal with a reference version of the transmitted sweep compresses the extended reflections and also improves the S/N ratio (Hoover et al., 1984). This suggests that the cross-correlation process attenuates events in the data whose frequency content is outside the sweep band. Therefore, after correlating air pressure and seismic data with the sweep, we would expect the attenuation of background and harmonic noise in the field records. In practice, however, there is a little noise and artifacts remaining in the data. The cross-correlation of the microphone signal with the pilot sweep results in a “pseudo-autocorrelation” of the microphone signal. This is similar to the autocorrelation of the

Vibroiseis sweep, which results in a particular wavelet known as Klauder wavelet. In this case, the long-duration air wave is compressed to the impulse-like signal that would be obtained from an impulse source such as dynamite or sledgehammer. For an ensemble of consecutive microphone traces, the times of maximum correlation are determined by the linear moveout (LMO) associated to the air wave arrival in the microphones (see Figure 5.7)

Figure 5.7 shows examples of common shot gathers for microphone and geophone data. The panel on the left contains microphone data with 500-ms AGC for display purposes. Note that the stronger energy is the source-generated airwave travelling at the speed of sound in the air (331.5 m/s at 0° C). The common shot gather on the right panel contains the vertical component of ground velocity decimated from the 3-C geophones. The number of traces in the geophone shot gather is twice the number of traces in the microphone shot gather because the 3-C geophone spacing was 10 m. Note that the airwave coupled into the geophones and appears as a coherent event across the shot gather. It travelled at the speed of sound in the air.

Visual inspection of geophone and microphone shot gathers suggested that pump jack noise is mainly vibrational and coupled into the 3-C geophones through ground motion. Little of this noise energy appears to be recorded from the microphone prototypes.

The third step of the analysis was to investigate the low-frequency energy recorded by the microphones. As stated in Chapter 1, it would be very helpful to have a noise reference for surface waves (ground-roll), air waves and background noise from an independent sensor, and then use this reference for noise attenuation in geophone records. So far, I have shown that strong broad-band air waves can be recorded with microphones.

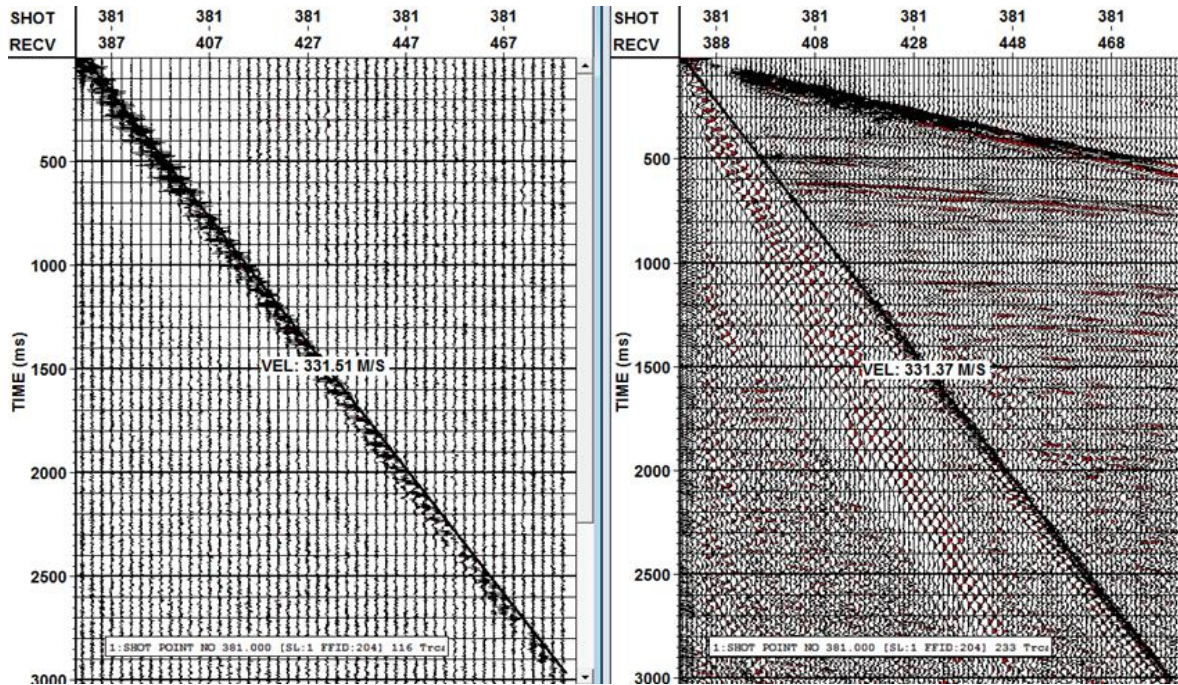


Figure 5.7 Example of correlated microphone (left) and geophone data (right) from Pikes Peak. Note that the airwave in these shot records propagates at the speed of sound in the air (331 m/s).

To investigate the response of the microphone prototypes at low frequencies, a 12-25 Hz band-pass filter was applied to uncorrelated microphone traces in a shot gather, because this is the frequency band where the ground-roll is usually dominant. An analysis time window from 0-1000 ms and offsets range of ± 240 m was defined to compute the average amplitude spectrum (Figure 5.8-5.9). The amplitude spectrum shows strong low-frequency energy from 10-40 Hz with peak at about 20 Hz that corresponds to the low-frequency air wave radiated from the Vibroseis. This interpretation was supported by a subsequent analysis of the correlated microphone and geophone traces (see Figure 5.10). A geophone shot gather is shown on the left panel of Figure 5.10, which contains a cone of surface waves and air waves overwhelming primary reflections. Unlike geophone data, such a noise cone constitutes the signal of interest in microphone data. However, the microphone shot gather on the right panel of Figure 5.10 shows a coherent air wave cone only. There is

not obvious surface wave energy as in the geophone case, which suggests that the air pressure energy, if any, generated by the passage of the surface waves by the microphones is very small. Frequency-wavenumber (f-k) spectra for geophone and microphone data are shown in Figure 5.11. Note that both spectra are very different. First breaks, surface waves, and reflections characterize the geophone f-k spectrum while only the airwave characterizes the microphone f-k spectrum.

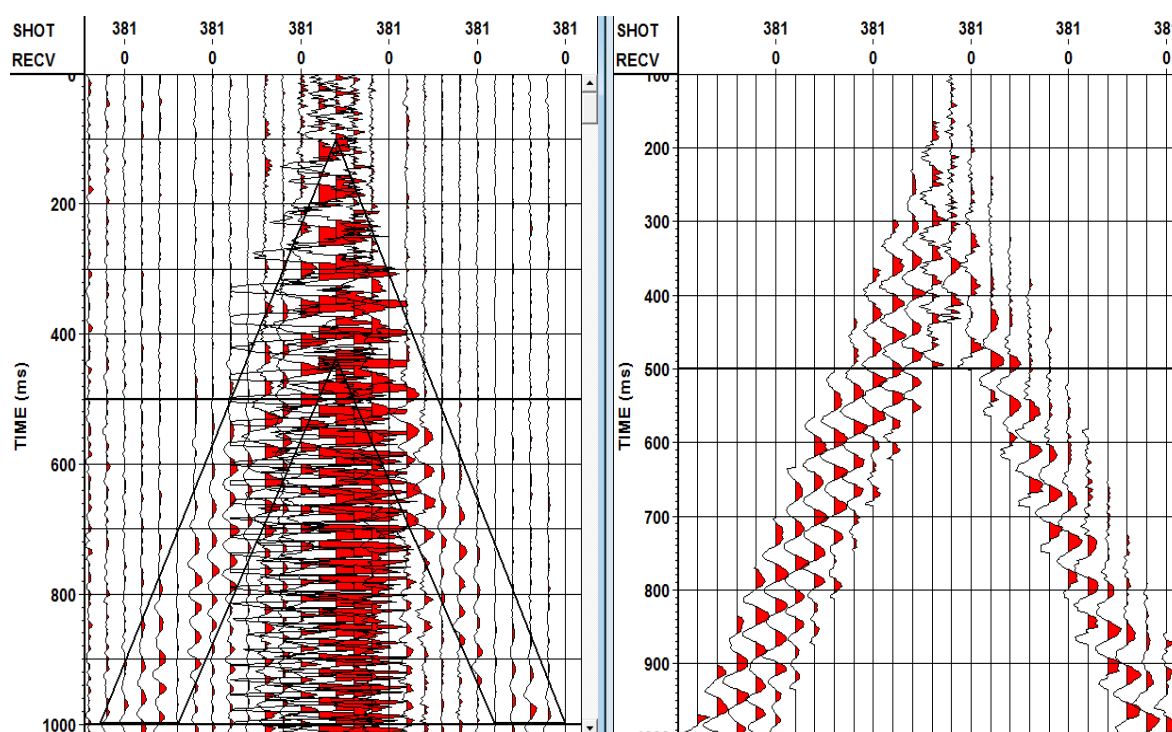


Figure 5.8. First 1000 ms of uncorrelated microphone data. Raw data and time analysis window (not gained) are shown of the left. Windowed data with AGC is shown of the right

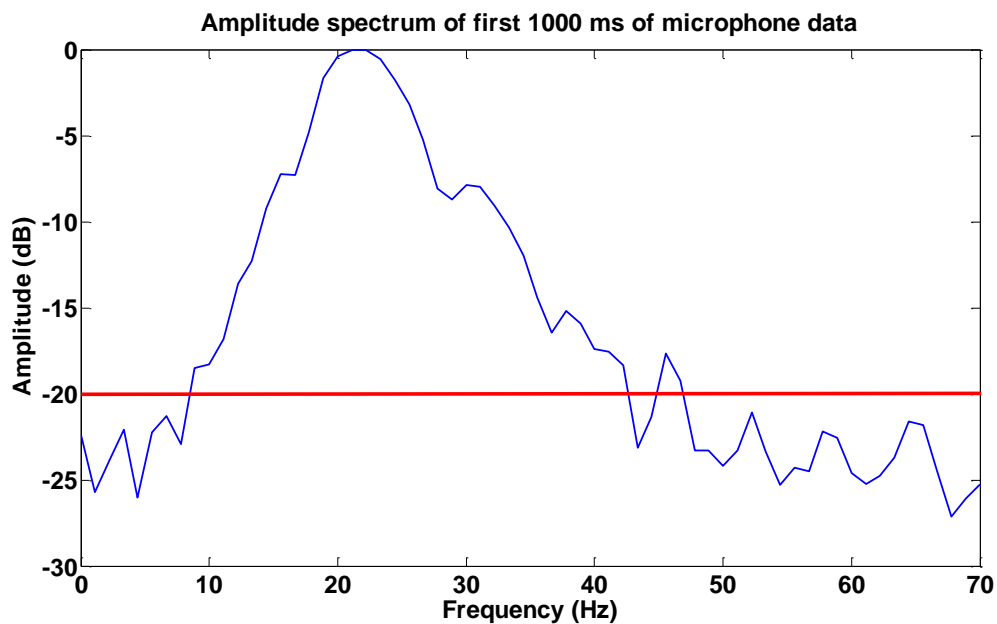


Figure 5.9 Amplitude spectrum of the first 1000 ms of uncorrelated microphone data over the analysis window shown in Figure 5.6 with no amplitude scaling. This wave train in the uncorrelated microphone data corresponds to the low-frequency component of the Vibroseis-generated sound wave with peak amplitude between 20-23 Hz.

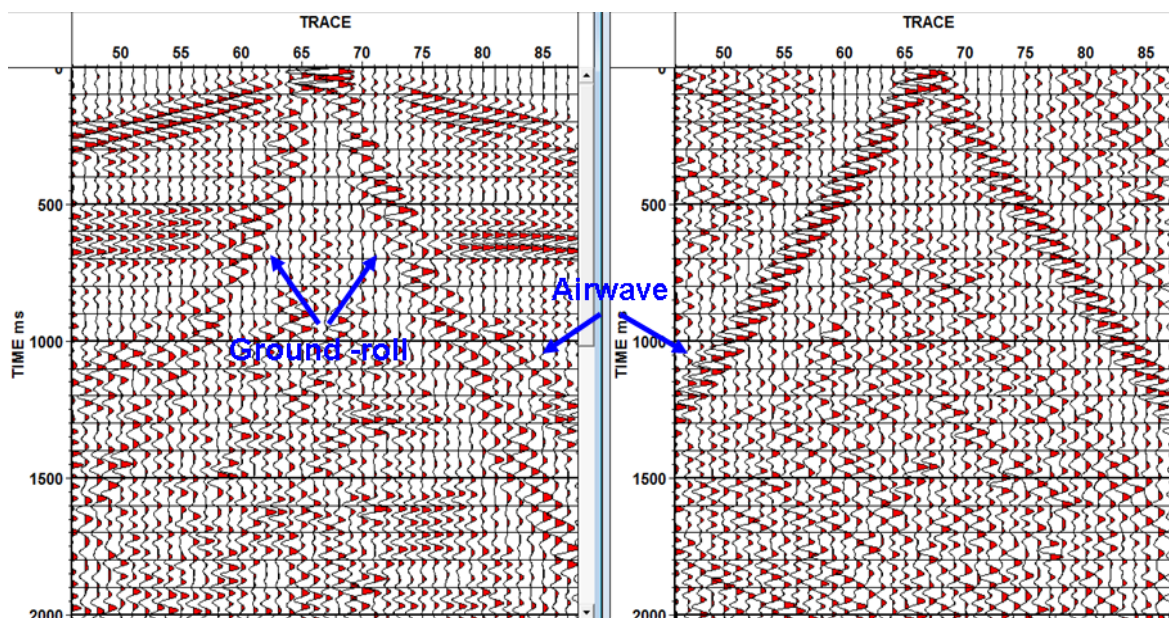


Figure 5.10 Vibroseis correlated vertical geophone (left) and microphone data (right). A 10/12/25/30 Hz band-pass filter was applied to these data to investigate the low-frequency energy in the typical ground-roll frequency band. A 500-ms AGC has been applied.

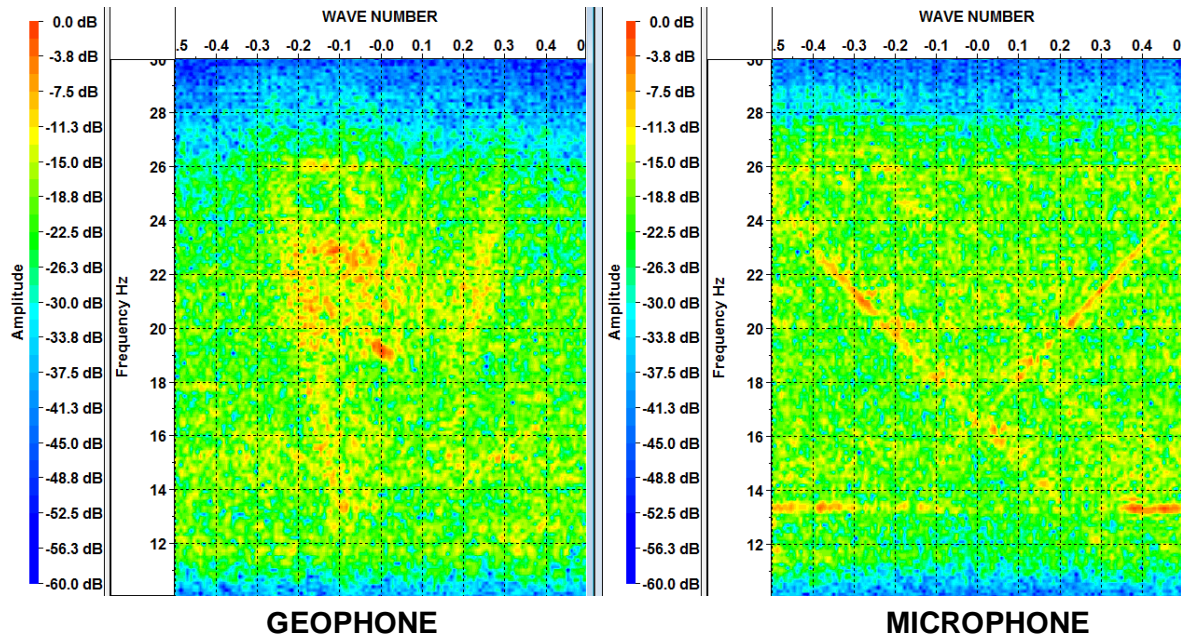


Figure 5.11. F-k spectra of vertical component of ground velocity (right) and air pressure (left). A 10/12/25/30 Hz band-pass filter was applied to both shot gathers to investigate the low-frequency energy contained in these records. Note that the microphone information in the surface wave's bandwidth is the low-frequency component of the air wave.

5.2. 3C - 2D high-resolution near-surface survey at the Rothney Astrophysical Observatory, Alberta, Canada

The 3C-2D high-resolution near-surface survey was undertaken at the Rothney Astrophysical Observatory near Priddis, Alberta during the winter of 2008. The site is a rural area about 26 km southwest of downtown Calgary (Figure 5.12). One of the aims of the experiment was to acquire a unique data set to test a 3C land streamer and compare its shot records and processing results to those of a 200 m multicomponent seismic profile at 1 m spacing. We also deployed 32 of our microphones at 5 m spacing to span 155 m of the multicomponent line. In this chapter, however, only conventional 3C and microphone data are considered. Since the 3-C geophones were mostly buried at 1m spacing, this experiment allowed us to study the transfer of acoustic energy into the ground. The site was relatively

flat, sloping generally downwards from west to east (Figure 5.13). The surface geology of the site comprised glacial till and clay in the uppermost near-surface.

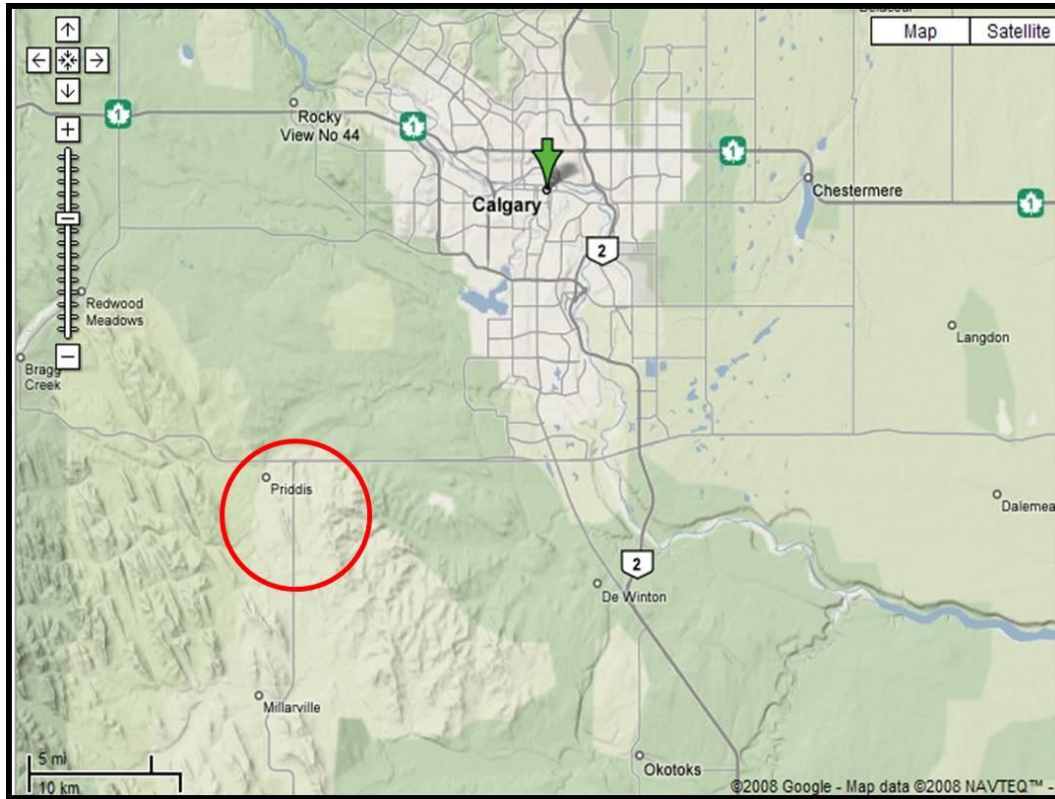


Figure 5.12. Location map of the test site at Priddis, Alberta.



Figure 5.13. CREWES students and staff provided a valuable help in the field. Each microphone was placed beside a geophone every 5 m (photos by Gabriela Suarez and Alejandro Alcudia).

5.2.1. Acquisition

The shallow seismic profile comprised two hundred ION Spike 3-C geophones (described in Chapter 4). A small 15-cm deep by 6-cm wide hole was drilled for each geophone using a gas-powered handheld auger. Each microphone was powered by a 9V PP3 battery (square) and connected to a line cable with eight take outs. Four extra Remote Acquisition Units (RAM's) were employed to support 32 microphones in total. The source was an environmental 17,000 Lb Vibroseis (IVI EnviroVibe) manufactured by Industrial Vehicles International. Four sweeps were performed at each source location to increase the S/N value in seismic field records. The radial components of the 3-C geophones were oriented east-west (in-line with the source-receiver azimuth) while the transverse components were oriented north-south (cross-line with the source-receiver azimuth). Please refer to Figure 5.14 for a schematic diagram and Table 5.2 for a summary of acquisition parameters.

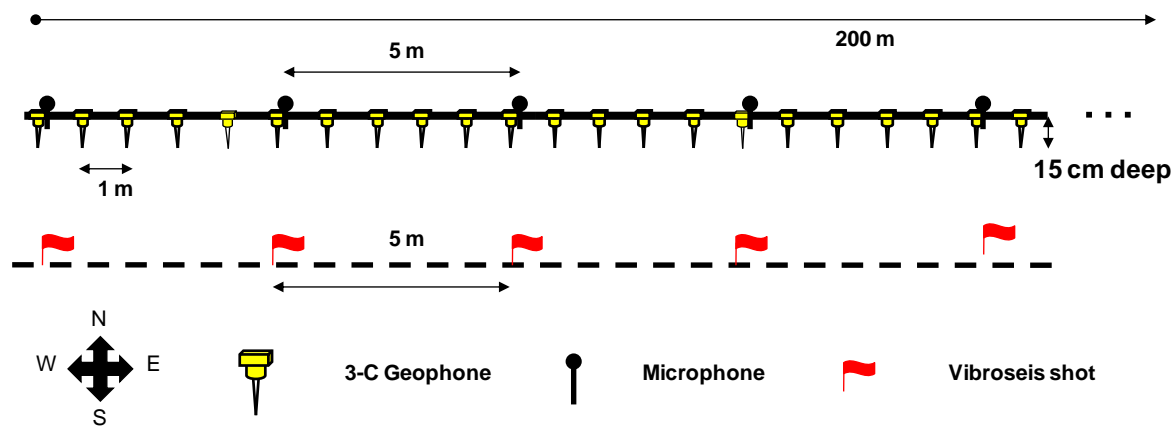


Figure 5.14. Acquisition layout at Priddis survey.

Table 5.2. Priddis survey acquisition parameters

Source	Mini Vibroseis (EnvirVibe)
Sweep	4 sweeps per shot point Linear 10-250 Hz, 10 sec
Sample interval	1 ms
Record length	11 seconds
Low-cut filter	3 Hz
High-cut filter	410 Hz
Microphone spacing	5 m
3C geophone spacing	1 m
Source interval	10 m (outside of spread) 5 m (within spread)

5.2.2. Data pre-processing and analysis

As stated in section 5.1.2, the air wave is fundamentally a sweep-like signal. The Gabor spectrum in Figure 5.15 corresponds to the theoretical Vibroseis sweep (10-250 Hz linear) used in this experiment. Figure 5.16 shows the Gabor spectrum of an uncorrelated microphone signal recorded a few metres from the EnviroVibe. Similar to the Pikes Peak survey, the highest amplitudes occurred at the highest frequencies and latest times. Note the presence of second and third harmonics in the signal, which suggested the proximity of the seismic source to the receivers in the seismic line.

Figure 5.17 shows examples of Vibroseis-correlated microphone and geophone data. A 250-ms AGC has been applied to these data for display purposes only. Note that the air wave is a high-frequency coherent noise in the geophone data, and a broad-band signal in the microphone data. Very good waveform consistency was observed in the microphone data with a few bad channels.

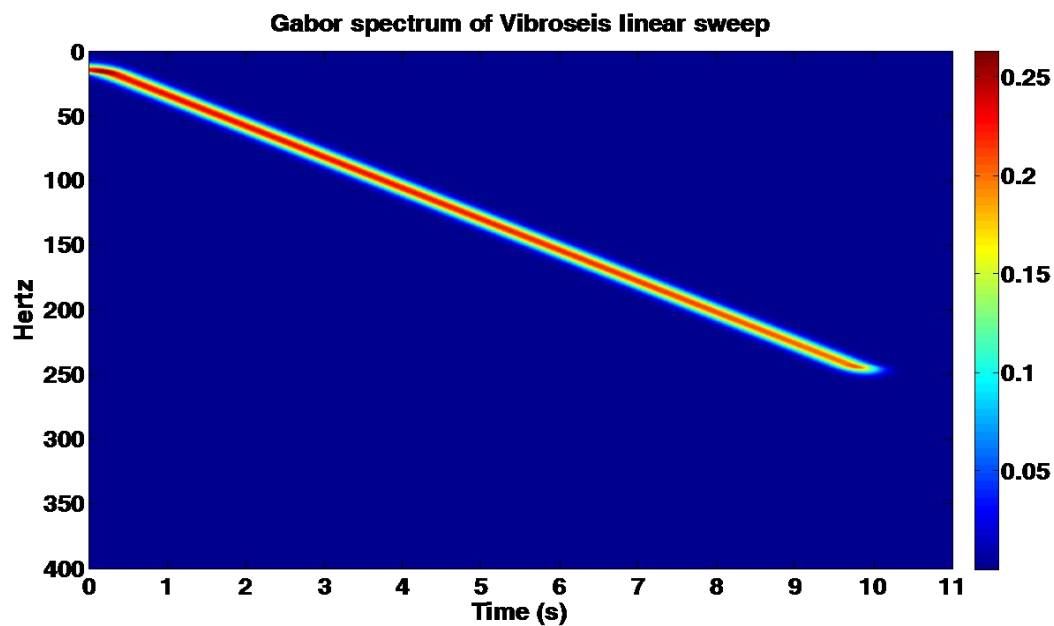


Figure 5.15. Time-frequency decomposition of the Vibroseis sweep used in the high-resolution near-surface survey at Priddis. The 10s sweep was linear from 10-250 Hz.

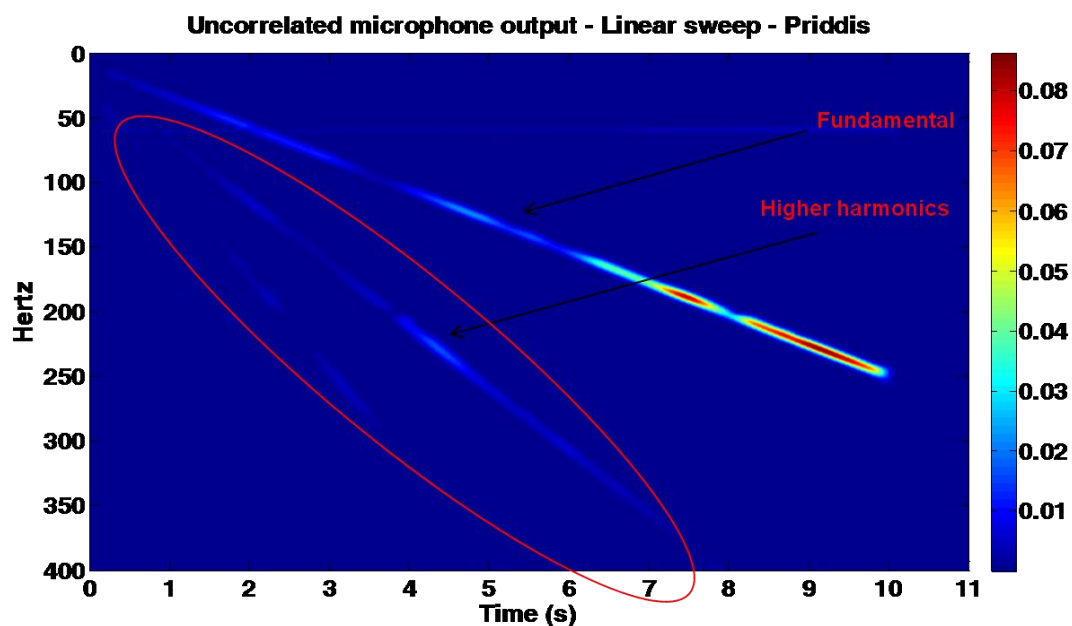


Figure 5.16. Uncorrelated microphone output recorded a few metres from the EnviroVibe and represented in the time-frequency domain. The sweep was linear from 10-250 Hz.

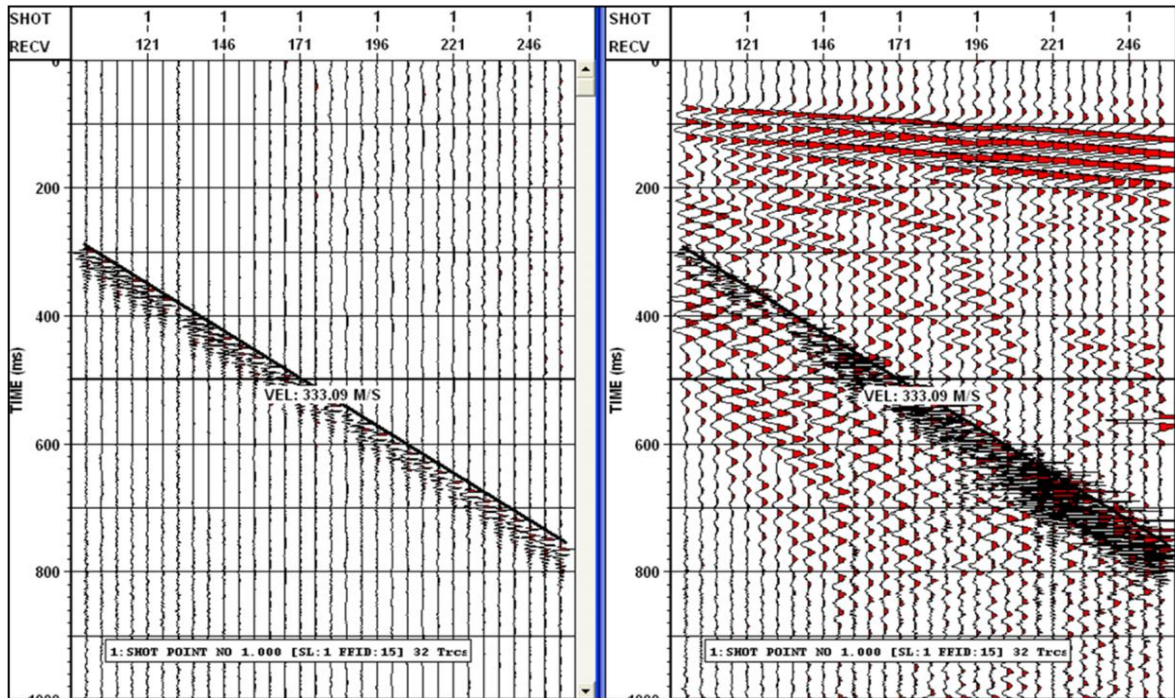


Figure 5.17. Common shot gather of microphone (left) and vertical component seismic data (right) with the Vibroseis source at 100m offset from station 101.

Figure 5.18 shows examples of symmetrical microphone and geophone shot gathers. As pointed out in section 5.1.2, strong correlation artifacts are introduced in the data after correlation due to harmonic noise in the uncorrelated data. Again, harmonic noise is generated by the non-linear coupling of the Vibroseis' baseplate to the ground, and it is especially problematic when the Vibroseis trucks are very close to the receivers as in this survey.

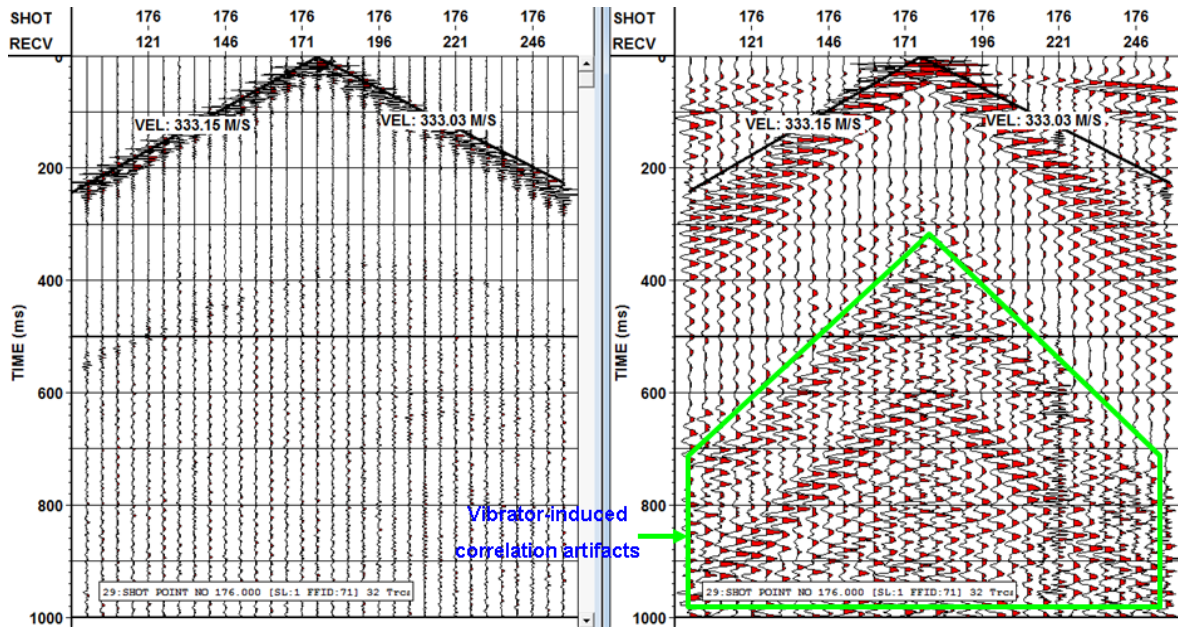


Figure 5.18. Common shot gather of microphone (left) and vertical component seismic data (right) with the Vibroseis source in split-spread shooting.

5.2.3. Coherence function

The ordinary coherence function (or coherence squared) is a measure of the linear dependence between two signals as a function of frequency f (Douze and Sorrells, 1975). In this case, the coherence function is an indication of how much power on a geophone trace can be predicted from the microphone output.

The definition of coherence is given by

$$|C(f)|^2 = \frac{\varphi_{MG}(f) \cdot \varphi_{GM}(f)}{\varphi_{MM}(f) \cdot \varphi_{GG}(f)} = \frac{|\varphi_{MG}(f)|^2}{\varphi_{MM}(f) \cdot \varphi_{GG}(f)}, \quad (5.1)$$

where φ_{MG} is the cross-power spectrum between the microphone signal (i.e., the excitation signal) and the geophone signal (i.e., the response signal), and φ_{MM} and φ_{GG} are auto-power spectra of the microphone and geophone, respectively. The coherence function is a real-valued dimensionless function since the numerator is the magnitude squared of the cross-power spectrum and the denominator is the product of the auto-power spectra of the

two signals. The range of values of the coherence function is limited to values between 0 and 1. A coherence value close to one means a higher correlation (strong linear relationship), whereas a value close to zero means poor correlation at a particular frequency.

Figure 5.19 shows two coherence functions computed from the signals recorded at two different receiver stations in the Priddis survey. For frequencies between 110 and 250 Hz, the coherence function is close to 1 due to the high-frequency air wave. This is evident from the time domain waveforms as well. A rapid and effective method to suppress this noise would be a high-cut filter with corner frequency at 110 Hz. However, for some surveys (especially for shallow targets), we are forced to preserve high frequencies to resolve shallow reflectors. At frequencies between 25 and 50 Hz, there is less relationship between the microphone and geophone outputs. For frequencies below 25 Hz, the coherence values differ from station to station. For example, the coherence function for the first geophone and microphone pair in Figure 5.19 (left) shows strong linear relationship at low and high frequencies, but the second pair (right) shows strong linear relationship at high frequencies with moderate relationship at low frequencies. The large coherence values at low frequencies would suggest that the microphones recorded some of the low-frequency noise in the geophones. However, as shown in Figure 4.12, our microphone prototype frequency response is reliable from about 30 Hz and above. Coherence results for frequencies below 30 Hz are not reliable.

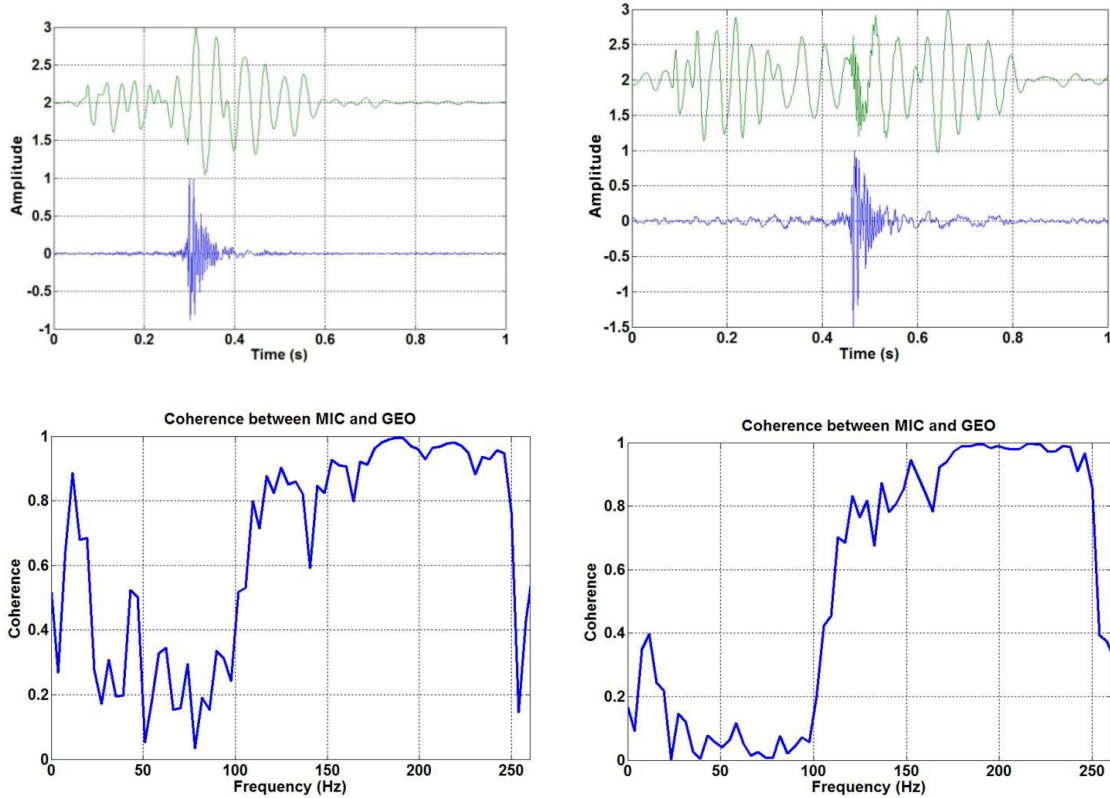


Figure 5.19. Coherence functions computed for two pairs of geophone and microphone signals.

5.2.4. Air-ground transfer function

In the last section, I showed that maximum coherence of air pressure and ground velocity occurred at frequencies greater than 100 Hz. A model of the amplitude decay of an acoustically-induced wave propagating in the ground can be determined by regression analysis of the high -frequency component of geophone data. The air wave recorded on the geophones showed amplitude decay with distance. Its amplitude decay can be characterized as an exponential function of the form:

$$AW(x) = a \cdot e^{bx}, \quad (5.2)$$

where x is distance, and a and b are coefficients determined by regression analysis. Another form of exponential function is given by

$$AW(x) = a \cdot e^{bx} + c \cdot e^{dx}, \quad (5.3)$$

where a , b , c and d are coefficients determined by regression analysis (i.e., curve fitting in the least-squares sense) of the high-frequency airwave in the geophone data. Regression analysis was done with the aid of the MATLAB Curve Fitting toolbox.

Figure 5.20 shows a high-resolution geophone shot record with 200-ms AGC applied for display purposes. Trace spacing for this shot is 1m. Note that the air wave is not obvious because the low-frequency surfaces waves dominate across the entire shot. However, if a 120-250 Hz band-pass filter is applied to the data, the air wave becomes dominant (Figure 5.21). Note that the air wave exhibits obvious amplitude decay with distance.

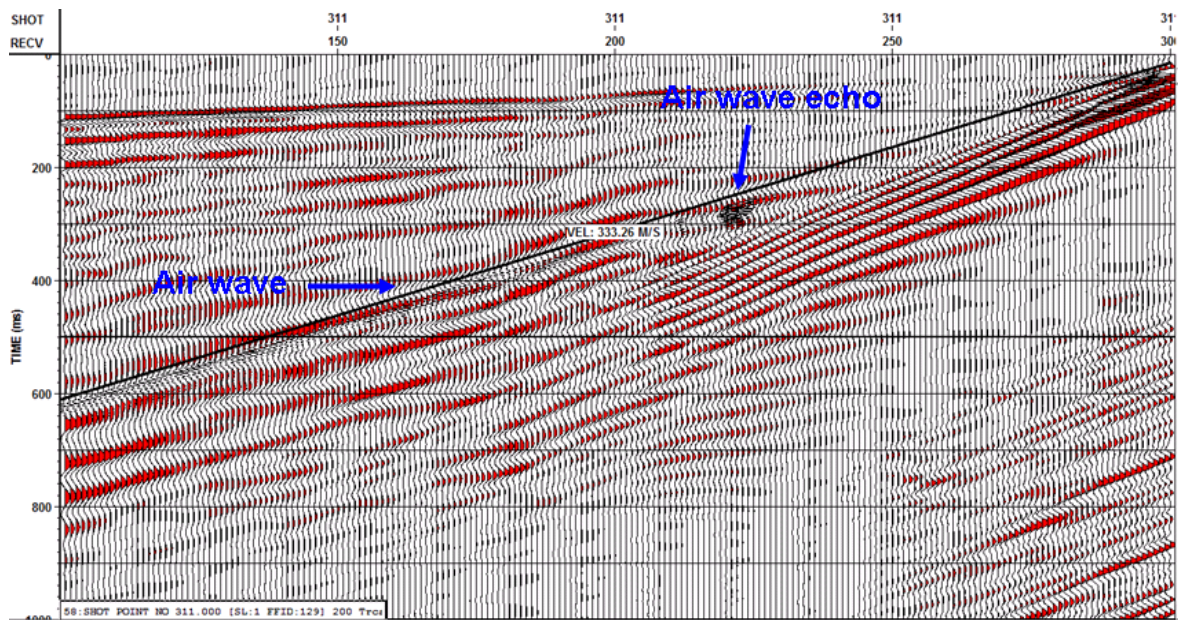


Figure 5.20. Vertical component of the geophone for a shot point located at station 301 (far right). Trace spacing is 1m. A 200-ms AGC was applied to the raw data.

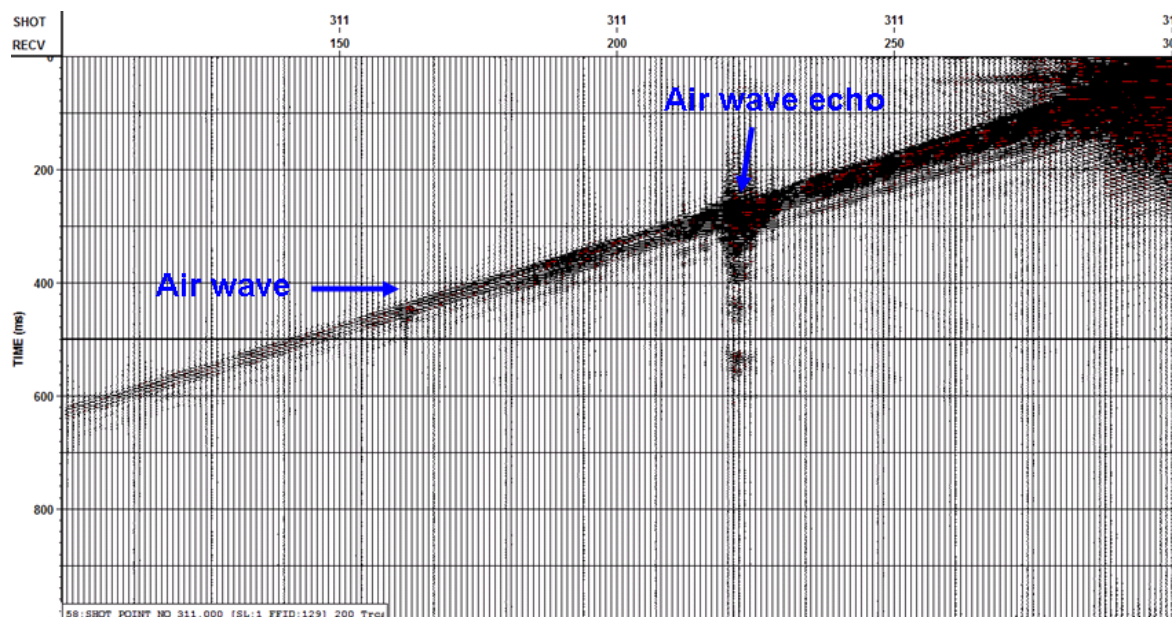


Figure 5.21. Vertical component of the geophone for a shot point located at station 301 (far right). Trace spacing is 1m. A 120-250 Hz band-pass filter has been applied to the data.

A good model fit could be achieved using peak amplitude values from each high-pass geophone trace. However, any amplitude anomaly must be removed prior to curve fitting to minimize the mean-square error. For instance, the high-pass version of the shot in Figure 5.20 (Figure 5.21) showed that there was an echo of the air wave travelling in opposite direction to the primary air wave. This echo was generated by reflection of the air wave from the recording truck. A 200-ms AGC was applied to the shot gather in Figure 5.21 (Figure 5.22) for further analysis of the echo. Note that the echo has opposite LMO direction. In next chapter, I show that this echo could not be removed from the geophone records by combining microphone and geophone data.

A LMO correction was applied to the data to flatten the air wave arrival. A velocity of 333 m/s was used because this is the speed of the sound in the air at 3° C. This velocity is highly variant and dependent on air temperature and air density. At -10° C its speed is about 325 m/s while at 10° C it travels at 337.5 m/s. It is important to note that the sound speed in

air is not significantly dispersive. Figure 5.23 shows the shot gather after LMO correction and amplitude anomaly removal. Next, peak amplitude values were exported into the MATLAB Curve Fitting toolbox to compute the coefficients for the exponential amplitude decay models suggested in Equations 5.2 and 5.3. Only results for Equation 5.3 are listed in Table 5.3 because this model gave the best fit. Figure 5.24 shows results for both models.

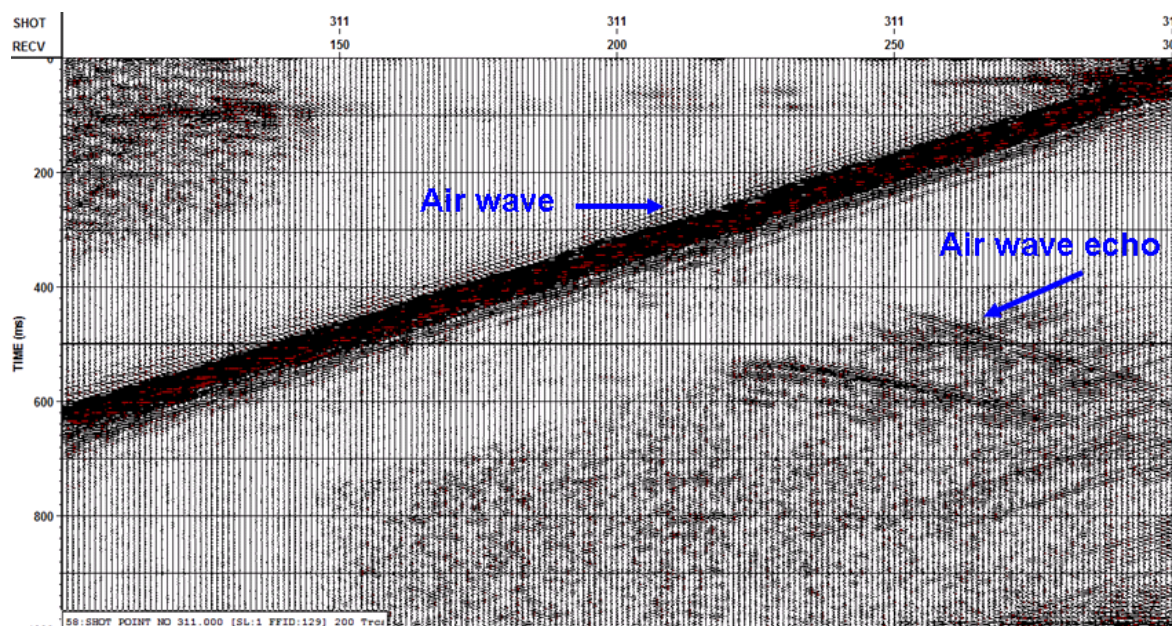


Figure 5.22. Same as Figure 5.20 with a 200-ms AGC for display purposes.

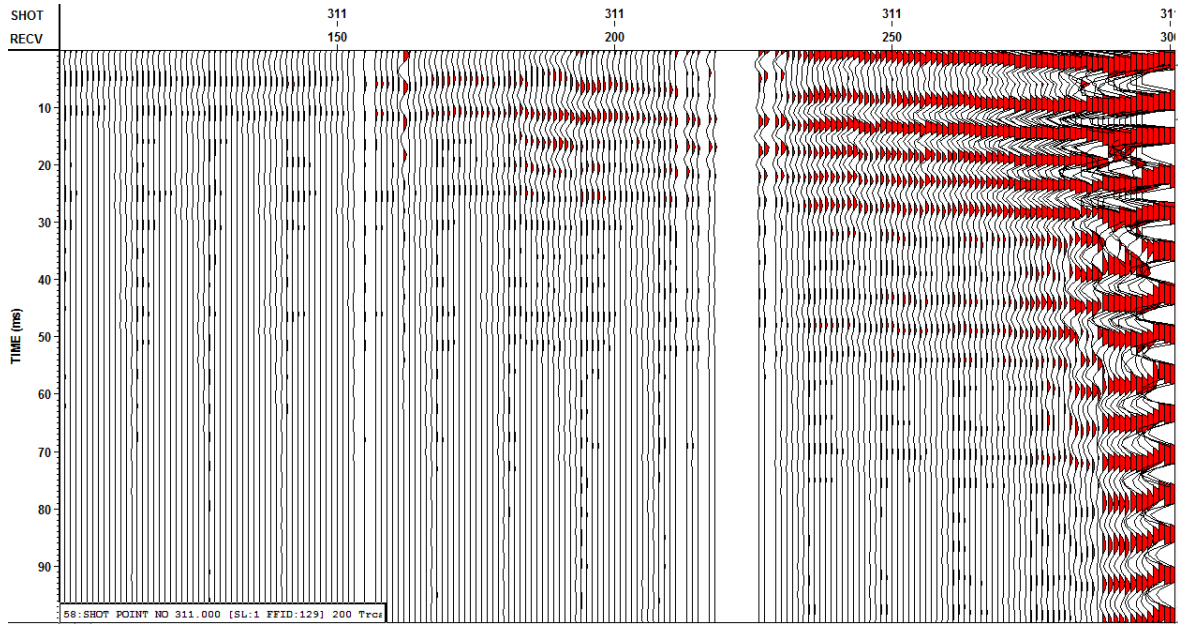
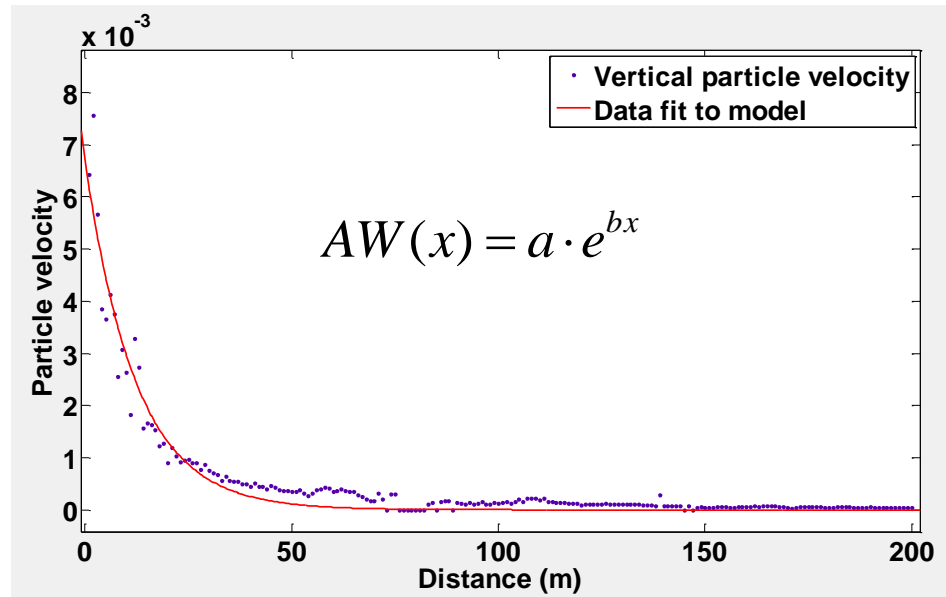


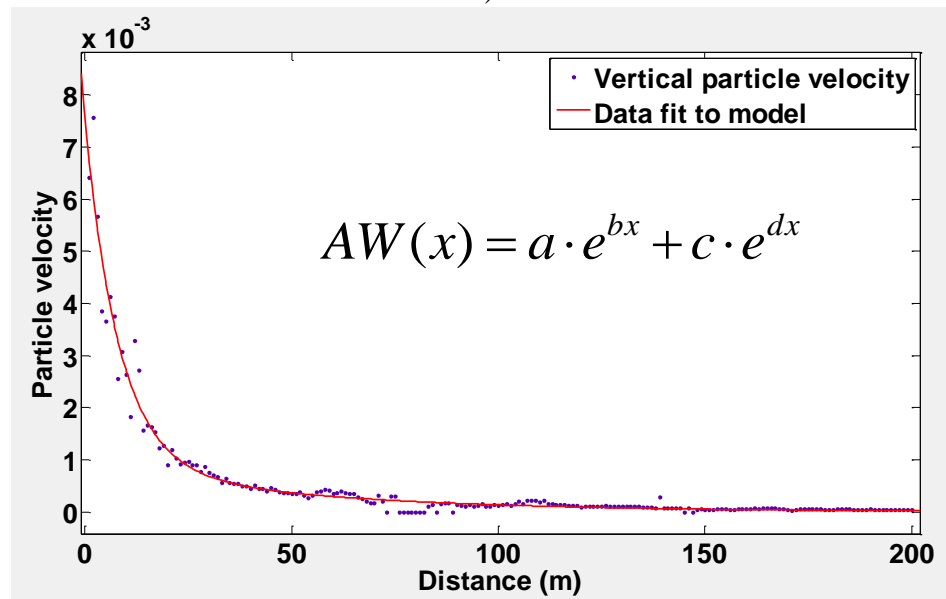
Figure 5.23. LMO-corrected geophone data for regression analysis.

Table 5.3. Equation 5.3 coefficients obtained by curve fitting.

	Coefficients		95% Confidence bounds	
	a	0.006618	0.006223	0.007012
b	-0.1225	-0.137	-0.108	
c	0.0009132	0.0005404	0.001286	
d	-0.01915	-0.02544	-0.01287	
Mean Square error	0.0001972			



a)



b)

Figure 5.24. Results of geophone data fit to the exponential amplitude decay models.

CHAPTER FIVE: AIR WAVE ATTENUATION IN SEISMIC SIGNALS USING AIR-PRESSURE MEASUREMENTS

A procedure to remove air noise from seismic records by the combination of a microphone signal with the contaminated geophone signal in the time-frequency domain is presented. In general, the approach depends upon the degrees of correlation and coherence between the pressure signal recorded on the microphone and the ground velocity signal recorded on the geophone. The algorithm is based on a type of localized Fourier transform and makes use of the similar local spectra characteristics between the reference signal and its associated component in the seismic signal. The main advantage of this approach is that a completely independent air pressure measurement is recorded in the field to provide a reference for the contaminated geophone signal. This reference signal can be used in seismic data processing to estimate and remove the airborne noise from seismic records in several ways. One robust and deterministic way is given by designing a filter in the time-frequency domain with the aid of the Gabor transform.

This chapter is organized as follows: first, I review the fundamentals of time-frequency analysis with a particular emphasis on the Gabor transform and its application to nonstationary filter design. Second, I introduce the proposed algorithm for air-noise attenuation in the Gabor domain with graphic examples of how it operates. Third, I apply the proposed algorithm to a number of common shot gathers from two different multicomponent surveys in the Western Canada Sedimentary Basin (WCSB). Other methods in the time domain may be designed via Wiener filter theory and Least-Squares adaptive filters. These methods are briefly discussed in Appendices A and B, respectively.

6.1. Time-frequency analysis

Most real world signals, representing the evolution of a physical process over a finite period of time, are of finite energy and nonstationary. Seismic signals and biomedical signals are good examples. In a nonstationary physical process, the amplitude and frequency content of the signal describing the process evolves over time. The amplitude variations of a signal are conveniently represented in the time domain but only limited information about how often these variations occur and change over time (i.e., frequency) can be obtained. Engineers and scientists make use of a signal representation in the frequency domain to identify the rate of change in amplitude, analyze systems and design filters. This has been traditionally accomplished by means of the Fourier transform. The Fourier transform decomposes a signal as the sum of weighted sinusoidal functions extending from negative infinity to positive infinity in time (Qian and Chen, 1999). The Fourier representation describes which frequencies are present in the original signal by a simple interpretation of pure tones and overtones (i.e., second-order harmonics) in a plane of frequency versus weights (i.e., the magnitude of the Fourier coefficients). However, the Fourier transform is not always the most helpful tool to analyze real-world signals because the power spectrum (i.e., the square of the Fourier transform) does not reveal how the frequency content evolves over time. Let's consider the example below.

Figure 6.1 depicts the Fourier transform and the Gabor transform of a microphone output recorded close to a Vibroseis source. It is the uncorrelated pressure signal that represents the sound pressure variations emitted by the Vibroseis system as the seismic energy is being exerted into the ground. As stated above, in the time domain the waveforms offer little obvious information about the frequency content and how it changes over the 20

s record length. For example, this particular signal has three lobes that produce notches in the frequency content as depicted in the amplitude spectrum, but we cannot establish the correspondence of a particular frequency notch to a particular lobe in time. In other words, we are able to identify the frequency tones and overtones but cannot determine how they change over time. By analyzing the signal in time and frequency jointly, through the Gabor transform, not only can we see how the frequencies change but we also can see the intensity of the frequency components by the relative brightness levels. The Gabor spectrum reveals the nonlinearity of the Vibroseis sweep and the linearity of other events such as the 60 Hz power-line noise and its higher harmonics.

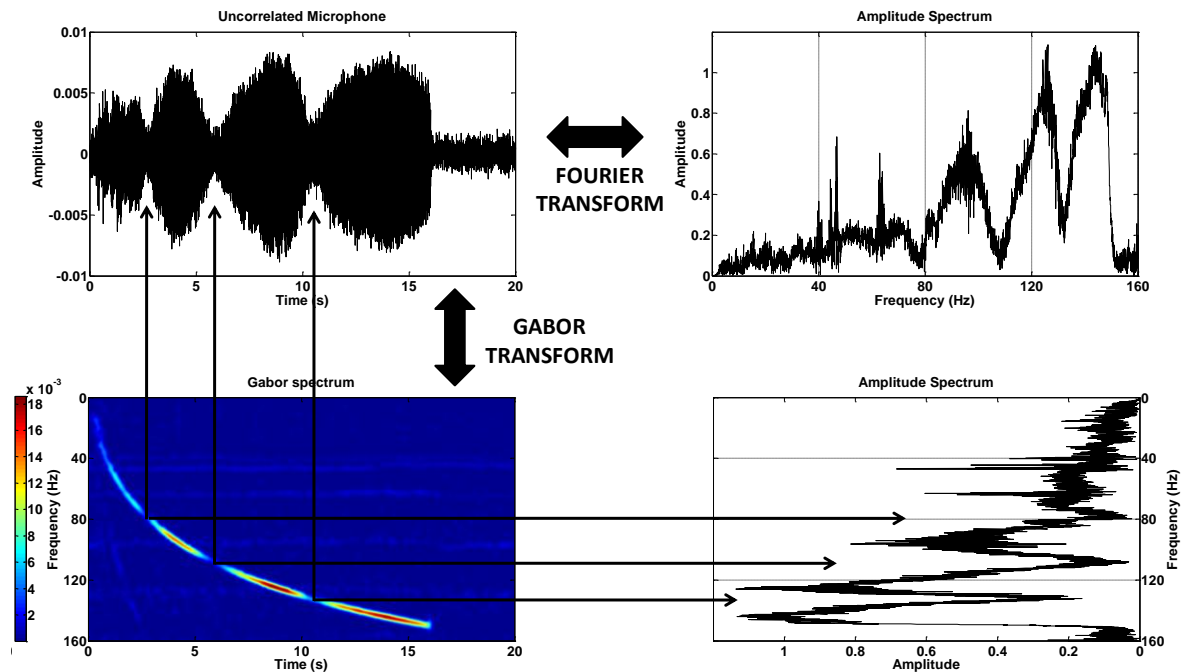


Figure 6.1. Fourier and Gabor transforms of an uncorrelated Vibroseis signal (i.e., the air wave) recorded with a microphone. The upper left is the signal of interest represented in the time domain. Signal representations are achieved using the Fourier transform for the frequency domain representation (upper right) and the Gabor transform for the joint time-frequency domain representation (lower left).

6.2. Nonstationary filters in the Gabor domain

The Gabor transform provides a means to measure the local spectral content of a signal. Essentially, the Gabor transform is a time-frequency method based on the localized version of the Fourier transform. In other words, for any time instant t the given signal s is multiplied (or modulated) by a Gaussian window of certain width and centered at time t_0 and the ordinary Fourier transform of this windowed signal is taken (Lamoureux and Adler, 2004). If a suite of windows positions is used to compute a collection of local spectra, the result is a time-frequency decomposition of the signal (Margrave et al., 2005). According to Qian and Chen (1999), Lamoureux and Adler (2004), Margrave et al. (2005), and others, if a signal can be reconstructed from a time-frequency decomposition, then a nonstationary filter can be designed by modifying the decomposition first. This is the fundamental idea behind our method for air wave attenuation.

One simple but non-automatic way to design a nonstationary filter is by interactive picking with a computer mouse. This “on the fly” design is an effective way to identify regions in the Gabor domain that should be selectively filtered (Lamoureux and Adler, 2004). However, a semi-automatic design can be achieved by constructing a “mask” function from a reference signal. Then, Gabor filtering is achieved by multiplying the Gabor spectrum or coefficients by the “mask” or “filter” function. This observation suggests that we can use a mask to filter out the desired Gabor coefficients from the noise background or the undesired Gabor coefficients from the signal space, and then reconstruct the time waveform via the Gabor expansion (i.e., the inverse Gabor transform).

The Gabor transform cannot achieve arbitrarily fine resolution in the time and frequency domain simultaneously due to the limitations imposed by the uncertainty

principle (Qian and Chen, 1999). However, it is the Gaussian function that achieves the optimal time-frequency decomposition because the product of its time and frequency is minimal. In other words, the smoothness of the Gaussian window function guarantees fast decay of the frequency components of the window.

The discrete Gabor transform implementation of Margrave et al. (2005) is used in this thesis. It is a discrete approximation that is based on a convenient summation property of Gaussians. However, if n windows are required and the trace is of length N , then the computation effort is proportional to $nN \log 2N$. When using Gaussian windows, each windowed trace segment is as long as the original trace. A Gabor transform pair is available in the CREWES MATLAB Toolbox. A complete overview of this implementation and applications to seismic data deconvolution can be found in Margrave et al. (2005)

6.3. Method of air wave attenuation in the Gabor domain

Figure 6.2 shows the time-frequency decomposition of a geophone signal and a microphone signal. A Gaussian window of 25-ms width and shifted at 1ms time increment has been used to compute the Gabor spectra in Figure 6.2. The geophone Gabor spectrum shows that most seismic energy lies below 100 Hz. It also shows that the air wave energy is broadband at about 350 ms. Early seismic arrivals, however, show some weak high-frequency energy above 100 Hz that share the frequency space of the airwave. These components would be lost if a band-pass filter is applied to the geophone data in attempt to remove the air wave. This is a typical scenario where a nonstationary filter must be used. However, note that the microphone Gabor spectrum offers a fairly good air wave reference that could be used to filter out the air wave in the geophone. In this case, the shapes of the air wave in both sensors are very similar. It is obvious from this example that a “mask” or

“filter” function can be constructed from the microphone Gabor spectrum. Therefore, a simple method for air wave attenuation in the Gabor domain has been developed.

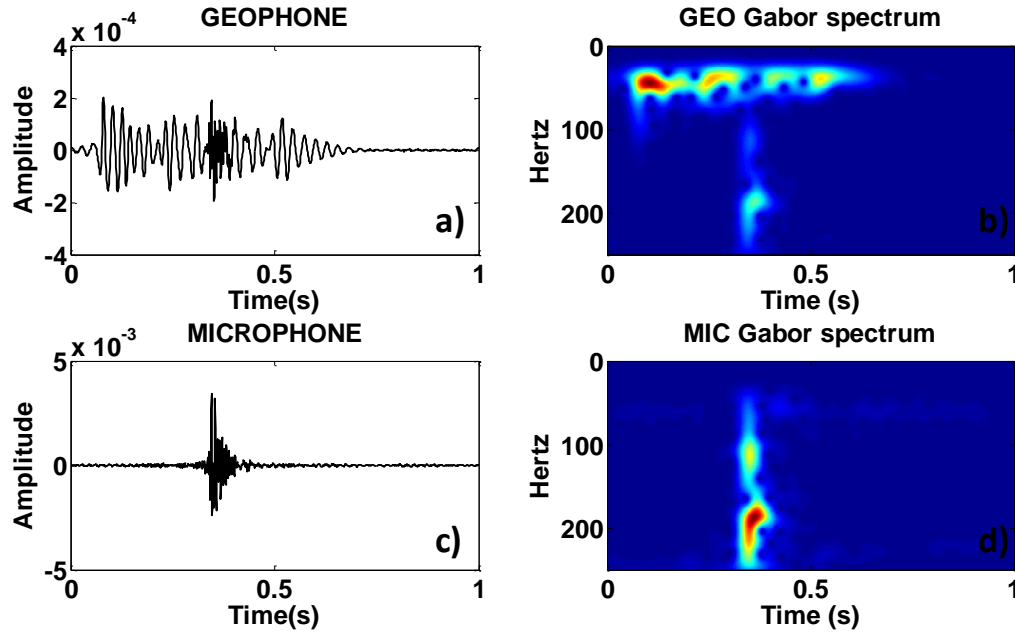


Figure 6.2. a) Geophone signal and b) microphone signal in the time domain. c) Geophone signal and d) microphone signal in the time-frequency domain (Gabor domain).

A graphical explanation of the method is offered in Figure 6.3. The procedure is explained as follows:

- Compute the Gabor transform of microphone and geophone raw signals and take the magnitude of the Gabor coefficients
- Find the maximum Gabor coefficient ($maxGC$) in the microphone Gabor spectrum
- Set a threshold equal to $maxGC/n$, where n is an integer between 1 and 10. This parameter determines the size of the region in the geophone Gabor spectrum that will be filtered

- Find all indices (coefficients) in the microphone Gabor spectrum matrix that equal or exceed the threshold and substitute their values with the minimum Gabor coefficient in the geophone. Make all coefficients below the threshold equal to one. This modified microphone spectrum is called a “mask” filter. The threshold determines the extent of the “mask” area in the geophone spectrum
- Multiply the geophone Gabor spectrum with the “mask” filter
- Compute inverse Gabor transform of the filtered geophone spectrum
- Repeat the procedure for next trace in common shot gather.

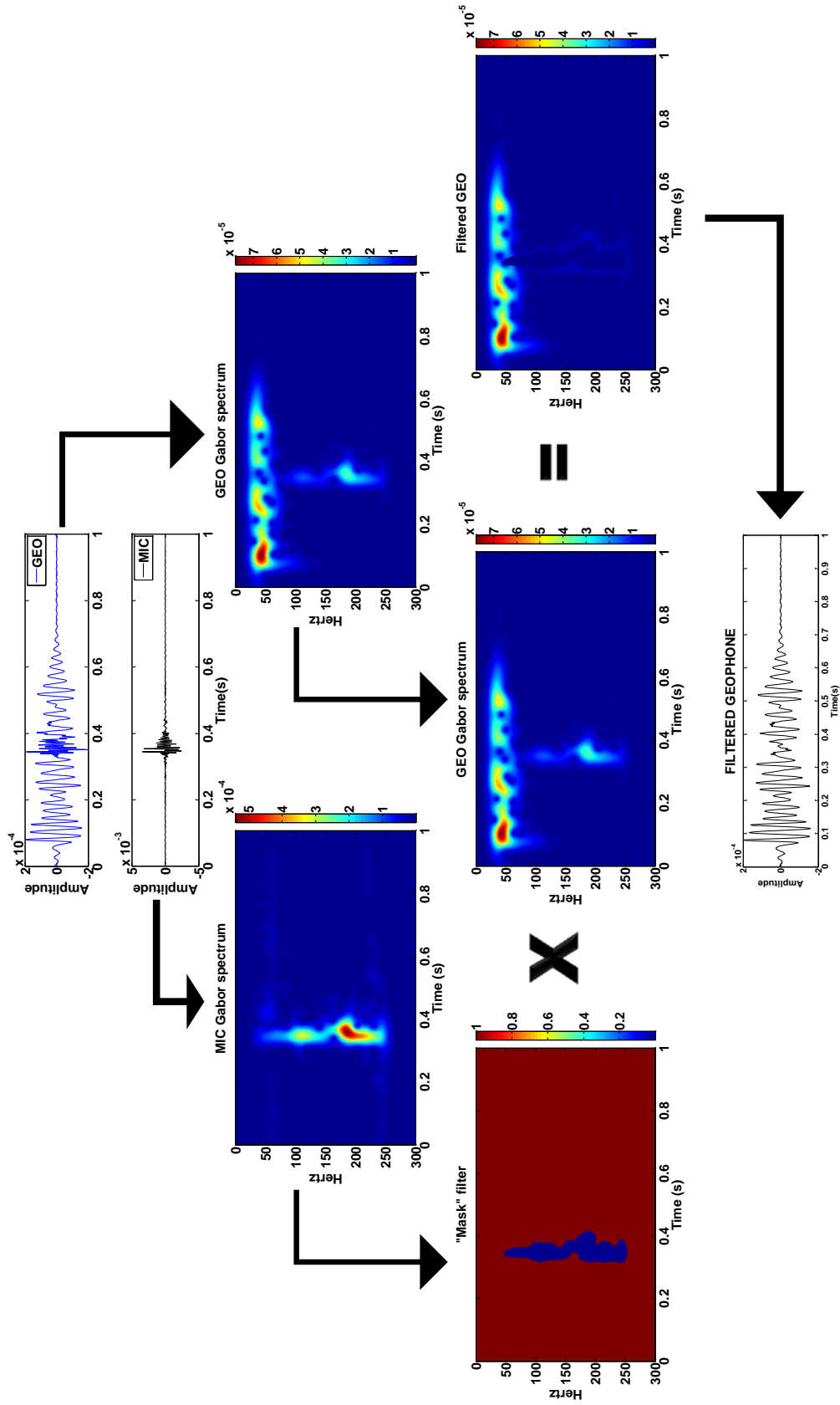


Figure 6.3. Step by step schematic of the air wave attenuation method by combination of microphone and geophone signals in the time-frequency domain (Gabor domain).

6.4. Field data examples: Pikes Peak and Priddis 3C-2D surveys

This method for air wave attenuation was applied to a number of common shot gathers from the experiments described in Chapter 5. Preliminary testing was required to determine appropriate parameters that satisfy both accuracy and computer time. This can be done by selecting a random trace from a shot gather. Different window widths and time increments should be tested prior to filter application over the entire shot gather. From this experience, it was found that a 50 ms window gave good results for seismic data of 4s length (Pikes Peak data). For 1s seismic data (Priddis data), a 25 ms window yielded good results. In both cases, a 1 ms time increment was used for the Gabor transform computations. Similar to the Gabor transform parameters, appropriate values for the microphone spectrum thresholds were found based on testing. A threshold of $maxGC/5$ was appropriate for the Pikes Peak data, while a threshold of $maxGC/8$ was required for the Priddis high-resolution near-surface survey. The general rule was: the bigger the parameter n the larger the “mask” area. Hence, for strong air wave energy, n needs to be large.

Figure 6.4 shows a single-trace example from the Priddis survey before the microphone and geophone combination and after the filter was applied. The difference between the original and filtered trace was computed to measure the effectiveness of the procedure for this example. Note that the air wave has been completely removed without perturbing other events in the seismic trace. Figure 6.5 shows another single-trace example from the Peak survey.

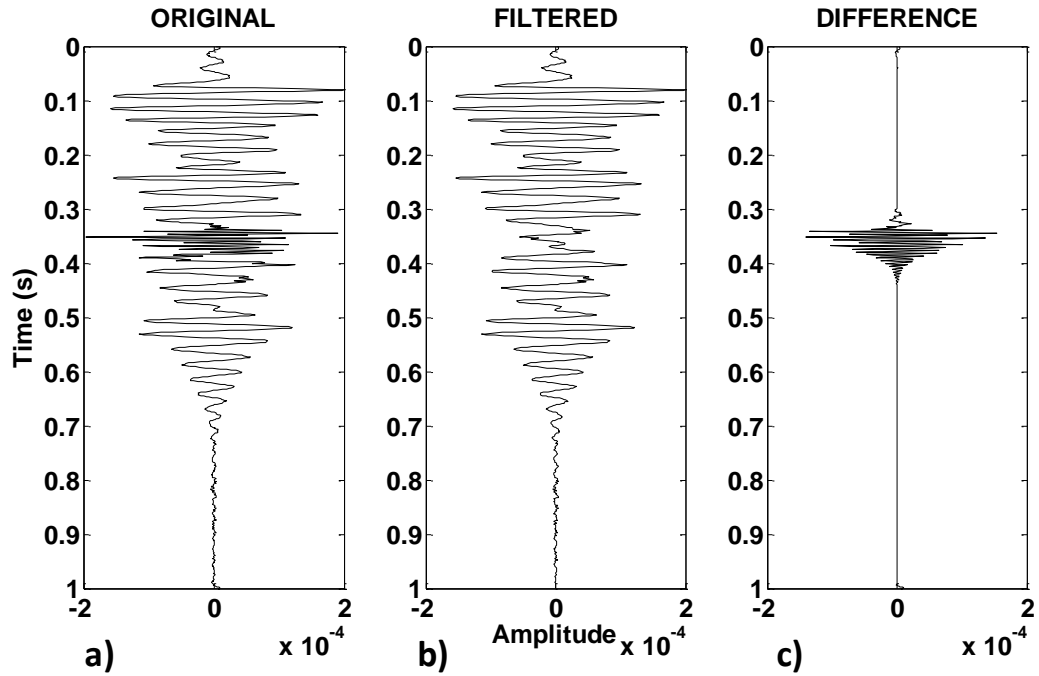


Figure 6.4. A single-trace example from the Priddis survey. a) Original trace, b) filtered trace, and c) difference between original and filtered trace.

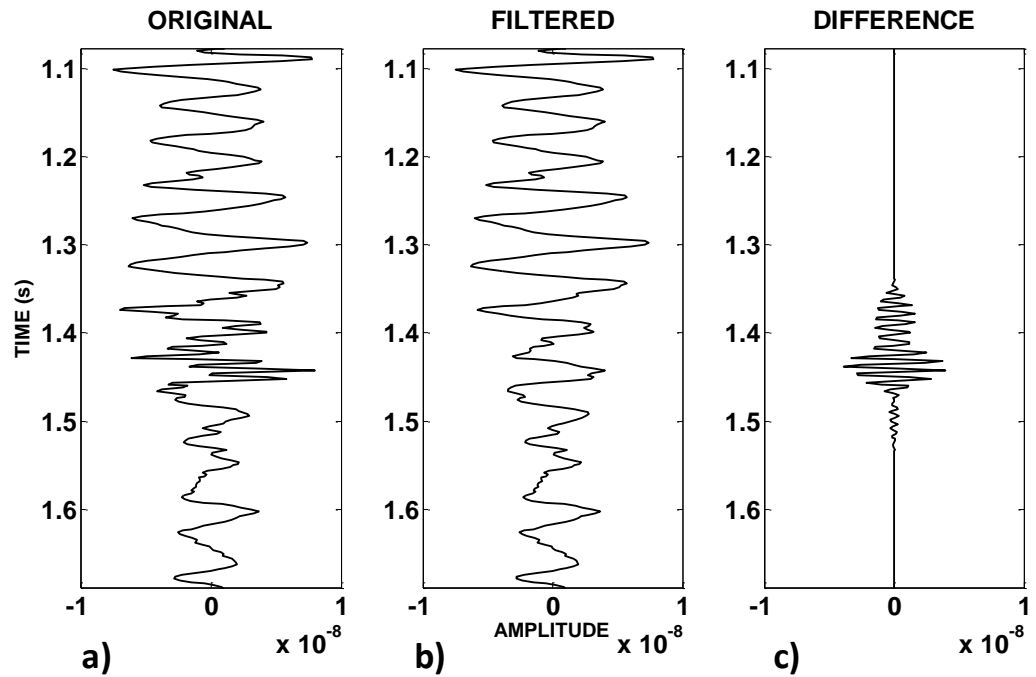


Figure 6.5. A single-trace example from the Pikes Peak survey. a) Original trace, b) filtered trace, and c) difference between original and filtered trace.

The shot gather on top of Figure 6.6 is the vertical array data from Pikes Peak before applying signal combination. An automatic envelope correction (amplitude correction) was applied for display purposes only. The shot gather at the bottom of Figure 6.6 is a filtered version of these data. A 50-ms window and 1ms time-shift were selected for this example as mentioned above. The threshold of the microphone Gabor coefficients was set to $\text{maxGC}/5$, which defined a sufficient “mask” area. Note that the air wave has been cancelled to a large extent while preserving the frequency content of other seismic events. An exception occurred at about 0.6 s in trace 105 because the microphone trace at this station was bad. These results were exported to VISTA processing for a better color display (see Figure 6.7).

Figure 6.8 is an example from the high-resolution survey conducted at the Rothney Astrophysical Observatory. The vertical component data was decimated to match the microphone spacing (5 m). Traces 257-301 are not shown because the microphones covered 155 m of line only. The Vibroseis shot point was located about 100 m west of receiver station 101. Therefore, the air wave arrival was at about 300 ms (for a speed of sound in air of 333 m/s). A 25 ms window and 1 ms time-shift were selected for the Gabor transformations. A threshold of $\text{maxGC}/8$ was used to construct the “mask” function. Note that the air wave has been attenuated while preserving the frequency content of other seismic events, as in the Pikes Peak example. The “mask” filter in the Gabor combination method failed to attenuate the air wave in traces 216 and 221 because the acoustic wavefront in the air was reflected by the recording truck at these locations.

One of the advantages of this methodology is that air pressure measurements are given for each station. Therefore, spatial aliasing does not have any impact over filtering results. For instance, Figure 6.10 shows an f-k spectrum comparison of the shot gathers before and

after filtering. Some residual air wave energy remains in the data due to the air wave echo reflected by the recording truck.

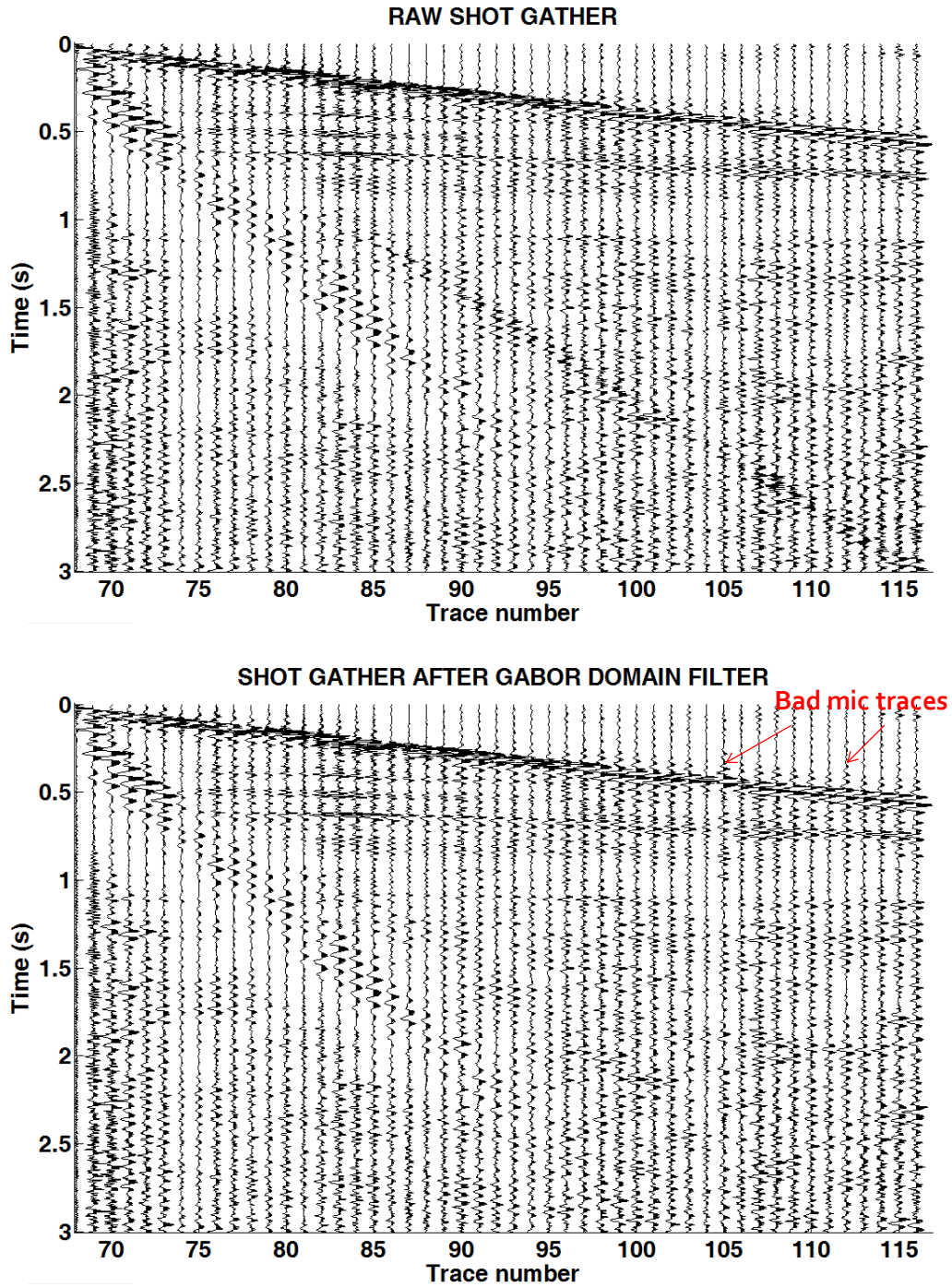


Figure 6.6. Shot gather from the Pikes Peak data set. A 50 ms window and 1 ms time-shift was used for this shot gather. Note that the air wave has been attenuated while preserving the frequency content of other seismic events.

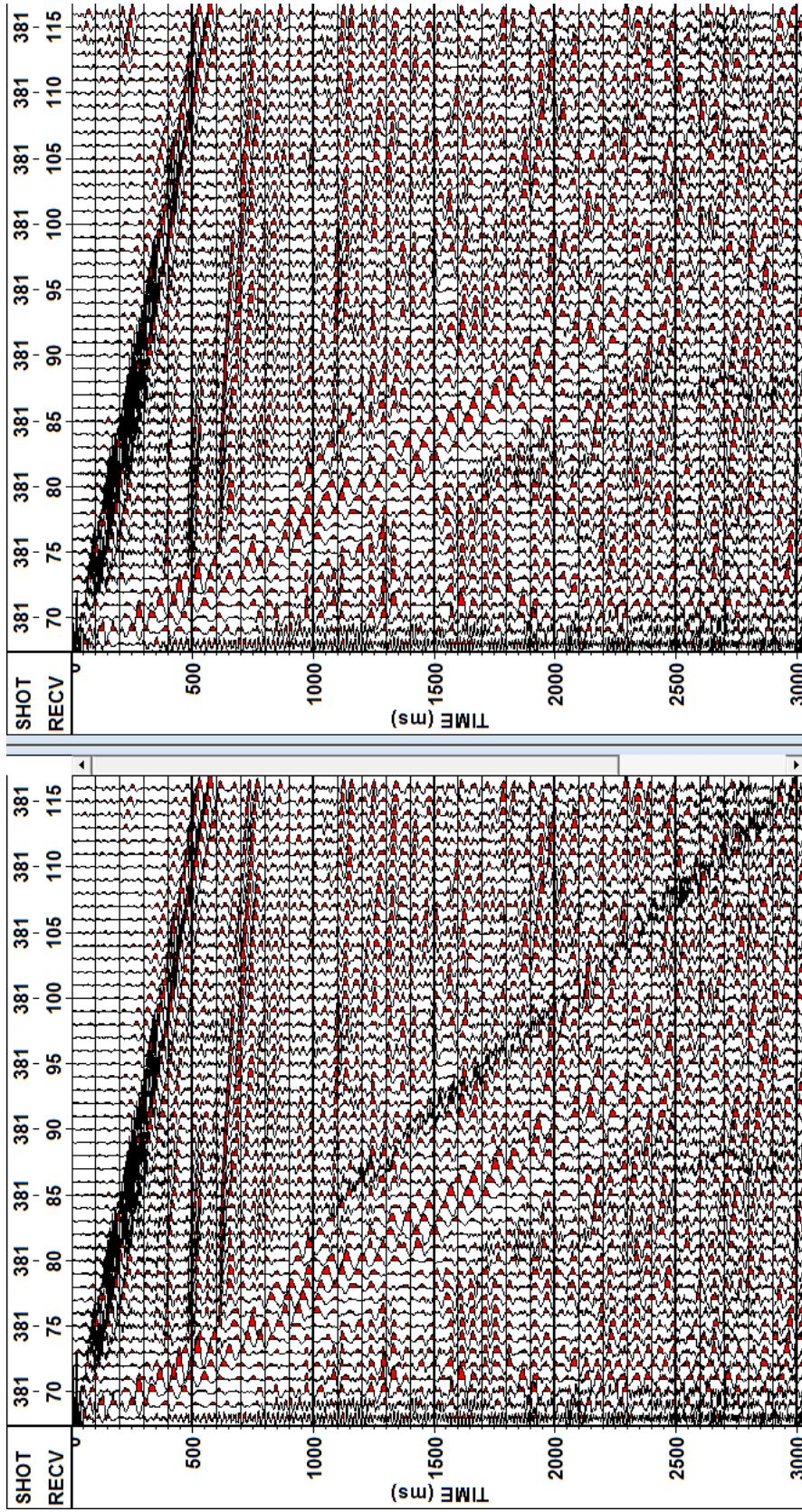


Figure 6.7. Common shot gather from Pikes Peak survey before and after applying our Gabor combination method. A 50 ms Gaussian window shifted at 1 ms increments was used for the Gabor transformations. The threshold for constructing the “mask” filter was set to $maxGC/5$.

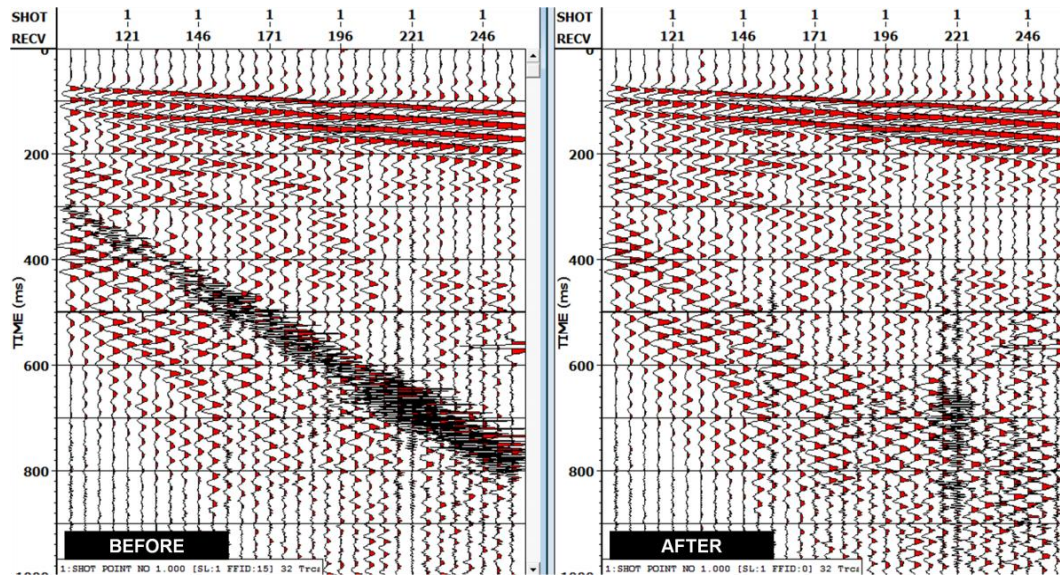


Figure 6.8. Common shot gather from the high-resolution near-surface survey before and after applying our Gabor combination method. A 25 ms Gaussian window shifted at 1ms time increment was used for the Gabor transformations. The threshold for constructing the “mask” filter was set to $maxGC/8$.

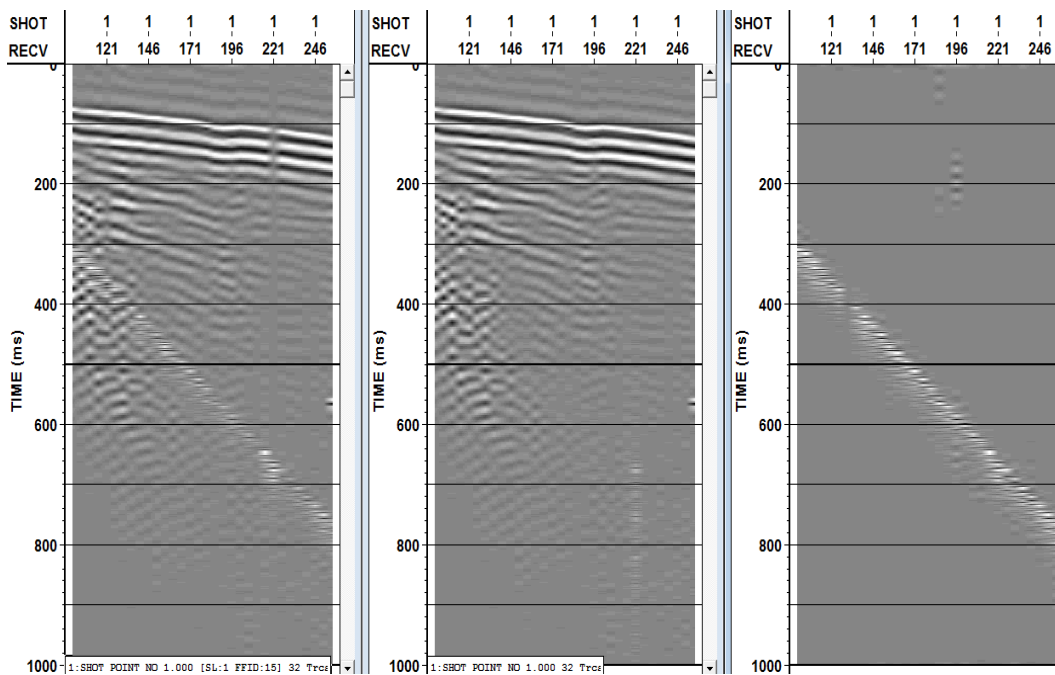


Figure 6.9. Same example as in Figure 6.8 showing the original shot record (left), its filtered version (centre) and the difference between raw and filtered data (right). Displays have been changed to variable density and amplitudes scaled relative to the peak amplitude on each shot record.

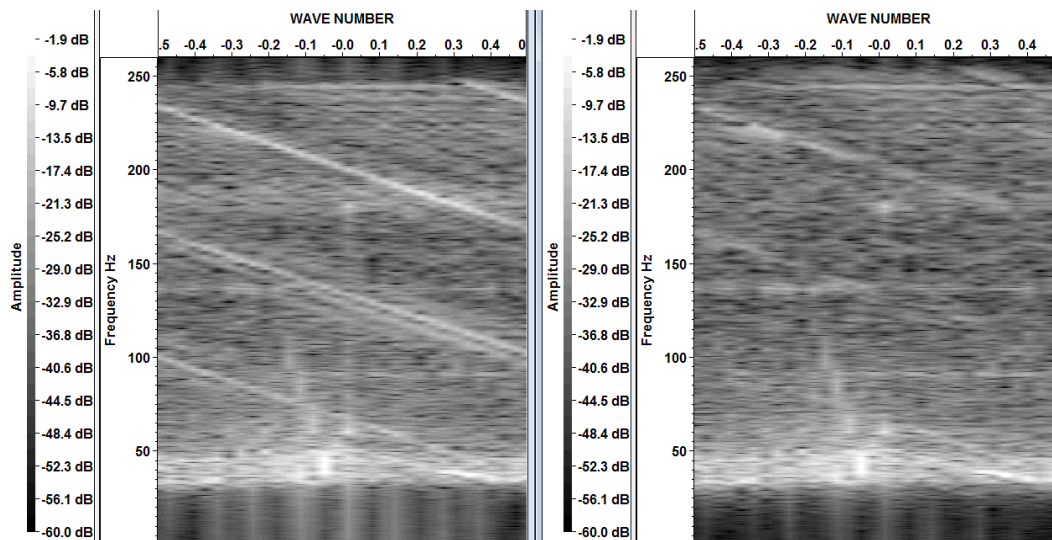


Figure 6.10. f-k spectra of shot gathers shown in Figure 6.8. Note that the air wave is spatially aliased in the original data and wraps around at about 100 Hz (left). The Gabor combination method attenuated the aliased air wave to a great extent. However, some residual air wave remains in the data.

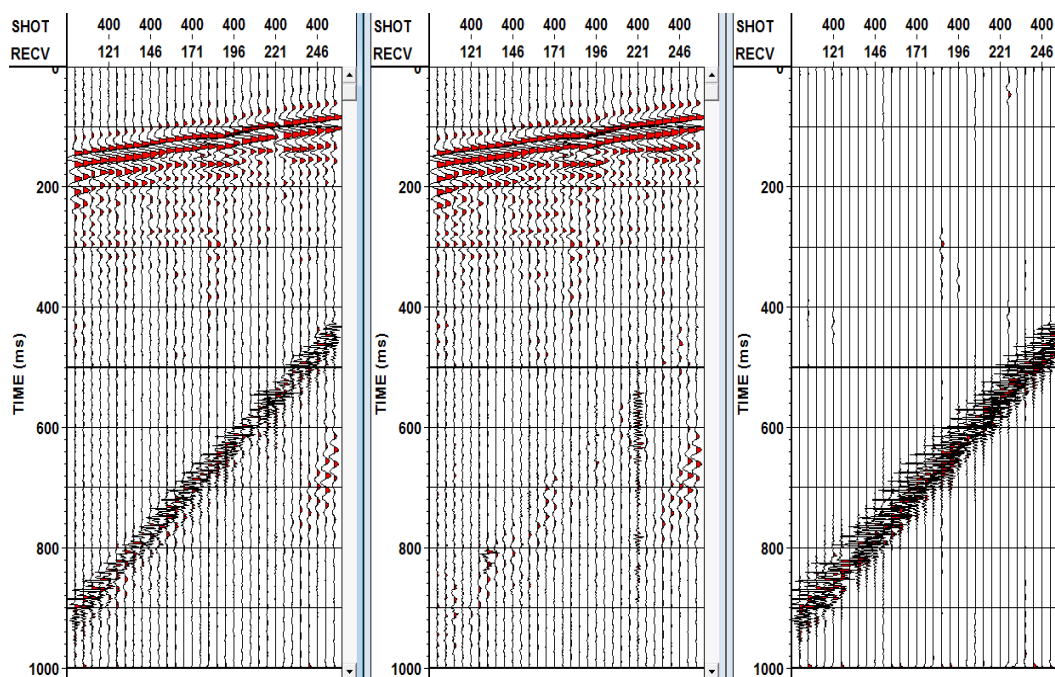


Figure 6.11. Another shot gather from the Priddis high-resolution survey with the same filter parameters as in the example for SHOT 1. The original data is shown on the left, its filtered version is shown in centre panel, and the difference between original and filtered data is shown on the right. The amplitudes have been scaled relative to the peak amplitude on each shot record.

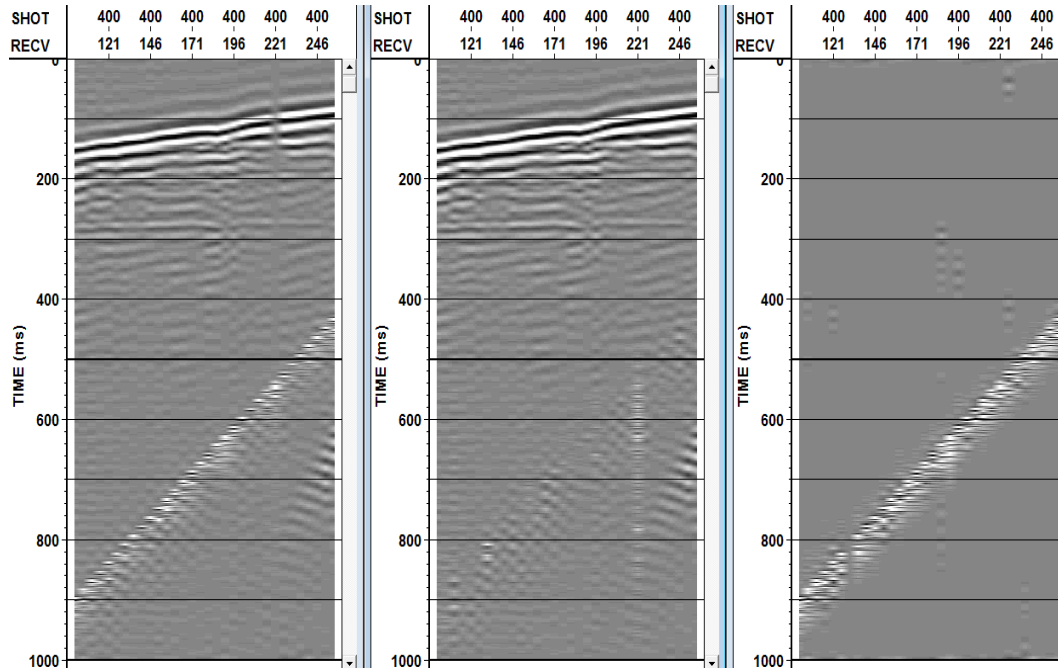


Figure 6.12. Same example as in Figure 6.11 showing the original shot record (left), its filtered version (centre) and the difference between raw and filtered data (right). Displays have been changed to variable density.

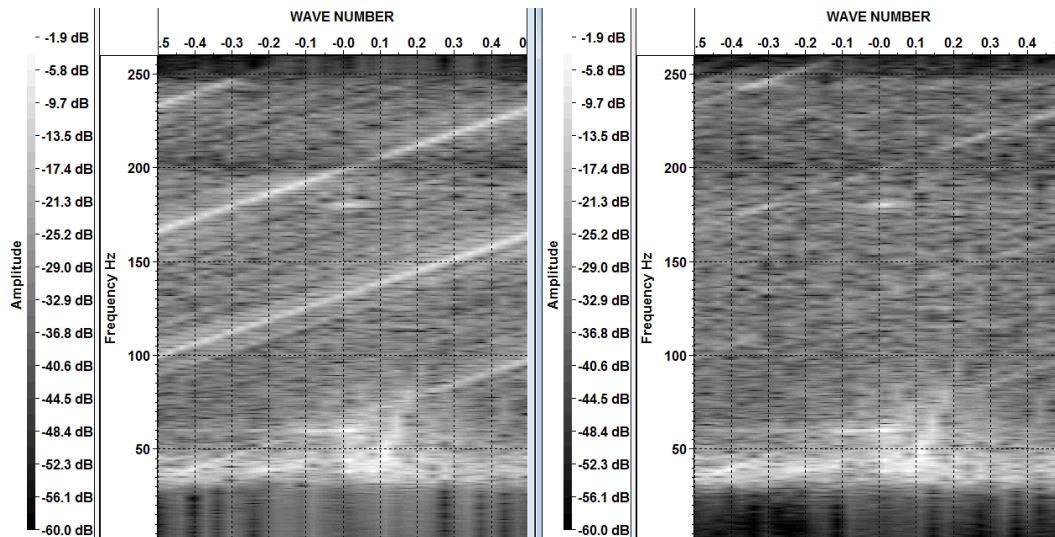


Figure 6.13. f-k spectra of shot gathers shown in Figure 6.11. Note that the air wave is spatially aliased in the original data and wraps around at about 100 Hz (left). The Gabor combination method attenuated the aliased air wave to a great extent. However, some residual air wave remains in the data.

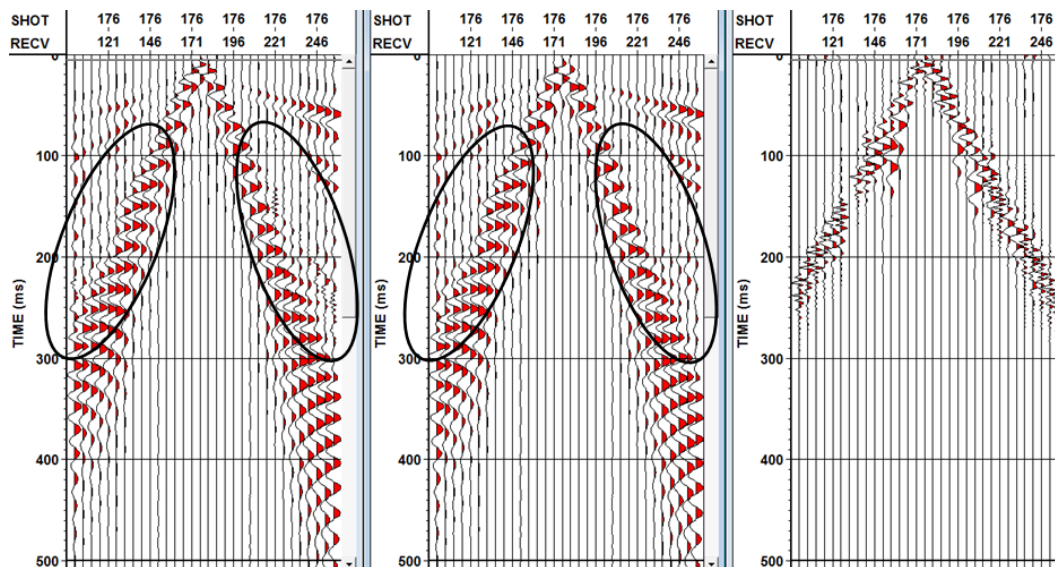


Figure 6.14. An example of air wave attenuation in a split-spread shot gather from Priddis. Data have been scaled relative to peak amplitude in the entire shot gather. Data before filter (left), data after filter (centre) and difference between original and filtered data (right).

CHAPTER SIX: CONCLUSIONS

Vibration monitoring can ascertain motion levels of natural as well as seismic activity. This can provide objective information about seismic effects, in particular when seismic operations are undertaken over sensitive and restricted areas. The monitoring results suggest that three components of ground motion need to be measured, since the PPV in the longitudinal and transverse components could be larger than the PPV measured in the vertical direction. Vibration measurements are fairly simple and straightforward in terms of peak values of particle velocity and air-overpressure. However, waveform analysis of ground motion and air vibration may reveal some further interesting features in the data.

Particle velocity and pressure data from seven different sensors were acquired in a test site located at the west end of the University of Calgary campus. Geophones and microphone outputs were sorted into receiver gathers and used to compute average amplitude spectra. Amplitude differences between conventional and calibrated geophone data can be found by taking the PPV of each trace recorded with conventional geophones, converting it to physical units, and dividing each Blastmate PPV measurements by the trace PPV. For hammer shots, the maximum and minimum amplitude difference between the calibrated and ION spike vertical geophone were 3.90 and 2.11, respectively. Mean factors for the ION spike and OYO geophones were between 1.98 and 3.62 for all particle velocity components and all hammer shots. Vibroseis uncorrelated data gave mean values between 2.98 and 4.18 for all particle velocity components. Pressure data recorded with three uncalibrated microphones and a single calibrated microphone suggested that some low-frequency acoustic energy (< 25 Hz) was recorded during this experiment. All microphones

responded quite similar at frequencies where the air wave is stronger (higher frequencies). However, they responded quite differently at lower frequencies (where the ground-roll is usually dominant). The low-frequency events displayed in time do not show any obvious coherence across the microphone receiver gathers.

Microphone output signals can be measured and used for air-noise attenuation in seismic records. A robust method for air wave attenuation has been developed in the Gabor domain, which combines microphone and geophone data. The procedure is semi-automatic in the sense that users need to specify three parameters only: the Gaussian window width and its time-shift increment, and a threshold.

Ideally, the suppression or attenuation of any manifestation of air-noise is desirable (e.g., air blast, winds, helicopter noise, etc.). In our experiments, the most signal noise measured with the microphones is the air wave. Therefore, at this point of the research the Gabor transform method is largely restricted to air wave attenuation.

CHAPTER SEVEN: FUTURE WORK

- Future comparisons of exploration geophones to high-precision blasting geophones would be benefited from using dynamite as seismic source because PPV's are much larger than PPV's from Vibroseis and sledgehammer shots. Dynamite shots would also enable comparison of far-offset data.
- Further investigate the dynamic range properties of the microphones for air noise recording.
- Improve the “mask” function by generating a smooth attenuation function. This can be achieved by taking the inverse of the microphone Gabor spectrum. However, by inverting the Gabor spectrum we face numerical instability. More work has to be done in this matter.
- Reduce computation times with improved code efficiency. This will allow us to reprocess seismic data using this technology and compare brute stacks to those achieved by conventional processing.
- Investigate microphone response to ground or case vibration. A spike could be attached to the body of the microphone prototype to follow ground motion (as in the geophone case) and minimize spurious signals generated by ground vibration.

REFERENCES

- Albert, D.G. and Orcutt, J.A., 1990, Acoustic pulse propagation above grassland and snow: Comparison of theoretical and experimental waveforms: *Journal of the Acoustical Society of America*; **87**, 93-100.
- Albert, D.A., 1993, Attenuation of outdoor sound propagation levels by a snow cover: Report of the Cold Region Research and Engineering Laboratory, US Army Corps of Engineers, 93-20.
- Beauduin, R., Lognonné, P., Montagner, J.P., Cacho, S., Karczewski, J.F., and Morand, M., 1996, The effects of the atmospheric pressure changes on seismic signals or how to improve the quality of a station: *Bulletin of the Seismological Society of America*, **86**, 1760-1769.
- Brook, R.A., Crews, G.A. and Sallas, J.J., 1989, Experimental analysis of the vibrator air wave: 59th Ann. Internat. Mtg., Soc. Expl. Geophys., Expanded Abstracts, 683-685.
- Carley, M.J., 2004, Some notes on acoustics: MECH0050 course notes, Special topics in aerodynamics, University of Bath, England.
- Claerbout, J.F., 1985, *Imaging the Earth's interior*: Blackwell Scientific Publications, Inc.
- Douze, E.J. and Sorrells, G.G., 1975, Prediction of pressure-generated earth motion using optimum filters: *Bulletin of the Seismological Society of America*, **65**, 637-650.
- Edwards, W.N., Eaton, D.W., McCausland, P.J., ReVelle, D.O., and Brown, P.G., 2007, Calibrating infrasonic to seismic coupling using the Stardust sample return shockwave: Implications for seismic observations of meteors: *Journal of Geophysical Research*, **112**, B10306.
- Gupta, R.N., Roy, P.P., and Singh, B., 1988, Prediction of peak particle velocity and peak air pressure generated by buried explosion: *International Journals of Mining and Geological Engineering*, **6**, 15-26.
- Harrop, N. and Attenborough, K., 1998, On the reliability of acoustic-to-seismic coupling ratio measurements: In Proc. 3rd Symposium, Bouyoucos Conference on Agroacoustics, November 1998, Tishomingo, Mississippi, US.
- Haykin, S., 1996, *Adaptive Filter Theory*: Prentice Hall, Third Edition.
- Henley, D.C., 2003, Coherent noise attenuation in the radial trace domain: *Geophysics*, **68**, 1408-1416.

- Hill, D.P., Fischer, F.G., Lahr, K.M., and Coakley, J.M., 1976, Earthquake sounds generated by body-wave ground motion: *Bulletin of the Seismological Society of America*, **66**, 1159-1172.
- Hoffe, B.H., Bertram, M.B., Bland, H.C., Gallant, E.V., Lines, L.R., and Mewhort, L.E., 2000, Acquisition and processing of the Pikes Peak 3C-2D seismic survey: CREWES Research Report 12.
- Hoffe, B.H., Lines, L.R., and Cary, P.W., 2000, Applications of OBC recording: *The Leading Edge*, **19**, 382-391.
- Hons, M.S., 2008, Seismic sensing: Comparison of geophones and accelerometers using laboratory and field data: M. Sc. thesis, University of Calgary.
- Hoover, G.M., Gallagher, J. G., and Rigdon, H.K., 1984, Vibrator signals: *Proceedings of the IEEE*, **72**, 1290-1301.
- InstanTel, 2001, Blastmate III Operator Manual: InstanTel, Inc.
- Kalinski, M.E., 2007, Effect of Vibroseis Arrays on Ground Vibrations: A numerical study: *Journal of Environmental & Engineering Geophysics*, **12**, 281-287.
- Kappus, M.E. and Vernon, F.L., 1991, Acoustic signature of thunder from seismic records: *Journal of Geophysical Research*, **96**, 10989-11006.
- Karsli, H., and Bayrak, Y., 2008, Ground-roll attenuation based on Wiener filtering and benefits of time-frequency imaging: *The Leading Edge*, **27**, 206-209.
- Lamoureux, M.P. and Adler, D.H., 2004, Nonstationary image processing via Gabor transforms: CREWES Research Report, 16.
- Larner, K., Chambers, R., Yang, M., Lynn, W., and Wai, W., 1983, Coherent noise in marine seismic data, *Geophysics*, **48**, 854-886.
- Lawton, D.C., and Bertram, M.B., 1990, Field tests of 3-component geophones: CREWES Research Report, 2.
- Le Pichon, A., Guilbert, J., Vega, A., Garcés, M., and Brachet, N., 2001, Ground-coupled airwaves and diffracted infrasound from the Arequipa earthquake of June 23, 2001: *Geophysical Research Letters*, **29**, 18, 33-1 – 33-4.
- Lin T.L., and Langston, C.A., 2007, Infrasound from thunder: A natural seismic source: *Geophysical Research Letters*, L14304.
- Lines, L.R. and Newrick, R.T., 2004, *Fundamentals of Geophysical Interpretation: Geophysical Monograph Series No. 13*, Society of Exploration Geophysicists.

- Margrave, G.F., Gibson, P.C., Grossman, J.P., Henley, D.C., Illiescu, V., and Lamoureux, M.P., 2005, The Gabor transform, pseudodifferential operators, and seismic deconvolution: *Integrated Computer-Aided Engineering*, **12**, 43-55.
- Mooney, H.M. and Kaasa, R.A., 1962, Air waves in engineering seismology: *Geophysical Prospecting*, **10**, 84-9.
- Norton, M. and Karczub, 2003, *Fundamentals of noise and vibration analysis for engineers*: Cambridge University Press.
- Press, F. and Ewing, M., 1951, Ground roll coupling to atmospheric compressional waves: *Geophysics*, **16**, 416-430.
- Press, F. and Oliver, J., 1955, Model study of air-coupled surface waves: *Journal of the Acoustical Society of America*, **27**, 43-46.
- Pritchett, W.C., 1990, *Acquiring better seismic data*: Springer.
- Qian, S. and Chen, D., 1999, Joint time-frequency analysis: *IEEE Signal Processing Magazine*, **16**, 2, 52-67.
- Rappin, D., Faure, P., and Artzt, C., 2007, Determination of safety distances and source monitoring during land seismic acquisition: 77th Ann. Internat. Mtg., Soc. Expl. Geophys., Expanded Abstracts, 41-42.
- Russell, B., Hampson, D., and Chun, J., 1990, Noise elimination and the Radon transform: *The Leading Edge*, **9**, 18-23.
- Sabatier, J.M., Bass, H.E., Bolen, L.N. and Attenborough K., 1986, Acoustically induced seismic waves: *The Journal of the Acoustical Society of America*, **80**, 646-649.
- Sallas, J.J. and Brook, R.A., 1989, Air-coupled noise produced by a seismic P-wave vibrator: 59th Ann. Internat. Mtg., Soc. Expl. Geophys., Expanded Abstracts, 686-689.
- Sharp, M.K., and Yule, D.E., 1998, Ground motion and air overpressure study: *Shock and Vibration*, **5**, 159-170.
- Sheriff, R.E. and Geldart, L.P., 1995, *Exploration Seismology*: Cambridge University Press.
- Steeple, D.W. and Miller, R.D., 1998, Avoiding pitfalls in shallow reflection surveys: *Geophysics*, **63**, 1213-1224.
- Stewart, R.R., Ferguson, R.J., Miller, S., Gallant, E.V., and Margrave, G.F., 1996, The Blackfoot seismic experiments: Broad-Band, 3C-3D, and VSP 3D surveys, *CSEG Recorder*, **21**, 7-10.

- Stewart, R.R., 1998, Air-noise reduction on geophone data using microphone records: CREWES Research Report, 10.
- Teasdale, D.L., Kiker, J.L., Oriard, L.L., Dowding, C.H., and Morrison, S.J., 2006, Response of test house to vibroseis vibrations and environmental forces: *Environmental & Engineering Geoscience*, **12**, 1, 25-37.
- Verschuur, D.J., Berkhout, A.J., and Wapenaar, C.P.A., 1992, Adaptive surface-related multiple elimination: *Geophysics*, **57**, 1166-1177.
- WorleyParsons Komex, 2007, Vibration monitoring of a seismic exploration program – Nanton, Alberta: Report to Compton Petroleum Corporation by WorleyParsons Komex (Project C66790000), Sep. 6, 2007.
- Xiang, N. and Sabatier, J.M., 2000, Land mine detection measurements using acoustic-to-seismic coupling: *Proceedings of the Society of Photographic Instrumentation Engineers*, 4038, 645-655.

APPENDIX A: MATCH FILTER DESIGNED VIA WIENER FILTER THEORY

A Wiener filter is a class of optimum linear filter that performs the linear estimation of a desired signal sequence from another related sequence. Applications of the Wiener filter are found in prediction, smoothing and deconvolution. The Wiener filter can be viewed as a correlation canceller in the sense that the optimum Wiener filter cancels that part of the desired output that is correlated with its input, while generating the estimation error (Haykin, 1996). This estimation error is usually minimized in the least-squares sense.

A MATLAB function called “match”, implemented by Dr. Gary Margrave, was used to compute a Wiener filter operator from a microphone signal. Convolution of the microphone signal with the operator produces a noise estimate of the noise component in the geophone signal. A simple subtraction is then applied in time domain to filter out the noise in the geophone. Figure A. 1 shows an example of air wave estimation using a Wiener filter and its subsequent subtraction from a contaminated geophone signal.

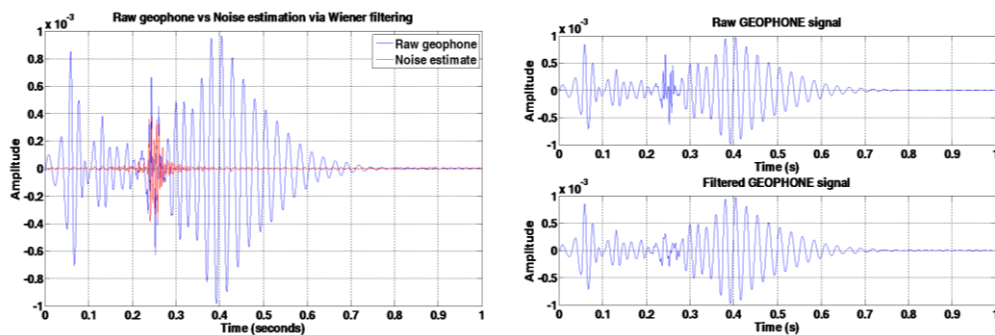


Figure A.1. A Wiener filter produces good noise estimates in the geophone signal by matching the input microphone signal (top).

APPENDIX B: MATCH FILTER DESIGNED VIA LEAST-SQUARES ADAPTIVE FILTER

The Least-Mean-Squares (LMS) adaptive filter is a sequential algorithm that modifies or adapts the tap weights of a FIR filter by continuous observation of its reference input, $x(n)$, and desired output, $d(n)$. The noise estimate, $y(n)$, is a weighted sum of a set of input samples. The number of input samples is determined by the number of taps (i.e., the filter's order). u is the algorithm step size, also called learning or adaptation rate. Minimizing the mean-squared value of the system output, $e(n)$, is equivalent to minimizing the mean-squared value of output noise, $V_o(n)-y(n)$. When $V_o(n)=y(n)$ the adaptive filtering is perfect (Haykin, 1996).

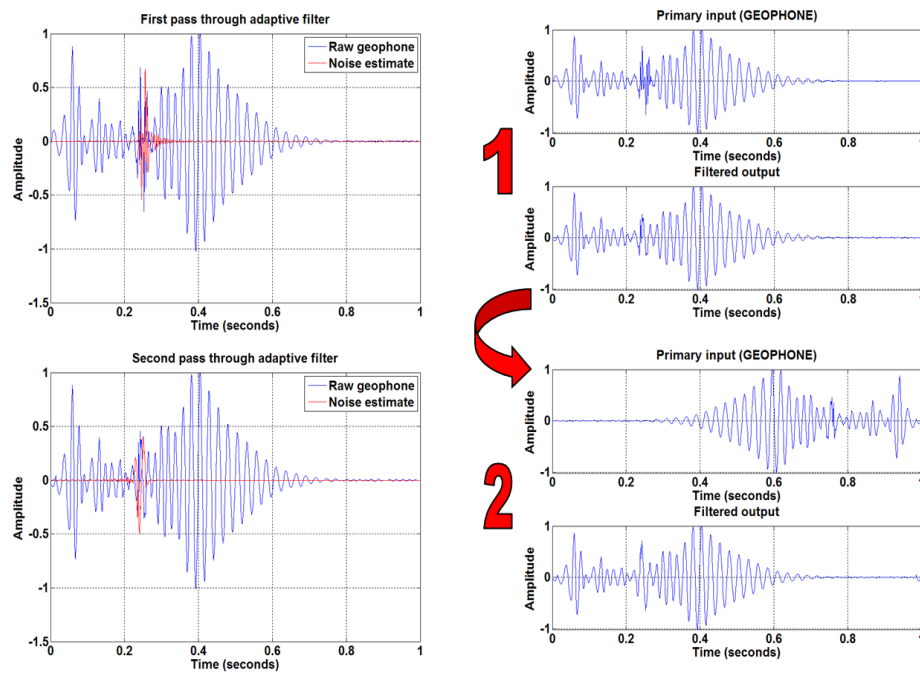


Figure B.1. A two-pass adaptive filter for air wave attenuation. The reference input to the filter, $x(n)$, is a microphone signal. Note that noise estimations, $y(n)$, are good but noise attenuation is achieved only after the second pass. However, this procedure is not as robust as the Gabor method.

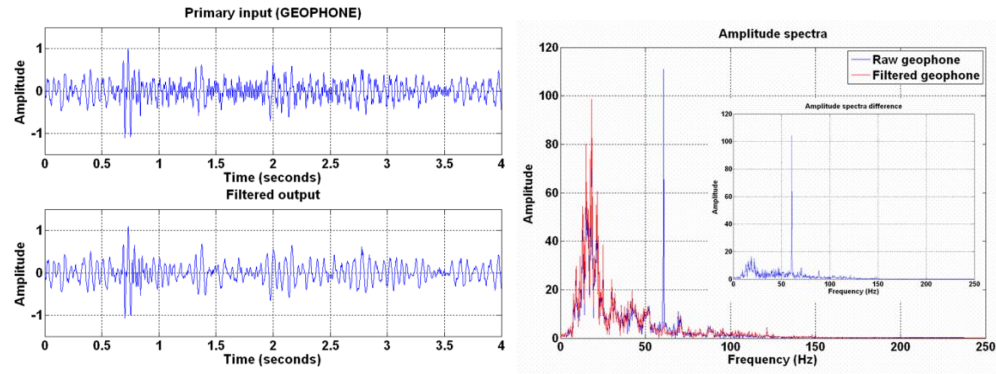


Figure B.2 Example of power-line noise cancellation by using the microphone signal as noise reference in an adaptive filter.

APPENDIX C: THE AIR-GROUND INTERFACE

Surface waves, commonly known as ground-roll, have been subject of an extensive research since the beginning of seismic exploration, resulting in several field and processing techniques to attenuate them. Unlike ground-roll, the horizontally propagating air blast (or air wave) and its interaction with the ground's surface have not received much attention, in part because the problem is more severe for shallow surveys than it is for petroleum exploration surveys. However, there are interesting ground motion phenomena associated to sound waves in the air that represent potential noise problems for any type of seismic survey.

Mooney and Kaasa (1962) introduced one of the first categorizations of ground motion phenomena related to propagating sound waves in the air. Figure C.1 shows a schematic of ordinary sound wave traveling directly through the air to the geophone, and the secondary ground vibration induced by the passage of the sound wave. In other words, the air blast can induce motion in the geophone in two different ways: 1) by direct pressure on the geophone case as the air wave passes over the geophone, or 2) by inducing ground motion in the proximity to the geophone case. In seismic records, these wave trains are commonly referred to as air waves.

The air-coupled ground roll, described by Press and Ewing (1951) and experimentally demonstrated by Press and Oliver (1955), occurs when a particular frequency component of a dispersive surface wave travels with a phase velocity equal to the sound speed in the air (331 m/s at 0° at sea level). In other words, the propagating sound wave in the air acts as a moving source of surface waves.

The opposite exchange of energy is also possible; Hill et al. (1976) describe the acoustic pressure waves in the air generated by body waves and/or surface waves in the ground, which have been reported as rumbling sounds before local earthquakes are felt.

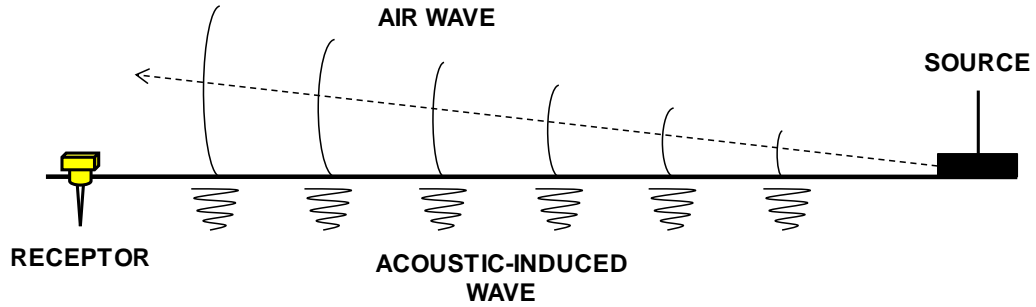


Figure C.1. Propagation mechanism of the acoustic-induced waves in the ground (after Mooney and Kaasa, 1962).

In general, the geophone data can be regarded as the response of the air-ground interface to a traveling air wave along the surface plus direct seismic waves, seismic reflections, refractions, ground roll and ambient noise. Similarly, the microphone data can be regarded as the response of the air-ground interface to traveling surface waves or body waves in the uppermost ground layer plus the direct air wave and ambient noise.

Using expressions in the frequency domain, an ideal microphone signal can be decomposed as

$$M(\omega) = [AW(\omega) + GAW(\omega)] \cdot S(\omega) + N(\omega). \quad (\text{C.1})$$

Similarly, the geophone signal can be decomposed as

$$G(\omega) = [R(\omega) + GR(\omega) + AW(\omega) + AWGR(\omega)] \cdot S(\omega) + N(\omega), \quad (\text{C.2})$$

where $M(\omega)$ is the microphone signal and $G(\omega)$ is the geophone signal. For the microphone data, $AW(\omega)$ is the air wave and $GAW(\omega)$ is the ground-coupled air wave. For the

geophone data, $R(\omega)$ is the reflectivity series, $GR(\omega)$ is the ground roll and $AWGR(\omega)$ is the air-coupled ground roll. For both cases, $S(\omega)$ is the source wavelet and $N(\omega)$ is ambient noise.

The transfer function $E(\omega)$ at the air-ground interface can be expressed as

$$E(\omega) = \frac{G(\omega)}{M(\omega)} = \frac{[R(\omega) + GR(\omega) + AW(\omega) + AWGR(\omega)] \cdot S(\omega) + N(\omega)}{[AW(\omega) + GAW(\omega)] \cdot S(\omega) + N(\omega)}. \quad (C.3)$$

C.1. Ground-coupled air wave

The ground-coupled air wave ($GAW(\omega)$) has been described as an inhomogeneous acoustic wave train above the free-surface, generated by vertical displacement of propagating seismic waves with phase velocity close to the sound speed in air. Due to the coupling at the air-interface, the horizontal phase velocities of the ground-coupled air wave and the seismic wave are identical (Le Pichon, et al., 2001).

Hill et al., (1976) made calculations of the transmission coefficients for seismic P and SV waves converted to acoustic waves at the Earth's surface. In the case of harmonic waves, the acoustic pressure, p , is related to the acoustic velocity potential ϕ by

$$p = -i\omega\rho_0\phi, \quad (C.4)$$

where ρ_0 is density of the air and ω is angular frequency. The transmission coefficients calculated by solving the Zoeppritz equations for the case of fluid (gaseous)-elastic solid media can be used to relate particle displacement in the incident elastic waves to the transmitted acoustic pressure by

$$p = i\omega\rho_0\alpha \frac{[\phi/\Phi]}{\cos\theta} U_{Pz} \quad (\text{C.5})$$

and

$$p = i\omega\rho_0\beta \frac{[\phi/\psi_{SV}]}{\cos\theta} U_{SVz}, \quad (\text{C.6})$$

where UP_z and USV_z are the vertical components of P and SV displacements, respectively. Φ is the displacement potential that describes a compressional wave moving with speed α , and Ψ_{SV} is the displacement potential that describes a shear wave moving with speed β .

Using the P or PS transmission coefficients appropriate for the near-surface material in the testing site, assuming reasonable angles of incidence and using Equations (C.5) and (C.6), we can calculate the acoustic pressure corresponding to a certain vertical particle displacement.

Figure C.2 shows the transmission coefficients for the cases where the incidence wave is in the lower layer. The elastic parameters for the upper layer (i.e., the air) are $Vp_0 = 340$ m/s, $Vs_0 = 0$, and $\rho_0 = 1.22$ kg/m³ (dry air at sea level and at 20°C). In the lower layer, $Vp_1 = 1800$ m/s, $Vs_1 = 720$ m/s, and $\rho_1 = 1600$ kg/m³. The plot on the left shows a weak dependence of the transmission coefficients for incident P waves on the angle of incidence for $\theta \leq 30^\circ$ and the phase is zero for all angles. The transmission coefficients for incident S-wave are plotted to the right in Figure C.2. In this case, there are marked phase changes at the critical angle and beyond. If the S-wave velocity is reduced to the sound speed in air, then the critical angles are also reduced and the amplitude at post critical angles increased due to resonant coupling.

C.2. Air-coupled ground roll

Shear-wave velocity is often associated with surface-wave velocity, especially Rayleigh-wave velocity, because the particle motion of Rayleigh waves is essentially retrograde elliptical. Therefore, ground roll propagation velocity is mainly determined by the medium's shear-wave velocity. Figure C.3 shows a theoretical seismic-to-acoustic ratio versus S-wave velocity for an incident air wave (i.e., an incident P-wave with pressure amplitude of 1 Pa) at a grazing angle over the surface of the earth. The seismic-to-acoustic ratio is calculated for both vertically and horizontally induced particle velocities with S-wave velocities varying from 200 to 1000 m/s. For simplicity, the assumed model is a liquid (gaseous)-solid interface separating a fluid half-space and an elastic half-space with the P-wave impinging from the liquid medium. In this case, the P-wave velocity of the gaseous medium is assumed to be 340 m/s.

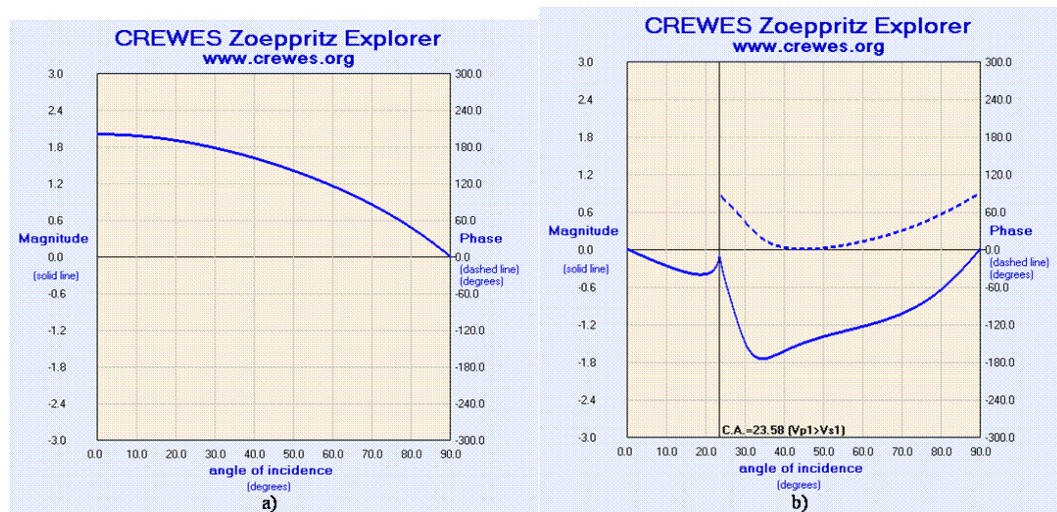


Figure C.2. P-wave transmission coefficients at the air-ground interface for a) an incident P-wave and b) an incident S-wave from the ground. Solid lines represent the magnitude and dashed lines represent the phase of the transmission coefficients. For the P-wave case, the phase is zero for all incidence angles. For the S-wave, there is a change in phase from zero for angles beyond the critical.

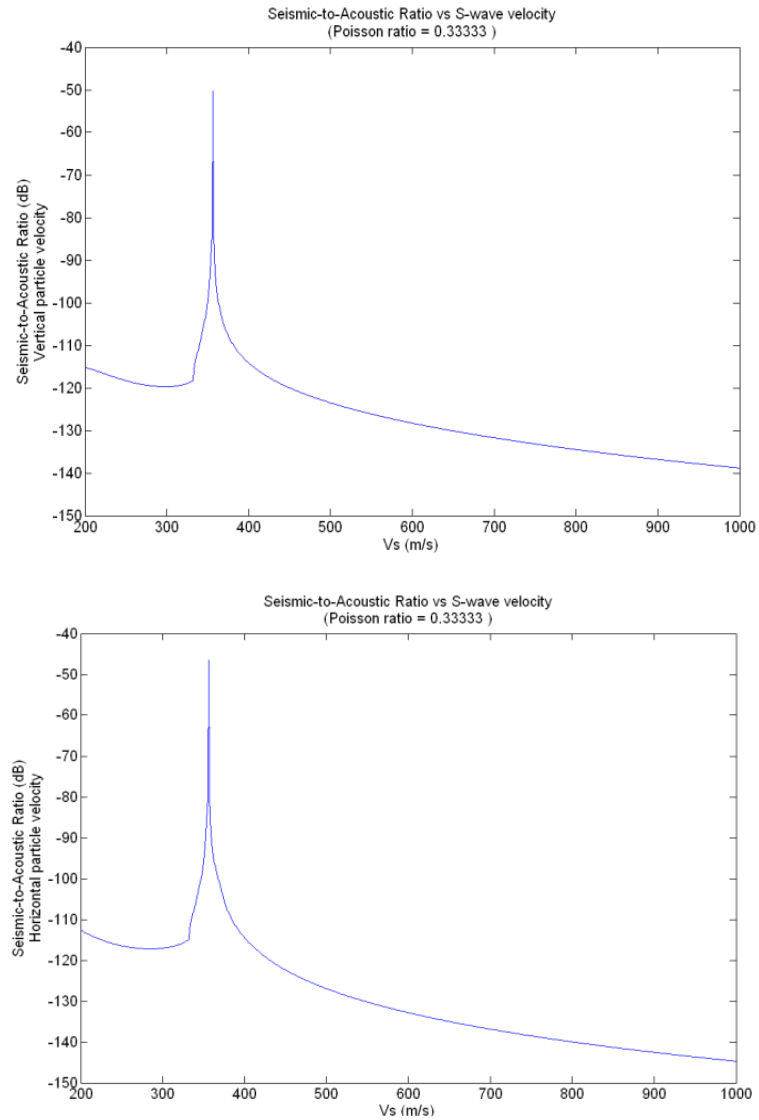


Figure C.3. Simple model of the resonant coupling that occurs when the S-wave associated with the ground roll is equal to the speed of sound in the air. The upper curve corresponds to the particle displacement in the vertical component. The lower curve corresponds to particle displacement in the horizontal component.